



Università degli Studi di Cagliari

DOTTORATO DI RICERCA

Scienze e Tecnologie Chimiche

Ciclo XXV

**DESIGN OF FUNCTIONAL COLLOIDAL MAGNETIC
NANOPARTICLES FOR BIOMEDICAL APPLICATIONS**

Settore/i scientifico disciplinari di afferenza

CHIM/03

Presentata da:	Dott.ssa Federica Orrù
Coordinatore Dottorato:	Prof. Mariano Casu
Relatore:	Dott.ssa Carla Cannas

Esame finale anno accademico 2011 – 2012

A Science has great beauty.

A scientist in his laboratory is not only a technician:

he is also a child placed before natural phenomena

which impress him like a fairy tale.

(Marie Curie)

To my Family

Nanostructured materials have been the focus of scientific interest in recent years, because of the peculiar properties displayed by matter in nano-size form. The interest has been growing steeply since possible applications in biomedical fields have shown to be realistic. The interaction of magnetic nanoparticles with applied magnetic field gradients makes these particles attractive for their potential applications in biomedical imaging, diagnostic, and therapy. In this context, a great advantage are the superparamagnetic properties that can be exhibited by the nanoparticles. They behave as paramagnetic centres with high magnetic moment at room temperature, as it arises from the coupling of many atomic spins. After eliminating the external magnetic field, the particles no longer show magnetic interaction, thus reducing the possibility of particle aggregation; this feature is especially important for their applications. Biomedical use of magnetic nanoparticles imposes their uniform dispersion and stability in the biological fluids; moreover their size range should easily permit cell internalization through pinocytosis or endocytosis. Therefore, surface modification, via coating or encapsulation, is widely employed to improve nanoparticles properties and for immobilization of functional molecules. Magnetic nanoparticles have garnered widespread attention in recent years to develop and understand synthetic means to control their size, magnetic behaviour, and chemical reactivity. Simultaneously tuning surface chemistry and physical properties enable preparation of functional magnetic nanoparticles. Recent advances in synthesis have allowed to easily prepare a wide range of magnetic nanoparticles through aqueous or non aqueous approaches. It has been widely shown that the non-aqueous routes are more efficient in producing stable colloidal nanoparticles with narrow size distribution, high crystallinity, tunable size and shape. However, this approach typically produces hydrophobic nanoparticles limiting their applications in biological and medical fields. Thus, the transformation of these

hydrophobic nanoparticles into hydrophilic is a crucial step toward their widespread use.

The aim of the present PhD research project is to give a contribution to implement synthetic approaches to develop novel colloidal magnetic nano-architectures with applications in biomedical field. In particular, the research moves along two principal themes. From one side it has been investigated the possibility to tune magnetic nanoparticles size and properties through appropriate synthetic methodologies. From the other side, since the selected synthetic approach provides hydrophobic nanoparticles, particular attention has been devoted to the surface modification with organic and inorganic coatings in order to convert them into water dispersible systems. To this end, a multi-technique approach is used. A first structural analysis is performed by wide-angle X-ray Diffraction to obtain information about the crystalline phases and the crystallite size (coherent domain). Direct images of the samples, obtained by Transmission Electron Microscopy observations allowed an evaluation of the particle sizes, their distribution and the homogeneity of the particle dispersions.

In order to study the magnetic-nanoparticles/coating interface, studies with FT-IR spectroscopy have been performed on hydrophobic nanoparticles and on all the systems in which the surface modification has been applied. To investigate the textural properties of the silica based composites nitrogen physisorption measurements have been performed in combination with low-angle X-ray diffraction to evidence the ordered porosity. Magnetic measurements have been acquired in order to understand how the different chemical composition, size and coatings can affect the magnetic properties of nanoparticles.

All the measurements have been carried out at the Department of Chemical and Geological Sciences at the University of Cagliari.

The present thesis is structured as follow: after an introduction on magnetic nanoparticle applications and properties (*chapter 1*), the *chapter 2* is devoted to the magnetic nanoparticles with a special emphasis on the different surface chemical

modification processes for their transferring into water environment. In the *chapter 3* a synthetic approach based on a surfactant-assisted high-temperature thermal decomposition of metallorganic compounds is described in order to prepare hydrophobic magnetite and cobalt ferrite nanoparticles with different sizes, narrow particle size distributions and tuned magnetic properties. Magnetite is an ideal candidate material because of its documented biocompatibility and high saturation magnetization, cobalt ferrite has been also chosen because of its known large magnetic anisotropy compared to other ferrites, in spite of highly toxic cobalt. In the *chapter 4* magnetic nanoparticles possessing a hydrophobic surface are transferred into water through molecular coatings. Oleic acid/oleylamine molecules, bound to the surface of magnetic nanoparticles, are substituted (ligand-exchange) by molecules possessing a dual functionality that allows their dispersion in water. The selected molecules are short-chain dicarboxylic acids or alkylsilanes. These molecules form a coating on the surface of the magnetic nanoparticles via carboxylic or Me-O-Si bonds, ensuring their stability in aqueous environment, as well as creating the conditions for a their possible conjugation with biologically active molecules. The hydrophobic nanoparticles is converted into hydrophilic also through the intercalation process with suitable surfactants such as cetyltrimethylammonium bromide (CTAB). These “*magnetic pseudo micelles*” build up of an inorganic core (magnetite or cobalt ferrite) and an organic shell (oleic acid-oleylamine-CTAB) are stable in water and can be employed in biological field. In the *chapter 5* pure CTAB micelles are also used as organic templates for the formation of colloidal mesostructured silica nanoparticles through a base-catalyzed sol-gel process. The hybrid-organic-inorganic “*magnetic pseudo micelles*”, have been proposed as building blocks for the creation, through the self assembling processes, of colloidal magnetic mesostructured silica nanoparticles with hexagonal or cubic pore structure. Silica is stable, biocompatible and hydrophilic, and if prepared in the form of mesostructured nanoparticles, showing high surface area and high pore volume, allows to incorporate an high number of magnetic nanoparticles, and to associate to the

magnetic properties other properties by entrapping fluorescent molecules, quantum dots, or luminescent nanoparticles.

Due to their peculiar features, these colloidal magnetic nanocarriers can be considered promising versatile multifunctional systems for applications in theranostic as well as in bimodal (magnetic and optic) imaging applications. For these reasons, at last, some *general comments and future insights* are given.

The *appendix* reports the details of the equipments and the methods.

Foreword.....	i-iv
Chapter 1. Magnetic Metal Oxide Nanoparticles in Biomedical Applications.....	1-25
1.0 Magnetic Metal Oxide Nanoparticles and Biomedical Applications.....	2
1.1 Introduction	2
1.2 Superparamagnetic Nanoparticles	4
1.3 Synthesis Techniques: Iron Oxide Nanoparticles.....	7
1.4 Biomedical applications of Magnetic Nanoparticles	9
1.4.1 Therapeutic applications	10
1.4.2 Diagnostic applications	15
References.....	22
Chapter2. Magnetic Nanoparticles: Surface Modification and Silica Nanocomposite	27-43
2.0 Surface modification of magnetic nanoparticles	28
2.1 Introduction	28
2.2 Surface modification.....	29
2.2.1 Organic coating.....	30
2.2.2 Mechanisms of surface modification by organic molecules	31
2.2.3 Inorganic coating.....	33
2.2.4 Silica coating.....	34
References.....	38

Chapter 3. Colloidal Magnetic Nanoparticles prepared by high temperature thermal decomposition of organometallic precursors assisted by surfactants(HTDSA).....	44-71
3.0 Experimental.....	45
3.1 Introduction.....	45
3.2 Nucleation and growth mechanism in HTDSA strategy.....	46
3.3 Synthesis of Spinel Ferrite Nanoparticles.....	50
3.3.1 CoFe ₂ O ₄ nanoparticles: Characterization.....	52
3.3.2 Fe ₃ O ₄ nanoparticles: Characterization.....	61
3.4 Conclusions.....	67
References.....	69
Chapter 4. Trasferring of hydrophobic nanoparticles into water: Legend exchange and Intercalation processes .	72-98
4.0 Experimental.....	73
4.1 Introduction.....	73
4.2 Legend Exchange with carboxylic acid and alkylsilane.....	73
4.2.1 Ligand Exchange with short chain carboxylic acids.....	75
4.2.2 Characterization.....	76
4.3 Ligand Exchange with alkylsilane.....	83
4.3.1 Ligand Exchange with alkylsilanes.....	86
4.3.2 Characterization.....	87
4.4 Intercalation process with CTAB (MAG_CTAB).....	91
4.4.1 Characterization.....	93
4.5 Conclusions.....	95
References.....	96

Chapter 5. Colloidal Magnetic Mesostructured Silica Nanoparticles	99-141
5.0 Experimental.....	100
5.1 Introduction.....	100
5.2 Mesoporous Silica Nanoparticles.....	105
5.3 Hexagonal and Cubic Mesostructured Silica nanoparticles (MSN_H, MSN_C): synthesis and characterization	108
5.3.1 Synthesis	108
5.3.2 Microstructural and textural Characterization.....	112
5.4 Magnetic mesostructured silica based nanoparticles (MMSN_H and MMSN_C): Synthesis, characterization and magnetic properties	121
5.4.1 Introduction.....	121
5.4.2 MMSN_H Synthesis.....	123
5.4.3 Characterization	125
5.5 Conclusions	138
References.....	139
Conclusions and future insights.....	142-145
Appendix Equipments and Techniques	146-151
Acknowledgements.....	152

This chapter gives general information about properties of magnetic nanomaterials, synthesis approaches and biomedical applications. It provides the background for understanding and exploring the biomedical applications of magnetic nanoparticles.

Chapter 1

Magnetic Metal Oxide Nanoparticles in Biomedical Applications

1.0 Magnetic Metal Oxide Nanoparticles and Biomedical Applications

1.1 Introduction

The development of novel materials is a fundamental focal point of chemical research; and this interest is mandated by advancements in all areas of industry and technology. Therefore in the last decade, the scientific research has focused on the development of new materials at the atomic, molecular, or macromolecular levels, on the length scale of approximately 1-100 nm. These research efforts are expected to provide a fundamental understanding of phenomena and materials at the nanoscale and to create and use structures, devices, and systems that have novel properties and functions due to their small and/or intermediate size, typically under 100 nm.^[1] Successful application of nanoparticles not only depends on the special properties exhibited at this scale such as an enhanced electronic, mechanical, and chemical response but also on their manipulation to achieve specific objectives. In this sense, magnetic nanoparticles offer a range of opportunities as their response can be tailored by choosing from a variety of magnetic materials with different magnetic properties that can be manipulated by the use of external magnetic fields and by modification of their surfaces with molecules specific for intended applications.

Magnetic nanoparticles are a major class of nanoscale materials with the potential to revolutionize current clinical diagnostic and therapeutic techniques. Due to their unique physical properties and ability to function at the cellular and molecular

level of biological interactions, they are being actively investigated as the next generation of magnetic resonance imaging (MRI) contrast agents^[2], as carriers for targeted drug delivery^[3], in the hyperthermia^[4] and as magnetic separation agent.^[5] This because, first, they have sizes that place them at dimensions comparable to those of a virus (20–500 nm), a protein (5–50 nm) or a gene (2 nm wide and 10–100 nm long). Second, the nanoparticles are magnetic, which means that they obey Coulomb's law, and can be manipulated by an external magnetic field gradient. Third and finally, nanoparticles have a large surface that can be properly modified to attach biological agents. Applications in biotechnology impose strict requirements on the particles' physical, chemical and pharmacological properties, including chemical composition, granulometric uniformity, crystal structure, magnetic behavior, surface structure, adsorption properties, solubility and low own toxicity. For example, in order for magnetic drug-targeting to be safe and effective (with the minimum amount of magnetic particles, a maximum of drug should be easily administered and transported to a specific site), the following parameters of the nanomagnets are critical: (a) particle size (small as possible to improve tissular diffusion, and to have long sedimentation times and high effective surface areas), (b) surface characteristics (easy encapsulation of the magnetic nanoparticles protects them from degradation and endows biocompatibility), and (c) good magnetic response (possibility of decreasing nanomagnets concentration in blood and therefore diminishing the associated side effects).^[6] Although early research in the field can be dated back several decades, the recent surge of interest in nanotechnology has significantly expanded the breadth and depth of magnetic nanoparticles research. With a wide range of applications in the detection, diagnosis, and treatment of illnesses, such as cancer^[7], cardiovascular disease^[8], and neurological disease^[9], Magnetic nanoparticles may soon play a significant role in meeting the healthcare needs of tomorrow.^[10]

1.2 Superparamagnetic Nanoparticles

The penetration of magnetic fields through human tissue and the ability to remotely detect or manipulate magnetic materials have been investigated for use in medicine for centuries.^[11] To better understand the advantages of using the magnetic nanoparticles in biomedical field we review some of the fundamental concepts of magnetism and the properties of nanoparticles. More thorough and detailed discussion of this topic can be found in the literature.^[12] The classification of a material's magnetic properties is based on its magnetic susceptibility (χ), which is defined by the ratio of the induced magnetization (M) to the applied magnetic field (H). In diamagnetic materials, the magnetic moment is antiparallel to H resulting in very small and negative susceptibilities (-10^{-6} to -10^{-3}). They do not retain magnetic properties when the external field is removed. Materials with magnetic moments aligned parallel to H and susceptibilities on the order of 10^{-6} to 10^{-1} are described as paramagnetic. While in ferri- and ferromagnetic materials, magnetic moments also align parallel to H , coupling interactions between the electrons of the material result in ordered magnetic states, i.e., magnetic domains, and large spontaneous magnetization. The susceptibilities of these materials depend on their atomic structures, temperature, and the external field H . If we now reduce the size of the ferromagnetic material we may ultimately reach a size where thermal energy ($K_B T = 4 \cdot 10^{-21}$ at 300 K) can randomize the magnetization, such that when there is no externally applied field the magnetization measured in a finite time interval (typically, 100 s) is zero. Such materials, at small sizes (on the order of nanometers), show no coercivity and behave as a single paramagnetic domain with a large magnetic moment, known with the name of superparamagnets (*figure 1(a) and (c)*). The randomization of the magnetization takes place by excitation over an energy barrier given by the product of the anisotropy constant, K , and the volume, V . Note that the relaxation time, τ , depends exponentially on the energy barrier, KV , and hence to reproducibly control the magnetic behavior of superparamagnetic nanoparticles, narrow size distributions are required (*figure 1 (b)*). A superparamagnet is defined as an assembly of giant magnetic moments which are not interacting, and which can fluctuate

when the thermal energy, $k_B T$, is larger than the anisotropy energy. However, at sufficiently high temperatures (i.e., blocking temperature T_B) thermal energy is sufficient to induce free rotation of the particle resulting in a loss of net magnetization in the absence of an external field. This superparamagnetic property, marked by the lack of remanent magnetization after removal of external fields, enables the particles to maintain their colloidal stability and avoid aggregation making it feasible for their use in biomedical applications. Furthermore, the coupling interactions within these single magnetic domains result in much higher magnetic susceptibilities than paramagnetic materials.

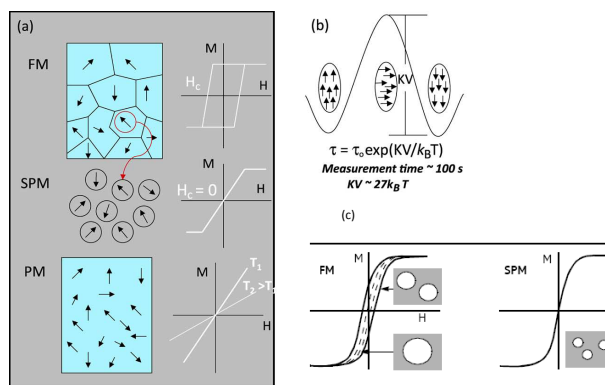


Figure 1. Magnetic behavior of materials: ferromagnetic materials (FM) are characterized by exchange interaction, hysteretic behavior and a finite coercivity, H_c , paramagnetic materials (PM) the non-interacting spins are characterized by a linear susceptibility that is inversely dependent on the temperature (Curie law), superparamagnetic materials (SPM), below a certain critical size the multidomain (FM) becomes a single domain superparamagnetic (a); and the superparamagnetic nanoparticles exhibit no remanence or coercivity, that is, there is no hysteresis in the magnetization curve (c).

Although superparamagnetism is a favorable property of small particles, the reduction of particle size is not without some consequences. As particle sizes decrease, surface-to-volume ratios increase resulting in pronounced surface effects, such as noncollinear spins, spin canting, and spin-glass-like behavior, which can significantly impact the magnetic properties of the material.^[13] Typically, the saturation magnetization (M_s) values of nanoparticles, corresponding to the complete alignment of all individual

moments in a sample, are smaller than their corresponding bulk phases due to disordered crystal structure resulting from high surface curvature, which increases with particle size reduction. Furthermore, significant differences in magnetic properties are observed with superparamagnetic nanoparticles obtained through different chemical processes. More detailed explanations of the physical properties of superparamagnetic nanoparticles and nanoscale magnetic phenomena can be found in recent reviews.^[14,15,16]

The magnetic behaviour of an assembly of nanoparticles is related to the crystalline structure. Among the different nanostructured magnetic materials, the metal oxide, such as magnetite (Fe_3O_4) and cobalt ferrite (CoFe_2O_4), with spinel structure ($\text{Me}^{\text{II}}\text{Me}_2^{\text{III}}\text{O}_4$) represent probably the most promising class in biomedical application, because the rich crystal chemistry of spinels offers excellent opportunities for fine-tuning the magnetic properties. These have a face-centered cubic (fcc) structure in which the oxygen atoms are cubic close-packed. The structure contains two interstitial sites, occupied by metal cations, with tetrahedral, (A)-site, and octahedral, [B]-site, oxygen coordination, resulting in a different local symmetry (*figure 2*).

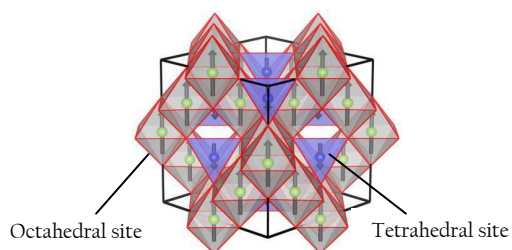


Figure 2. Schematic representation of spinel structure.

When the (A)-sites are occupied by Me^{II} cations and the [B]-sites by Me^{III} cations, the structure is referred to as normal spinel, $(\text{Me}^{\text{II}}) [\text{Me}^{\text{III}}]$. However, if the A sites are completely occupied by Me^{III} and the B-sites are randomly occupied by Me^{II} and Me^{III} , then the structure is referred to as inverse spinel, $(\text{Me}^{\text{III}}) [\text{Me}^{\text{III}} \text{Me}^{\text{II}}]$. In general, the cationic distribution in octahedral and tetrahedral sites is quantified by the “inversion degree” (γ), which is defined as the fraction of divalent ions in octahedral sites.^[17,18]

1.3 Synthesis Techniques: Iron Oxide Nanoparticles

It has long been of scientific and technological challenge to synthesize the magnetic nanoparticles of customized size and shape. Physical methods such as gas phase deposition and electron beam lithography are advantageous in that they produce nanomaterials of high purity and are applicable to large-scale production, but unfortunately are elaborate procedures that suffer from the inability to control the size of particles in the nanometer size range.^[19] The wet chemical routes to magnetic nanoparticles are simpler, more tractable and more efficient with appreciable control over size, composition and sometimes even the shape of the nanoparticles.^[20]

The most common methods including sol-gel,^[21,22] co-precipitation,^[23,24] thermal decomposition,^[15,25] hydrothermal synthesis,^[26] microemulsion,^[27,28] sonochemical synthesis,^[29] and sonochemical synthetic route can all be directed to the synthesis of high quality of iron oxide nanoparticles. In addition, these magnetic nanoparticles can also be prepared by the other methods such as electrochemical synthesis,^[30,31] laser pyrolysis techniques.^[32] In *table 1* are reported the main synthesis methods used to date for the preparation of magnetic nanoparticles and the nanoparticle characteristics.

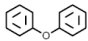
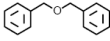
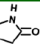
Table 1. Comparison of different synthesis methods to produce magnetic nanoparticles

Synthetic method	Nanoparticle characteristics							
	Size		Shape control	Synthesis	Reaction			Surface-capping agents
	Range	Distribution			Temperature	Time	Yield	
Aerosol/vapor (pyrolysis)	5-60 nm	Broad	Good	Complicated, vacuum/controlled atmosphere	High/very high	Minutes/hours	Medium	Needed, after reaction
Gas deposition	5-50 nm	Narrow	Good	Complicated, vacuum/controlled atmosphere	Very high	Minutes	High/scalable	Needed, after reaction
Sol-gel	3-150 nm	Narrow/broad	Good	Simple	20-90 °C	Hours/days	Medium	Needed, during reaction
Co-precipitation	10-50 nm	Broad/narrow	Poor	Very simple	20-90 °C	Minutes	High/scalable	Needed, during reaction
Thermal decomposition	2-20 nm	Very narrow	Very good	Complicated, inert atmosphere	100-330 °C	Hours	High/scalable	Needed, during reaction
Microemulsion	4-15 nm	Narrow	Good	Complicated	20-70 °C	Hours/days	Low	Needed, during reaction
Hydrothermal	10-150 nm	Narrow	Very good	Simple, high pressure	100 °C -high	Hours/days	Medium	Needed, during reaction

Among these methodologies thermal decomposition and hydrothermal methods seems to lead to the best results in terms of fine particle size tuning and narrow particle size distribution. In order to obtain primary particles of appropriate size and with an adequate distribution of the same, these methods allow to control the kinetically phase nucleation and particle growth through the use of suitable stabilizing agents, often surfactants. Such stabilizers interact intimately with the surface of nanoparticles, so that the growth of the nanocrystals is kinetically inhibited by the capping of these chemical and physical agents.^[33] The control of dimensions, of their distribution, morphology, degree of crystallinity, the agglomeration of particles during and after the synthesis and the manipulation of these materials, constitute critical points for obtaining the final product, given that from these parameters depend on the main properties of nanostructured materials. Recently, the method which has allowed to obtain precise control of size and shape of magnetic nanoparticles with a narrow size distribution, high crystallinity, high stability in organic solvents, is the synthesis based on the *High Temperature Decomposition of organometallic precursors Assisted by Surfactants (HTDSA)*.^[25]

Iron oxide nanoparticles with a high level of monodispersity and controlled size can be obtained by *HTDSA* of iron organic precursors, such as Fe(Cup)₃, (cup=N-nitrosophenylhydroxylamine), Fe(acac)₃, (acac= acetylacetonate), or Fe(CO)₅, using surfactants and high boiling point organic solvents such as the ones shown in *table 2*.

Table 2. High boiling points solvents for thermal decomposition.

Solvent	Structure	BP (°C)
1-hexadecene	CH ₃ (CH ₂) ₁₃ CH=CH ₂	274
dioctyl ether	CH ₃ (CH ₂) ₇ O(CH ₂) ₇ CH ₃	287
1-octadecene	CH ₃ (CH ₂) ₁₅ CH=CH ₂	317
1-eicosene	CH ₃ (CH ₂) ₁₇ CH=CH ₂	330
trioctylamine	[CH ₃ (CH ₂) ₇] ₃ N	365
diphenyl ether		259
dibenzyl ether		298
docosane	CH ₃ (CH ₂) ₂₀ CH ₃	369
2-pyrrolidone		245

By rapidly increasing the reaction temperature to about 200 °C, triggering a burst of nucleation followed by aging at that temperature until the net nucleation rate is zero. Subsequently, the temperature is slowly increased to about the boiling temperature (about 300°C) of the solvent to promote particle growth by diffusion of free atoms to the growing particles.^[34] Surfactants such as oleic acid, oleylamine, sodium oleate, and tri-*n*-octylphosphine oxide (TOPO) are usually used as coordinating solvent in nucleation phase and growth of nanoparticles, and to avoid particle agglomeration during synthesis. The formation of an intermediate Fe-oleate complex is a critical step in determining the final particle size.^[33,36]

1.4 Biomedical applications of Magnetic Nanoparticles

For many biomedical applications, magnetic nanoparticles presenting superparamagnetic behavior (no remanence along with a rapidly changing magnetic state) at room temperature are desirable. Biomedical applications are commonly divided into two major categories: *in vivo* and *in vitro* applications. *In vivo* applications could be further separated in therapeutic (hyperthermia and drug-targeting) and diagnostic applications (nuclear magnetic resonance (NMR) imaging), while for *in vitro* applications the main use is in diagnostic (separation/selection, and magnetorelaxometry).^[37] Consequently, additional restrictions apply on various magnetic nanoparticles for *in vivo* or *in vitro* biomedical application. It is rather simple for *in vitro* applications of magnetic nanoparticles. The size restriction as well as biocompatibility/toxicity are not so critical for *in vitro* applications, when compared with *in vivo* ones. Therefore, superparamagnetic composites containing submicron diamagnetic matrixes and superparamagnetic nanocrystals can be used. Composites with long sedimentation times in the absence of a magnetic field are also acceptable. It was noticed that functionalities may be provided readily for the superparamagnetic composites because of the diamagnetic matrixes. On the other hand, severe restrictions must be applied for magnetic nanoparticles for *in vivo* biomedical applications. First of

all, it is a requisite that the magnetic components should be biocompatible without any toxicity for the biosystems of interest. It is no doubt that interdisciplinary research collaboration is badly needed for clinical and biological applications of magnetic nanoparticles. Research fields involved include chemistry, materials science, cell engineering, clinical tests and other related scientific efforts.^[38] In this section, an overview of the biomedical applications of magnetic nanoparticles will be presented.

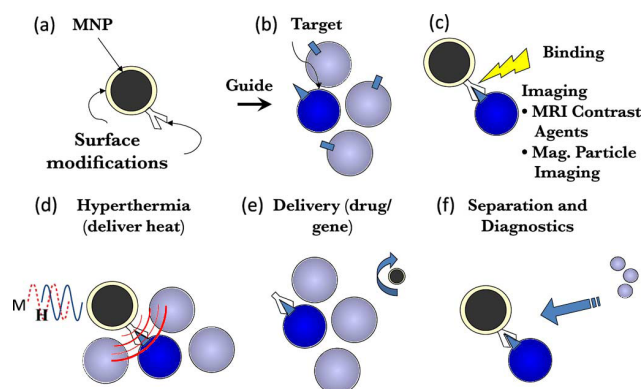


Figure 3. Magnetic Nanoparticles in Biomedicine.

1.4.1 Therapeutic applications

Hyperthermia. The possibility of treating cancer by artificially induced hyperthermia has led to the development of many different devices designed to heat malignant cells while sparing surrounding healthy tissue. Experimental investigations of the application of magnetic materials for hyperthermia date back to 1957.^[39] Since then there have been numerous publications describing a variety of schemes using different types of magnetic materials, different field strengths and frequencies and different methods of encapsulation and delivery of the particles. In broad terms, the procedure involves dispersing magnetic particles throughout the target tissue, and then applying an A.C. magnetic field of sufficient strength and frequency to cause the particles to heat. This

heat conducts into the immediately surrounding diseased tissue whereby, if the temperature can be maintained above the therapeutic threshold of 42°C for 30 min or more, the cancer is destroyed. The physical principle for which a magnetic material can be heated by the action of an external alternating magnetic field are the loss processes that occur during the reorientation of the magnetization of magnetic materials with low electrical conductivity.^[40] Whereas the majority of hyperthermia devices are restricted in their utility because of unacceptable coincidental heating of healthy tissue, magnetic particle hyperthermia is appealing because it offers a way of ensuring only the intended target tissue is heated. The advantage of magnetic hyperthermia is that allows the heating to be restricted to the tumour area. Moreover, the use of subdomain magnetic particles (nanometre-sized) is preferred instead multidomain (micron-sized) particles because nanoparticles absorb much more power at tolerable AC magnetic fields.^[41] Finally, it should be mentioned that the heating potential is strongly dependent on the particle size and shape, and thus having well-defined synthetic routes able to produce uniform particles is essential for a rigorous control in temperature. A number of studies have demonstrated the therapeutic efficacy of this form of treatment.^[42] To date, however, there have been no reports of the successful application of this technology to the treatment of a human patient. The challenge lies in being able to deliver an adequate quantity of the magnetic particles to generate enough heat in the target using A.C. magnetic field conditions that are clinically acceptable. Most of the laboratory-based studies reported so far are characterised by the use of magnetic field conditions that could not be safely used with a human patient. In most instances, reducing the field strength or frequency to safer levels would almost certainly lead to such a reduction in the heat output from the magnetic material as to render it useless in this application. The frequency and strength of the externally applied A.C. magnetic field used to generate the heating is limited by deleterious physiological responses to high frequency magnetic fields. These include stimulation of peripheral and skeletal muscles, possible cardiac stimulation and arrhythmia, and non-specific inductive heating of tissue. Generally, the usable range of frequencies and amplitudes is considered to be $f = 0.05\text{-}1.2$

MHz and $H = 0\text{-}15 \text{ kAm}^{-1}$, and a common rule of thumb is that the product $H \cdot f$ should not exceed $4.85 \times 10^8 \text{ Am}^{-1}\text{s}^{-1}$.^[43] The amount of magnetic material required to produce the required temperatures depends to a large extent on the method of administration. For example, direct injection allows for substantially greater quantities of material to be localised in a tumour than do methods employing intravascular administration or antibody targeting, although the latter two may have other advantages. A reasonable assumption is that around 5-10 mg of magnetic material concentrated in each cm^3 of tumour tissue is appropriate for magnetic hyperthermia in human patients.^[5]

Drug Delivery. The major disadvantage of most chemotherapies is that they are relatively non-specific. The therapeutic drugs are administered intravenously leading to general systemic distribution, resulting in deleterious side-effects as the drug attacks normal, healthy cells in addition to the target tumour cells. For example, the side effects of anti-inflammatory drugs on patients who have chronic arthritis can lead to the discontinuation of their use. However, if such treatments could be localised, e.g. to the site of a joint, then the continued use of these very potent and effective agents could be made possible. Recognition of this led researchers in the late 1970s to propose the use of magnetic carriers to target specific sites (generally cancerous tumours) within the body. The objectives are twofold:

- to reduce the amount of systemic distribution of the cytotoxic drug, thus reducing the associated side-effects,
- to reduce the dosage required by more efficient, localised targeting of the drug.

In magnetically targeted therapy, a cytotoxic drug is attached to a biocompatible magnetic nanoparticle carrier. These drug/carrier complexes usually in the form of a biocompatible ferrofluid are injected into the patient via the circulatory system. When the particles have entered the bloodstream, external, high-gradient magnetic fields are used to concentrate the complex at a specific target site within the body (*figure 4*).

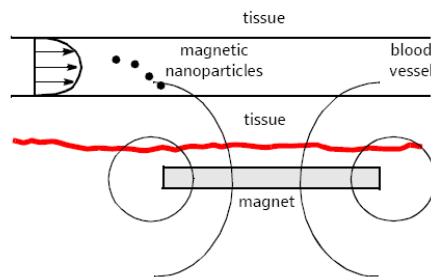


Figure 4. A hypothetical magnetic drug delivery system shown in cross-section, a magnet is placed outside the body in order that its magnetic field gradient might capture magnetic carriers flowing in the circulatory system.

Once the drug/carrier is concentrated at the target, the drug can be released either via enzymatic activity or changes in physiological conditions such as pH, osmolality, or temperature, and be taken up by the tumour cells.^[5] The process of drug localization using magnetic delivery systems is based on the competition between forces exerted on the particles by blood compartment, and magnetic forces generated from the magnet, i.e. applied field. When the magnetic forces exceed the linear blood flow rates in arteries (10 cm s^{-1}) or capillaries (0.05 cm s^{-1}), the magnetic particles are retained at the target site and maybe internalized by the endothelial cells of the target tissue.^[44] This system, in theory, has major advantages over the normal, non-targeted methods of cytotoxic drug therapy. The physical principles underlying magnetic targeting therapy are similar to those used in magnetic separation, and are derived from the magnetic force exerted on a superparamagnetic nanoparticle by a magnetic field gradient. The effectiveness of the therapy is dependent on several physical parameters, including the field strength, gradient and volumetric and magnetic properties of the particles. As the carriers (ferrofluids) are normally administered intravenously or intra-arterially, hydrodynamic parameters such as blood flow rate, ferrofluid concentration, infusion route and circulation time also play a major role as do physiological parameters such as tissue depth to the target site (i.e. distance from the magnetic field source), reversibility and strength of the drug/carrier binding, and tumour volume.^[45] In general, larger particles

(e.g. magnetic microspheres, around 1 μm in diameter, comprising agglomerates of superparamagnetic particles) are more effective at withstanding flow dynamics within the circulatory system particularly in larger veins and arteries.

Preliminary investigations of the hydrodynamics of drug targeting suggest that for most magnetite-based carriers, flux densities at the target site must be of the order of 0.2 T with field gradients of approximately 8 Tm^{-1} for femoral arteries and greater than 100 Tm^{-1} for carotid arteries. This suggests that targeting is likely to be most effective in regions of slower blood flow, particularly if the target site is closer to the magnet source. As discussed above, there are several major advantages of using magnetic nanoparticles in drug delivery. First, drug bound magnetic nanoparticles can penetrate through small capillaries and be taken up by cells. Secondly, the movement of drug loaded magnetic nanoparticles can be readily controlled by an external magnetic field. Hence, accumulation of efficient drugs at the target sites can be achieved. Thirdly, biocompatible magnetic for example core-shell nanoparticles allow sustained drug release over a period of time. Fourthly, after being injected into bodies, the drug uptake process can be visualized by MRI. Finally, unlike searching for new molecules, magnetic drug delivery involves low-cost research, which reduces the cost of drug loaded product. Despite many merits, there are some problems associated with magnetic drug delivery. The major limitation of magnetic drug delivery systems is that the external magnetic field should be lowered to a certain level, higher than which living bodies cannot withstand. However, a magnetic field at this level may not generate magnetic gradient high enough to control the targeted movement of nanoparticles or trigger the drug desorption because the magnetic gradient decreases with the distance. This problem can be alleviated by locating an internal magnet near the target by minimally invasive surgery. Another problem which may occur in magnetic drug delivery is the possible agglomeration of magnetic nanoparticles, that may cause a tough embolization of the blood vessels in the treated area, especially after the removal of the applied magnetic field, due to their high surface energy.^[46] Further, smaller nanoparticles possess weaker magnetic force. Thus, the ultrasmall dimension of nanoparticles, which is required for superparamagnetism, may lead to difficult control of their movement or location in the

presence of a relatively strong drag force from the blood flow. Consequently, magnetic drug delivery is more effectively controlled in blood flows with lower velocities. Further, when applying this technique to human bodies, a magnetic field with a safe strength may not be effective due to the large distance between the target site and the magnet. Pre-clinical and experimental investigations have been carried out to overcome these limitations and improve the efficiency of magnetic drug delivery at a safe level.^[38]

1.4.2 Diagnostic applications

The diagnostic applications of magnetic nanoparticles are processes to detect malignant tissues or pathogenic bioaggregates by using magnetic nanoparticles.

MRI contrast enhancement. In life science, an emerging technology, molecular imaging, has been playing a substantial role in both scientific investigation and practical bioapplications. Molecular imaging is the technology that helps us to understand diseases and search for the appropriate treatments. Since most disease processes have a molecular basis, molecular imaging with sufficient image resolution and image contrast at the molecular level is much needed for better diagnostic differentiations, early disease detection and objective therapy monitoring with imaging biomarkers.^[47] There is a number of molecular imaging techniques available ranging from ultrasonic to gamma ray and X-ray frequencies in the electromagnetic spectrum. Molecular imaging operates at the interface between life science and physical science, and images are obtained by facilitating interaction with a biological entity at a molecular level. Thus, both the life and physical sciences are required to develop and implement a molecular imaging technique due to its diverse nature. Among them, optical imaging, nuclear imaging and magnetic resonance imaging (MRI) are the most widely used molecular imaging techniques. Magnetic nanoparticles are able to enhance the image contrast in MRI, which has attracted enormous attention. To better investigate the functions of magnetic nanoparticles as a contrast agent in MRI, it is necessary to first understand the working mechanism and physical principles in MRI. As far as the imaging mechanism of MRI is concerned, the technology is based on the detection of nuclear spin in molecules. When

the nuclei of protons are exposed to a strong magnetic field, their spins align either parallel or antiparallel to the magnetic field. During their alignment, the spins precess under a specified frequency, known as the Larmor frequency (ω_0), (figure 5(a)). When a 'resonance' frequency in the radio-frequency (RF) range is introduced to the nuclei, the protons absorb energy and are excited to the antiparallel state. After the disappearance of the RF pulse, the excited nuclei relax to their initial, lower-energy state (figure 5(b)). There are two different relaxation pathways. The first, called longitudinal or T1 relaxation, involves the decreased net magnetization (M_z) recovering to the initial state (figure 5(c)). The second, called transverse or T2 relaxation, involves the induced magnetization on the perpendicular plane (M_{xy}) disappearing by the dephasing of the spins (figure 5(d)). Based on their relaxation processes, the contrast agents are classified as T1 and T2 contrast agents. Commercially available T1 contrast agents are usually paramagnetic complexes, while T2 contrast agents are based on iron oxide nanoparticles, which are the most representative nanoparticulate agents^[49]

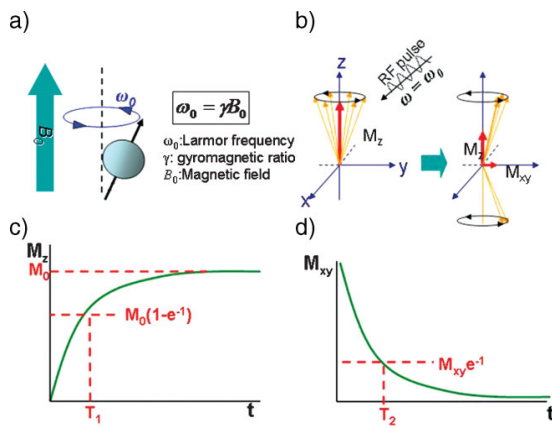


Figure 5. Principle of magnetic resonance imaging. (a) Spins align parallel or antiparallel to the magnetic field and precess under Larmor frequency (ω_0). (b) After induction of RF pulse, magnetization of spins changes. Excited spins take relaxation process of (c) T1 relaxation and (d) T2 relaxation.

The reason for using magnetic nanoparticles in MRI is to shorten both T1 and T2* (shorter relaxation time) so that the image contrast can be enhanced. Iron oxide nanoparticles have been tested for contrast enhancement in MRI. Superparamagnetic nanoparticles are magnetically saturated in the common magnetic fields applied in MRI, and they are able to create a substantial locally perturbing dipolar field, and hence successfully decrease the value of T1 and T2*. To further improve biocompatibility, iron oxide-based superparamagnetic nanoparticles are always coated by a biocompatible layer such as Dextran, PEG, SiO₂, DMSA, which can be excreted via the liver after treatment. In MRI, biofunctionalized magnetic nanoparticles are selectively taken up by the reticuloendothelial system, which serves as a network to remove foreign substances from the blood circulation system. It was found that magnetic nanoparticles with diameter less than 10 nm had a longer half-life than those of 30 nm in diameter or larger in the blood stream. Larger nanoparticles are recognized by liver and spleen, while smaller ones are collected by the reticuloendothelial system in healthy tissues throughout the body. It is the differential uptake of magnetic nanoparticles by different tissues that determines the MRI contrast. For tumor cells, the relaxation times are not changed by introducing contrast agent (magnetic nanoparticles) due to the absence of an effective reticuloendothelial system in the tumor. Therefore, identification of malignant lymph nodes, liver tumors and brain tumors by comparing the image contrast can be readily achieved in the presence of magnetic nanoparticles in MRI. It has been also noticed that iron oxide nanoparticles have the capability of being encapsulated into target-specific agents. Another type of common contrast agents T1 used in MRI is paramagnetic gadolinium ion complexes. Generally, magnetic labeling is employed by using fluorescent-labeled magnetic nanoparticles in both in vitro and in vivo imaging. The combination of nanoscale dimensions, superparamagnetic properties and fluorescence for these bifunctional nanoparticles has prompted their use in medical imaging which combines fluorescent imaging techniques and the MRI approach. Both methods are of great importance in diagnostic and therapeutic applications because cellular monitoring provides valuable information for subsequent cell-based therapy. The advantage of the MRI technique is well known: it offers anatomically sensitive deep

tissue imaging. As discussed above, magnetic resonance imaging is one of the most powerful medical tools for diagnostic purposes owing to its noninvasive process, high spatial resolution and multidimensional tomographic capabilities. However, this technique suffers from low-signal sensitivity. To overcome the weakness of current MRI techniques, signal enhancers need to be used. The signal-enhancing capabilities of magnetic nanoparticles/nanocrystals have been demonstrated. Magnetite (Fe_3O_4), as a member of clinically benign iron oxide-based nanoparticles, has been widely explored for signal-enhancing purposes.^[38]

Magnetic Separation and Purification. In modern biology or biomedicine, separation of particular biological entities (e.g. DNA, proteins, ions, molecules, etc.) from their native environment is often required for both scientific investigation and practical uses. Magnetically labeled biological entities exhibit magnetic properties so that they can be separated by applying an external magnetic field. Due to this reason, magnetic separation and purification have been widely used to prepare concentrated bio-samples in biomedical applications. A typical magnetic separation usually contains two steps: labeling desired biological entities with magnetic materials and separating magnetically tagged entities via a magnetic separation device. To ensure an effective labeling, functionalization needs to be performed to deposit biocompatible molecules on magnetic nanoparticles. The organic or inorganic coating not only provides a link between the particles and target biological entities, but improves the colloidal stability. A highly effective method of labelling cells is via antibody/antigen bonding due to its specific binding characteristics. By this technique, various biological entities (e.g. cancer cells, bacteria, red blood cells, Golgi vesicles, etc) have been demonstrated binding to immunospecific agents-coated magnetic nanoparticles. Similarly, magnetic microparticles can also be used for larger entities when incorporated in a polymer binder. In the second step of magnetic separation, when the mixture passes through a magnetic field, magnetic labeled targeted materials immobilize because of the force due to the magnetic field gradient and separate from the native solution. Due to the magnetic properties of magnetic-labeled biomolecules, magnetic separation may be

achieved by simply using a permanent magnet to aggregate magnetic entities on the wall of a test tube followed by removal of the supernatant. This simple process is illustrated in *figure 6(a)*.

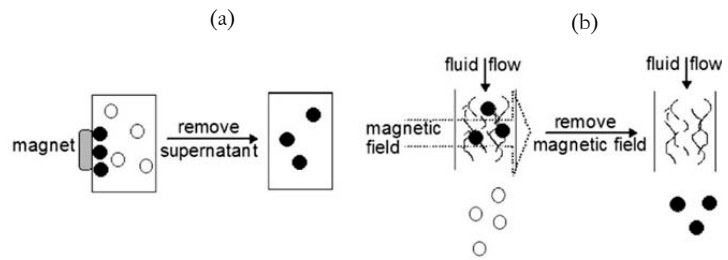


Figure 6. Schematic of two standard methods for magnetic separation. (a) A magnet is placed close to the container wall of a solution containing magnetically tagged (●) and unwanted (○) biomaterials. Due to the magnetic force exerted the tagged particles are attracted by the magnet and agglomerate while the unwanted biomaterials can be removed with the supernatant solution; (b) a solution containing tagged and unwanted biomaterials flows continuously through a region with strong magnetic field gradient which can be provided by packing the column with steel wool. Thus the tagged particles can be attracted. Afterwards, the tagged particles can be collected after removing the field followed by flushing through with water.

However, this method is suffering from its low separation efficiency because of the slow accumulation rates. Thus better magnetic separation is needed. A common method of achieving high separation efficiency is to use a magnetizable matrix of wire or beads to apply a strong magnetic field on a flow column through which magnetically tagged fluid is pumped. The type of separator design is able to generate high magnetic field gradient and capture the magnetic biological entities efficiently as they flow with their carrier medium. *Figure 6(b)* depicts the schematic of this process. In spite of its faster separation, this method, however, has some problems caused by the settling and adsorption of magnetic materials on the matrix. To overcome this problem, an alternative separation design was developed, as shown in *figure 7*.

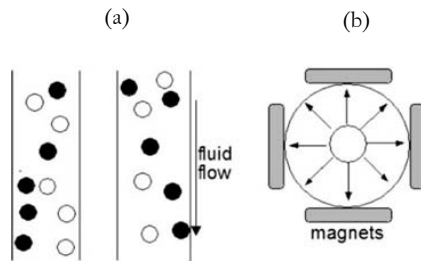


Figure 7. Schematic illustration of a rapid throughput method for magnetic separation. In this method, a solution containing magnetically tagged (●) and unwanted (○) biomaterials flows through an annular column placed within a set of magnets arranged in quadrature. (a) Longitudinal cross-section view of the annular column showing the flow of the solution; (b) transverse cross-section view of the four magnets with the resulting magnetic field lines. Under the magnetic force due to the magnetic field gradient, the tagged particles are attracted to the column walls, where they are held until the field is removed. The held tagged biomolecules can be recovered by flushing the column with water.

In this design, a magnetic gradient is created radially outwards from the center of the flow column by a quadrupolar arrangement. So obstruction will not take place during the separation. Additionally, biological entities with different magnetophoretic mobilities can be fractionated to achieve ‘fluid flow fractionation’ by adjusting the magnitude of the field gradient. In a typical separation process, the applied magnetic field is moved up the column while the fluid is kept static. Consequently, the particles can be moved up by the magnetic force and collected by a permanent magnet. The bottom section of fluid is then subjected to repeat separation processes with different magnetic strengths. Magnetic separation can be used with optical sensing to perform ‘magnetic enzyme linked immunosorbent assays’. Immuno-assays, combined with fluorescent enzymes, are able to detect cells labeled by the enzymes. In contrast to a conventional means in which the target cells need to bind to a solid matrix, magnetic-assisted immunosorbent assays utilize magnetic microspheres as the surface for cell immobilization. Importantly, magnetic separation is typically used to increase the concentration of the target materials. Recently, magnetic nanoparticles have been employed in this assay application. The use of nanoparticles improves the magnetic separation efficiency because their high mobility results in a short reaction time and

more immobilized reagent. Furthermore, magnetic separation offers an effective way to localize labeled cells at certain locations, which is of great help for cell detection and number counting by optical scanning.^[3, 38]

References

- [1] B.L. Cusching, V.L. Kolesnichenko, C.J. O'Connor, *Recent Advances in the Liquid-Phase Syntheses of Inorganic Nanoparticles*. Chem. Rev. **2004**, 104, 3893-3946.
- [2] C. Corit, P. Robert, J.M. Idee, M. Port, *Recent advances in iron oxide nanocrystal technology for medical imaging*. Advanced Drug Delivery Reviews, **2006**, 58, 1471-1504.
- [3] Q.A. Pankhurst, J. Connolly, S.K. Jones, J. Dobson, *Applications of magnetic nanoparticles in biomedicine*. Journal of Physics. D, Applied Physics, **2003**, 36, 167-181.
- [4] P. Pradhan, J. Giri, R. Banerjee, J. Bellare, D. Bahadur, *Preparation and characterizations of manganese ferrite based magnetic liposomes for hyperthermia treatment of cancer*. J. Magn. Magn. Mater., **2007**, 311, 208-215.
- [5] Q.A. Pankhurst, *Nanomagnetic medical sensors and treatment methodologies*. BT Technology Journal, **2006**, 24, 33-38.
- [6] P. Tartaj, M.P. Morales, T. González-Carreño, S. Veintemillas-Verdaguer, C.J. Serna, *Advances in magnetic nanoparticles for biotechnology applications*. Journal of Magnetism and Magnetic Materials, **2005**, 28-34.
- [7] M. Ferrari, *Cancer nanotechnology: opportunities and challenges*. Nature Reviews, Cancer, **2005**, 5, 161-171.
- [8] S.A. Wickline, A.M. Neubauer, P.M. Winter, S.D. Caruthers, G.M. Lanza, *Molecular imaging and therapy of atherosclerosis with targeted nanoparticles*. Journal of magnetic Resonance Imaging, **2007**, 25, 667-680.
- [9] C. Corot, K.G. Petry, R. Trivedi, A. Saleh, C. Jonkmanns, J.F. Le Bas, E. Blezer, M.Rausch, B. Brochet, P. Foster-Gareau, D. Baleriaux, S. Gaillard, V. Dousset, *Macrophage imaging in central nervous system and in carotid atherosclerotic plaque using ultrasmall superparamagnetic iron oxide in magnetic resonance imaging*. Investigative Radiology, **2004**, 39, 619-625.
- [10] C. Sun, J. S.H. Lee, M. Zhang, *Magnetic nanoparticles in MR imaging and drug delivery*. Advanced Drug Delivery Reviews, **2008**, 60, 1252-1265.

- [11] M.R. Mourino, *From Thales to Lauterbur, or from the lodestone to MR imaging: magnetism and medicine*. Radiology, **1991**, 180, 593-612.
- [12] A. Morrish, *The Physical Principles of Magnetism*. IEEE Press, New York, **2001**.
- [13] A.H. Lu, E.L. Salabas, F. Schuth, *Magnetic nanoparticles: synthesis, protection, functionalization, and application*. Angewandte Chemie. International Edition, **2007**, 46, 1222-1244.
- [14] X.M. Lin, A.C.S. Samia, *Synthesis, assembly and physical properties of magnetic nanoparticles*. Journal of Magnetism and Magnetic Materials, **2006**, 305, 100-109.
- [15] C. Cannas, A. Musinu, A. Ardu, F. Orrù, D. Peddis, M. Casu, R. Sanna, F. Angius, G. Diaz, G. Piccaluga, *CoFe₂O₄ and CoFe₂O₄/SiO₂ Core/Shell Nanoparticles: Magnetic and Spectroscopic Study*. Chem. Mater., **2010**, 22, 11, 3353-3361.
- [16] D. Peddis, F. Orrù, A. Ardu, C. Cannas, A. Musinu, G. Piccaluga, *Interparticle Interactions and Magnetic Anisotropy in Cobalt Ferrite Nanoparticles: Influence of Molecular Coating*. Chem. Mater., **2012**, 24, 6, 1062-1071.
- [17] A.R. West, *Solid State Chemistry and its Applications*, Series, **1984**.
- [18] L. Suber, D. Peddis, *Approaches to Synthesis and Characterization of Spherical and Anisometric metal Oxide Magnetic Nanoparticles*. Nanomaterials for the Life Sciences Vol.4: Magnetic Nanomaterials, Wiley-VCH, **2009**.
- [19] S. Stolnik, L. Illum, S.S. Davis, *Long circulating microparticulate drug carriers*. Adv. Drug Del. Rev., **1995**, 16, 195-214.
- [20] A.K. Gupta, S. Wells, *Surface modified superparamagnetic nanoparticles for drug delivery: preparation, characterization and cytotoxicity studies*. IEEE Trans Nanobioscience, **2004**, 3, 1, 66-73.
- [21] C.J. Brinker, *Sol-Gel Science*. Academic Press, San Diego, **1990**.
- [22] C. Cannas, A. Falqui, A. Musinu, G. Piccaluga, D. Gatteschi, C. Sangregorio, G. Concas, G. Spano, *Superparamagnetic behaviour of γ -Fe₂O₃ nanoparticles dispersed in a silica matrix*. Chem. Phys., **2001**, 3, 832-838.
- [23] R. Massart, V. Cabuil, J. Chim. Phys., **1987**, 84, 967.

- [24] A.K. Gupta, M. Gupta, *Synthesis and surface engineering of iron oxide nanoparticles for biomedical applications*. *Biomaterials*, **2005**, 26, 3995-4021.
- [25] S. Sun, H. Zeng, D.B. Robinson, S. Raoux, P.M. Rice, S.X. Wang, G. Li, *Monodisperse MFe_2O_4 (M= Fe, Co, Mn) Nanoparticles*. *J. Am. Chem. Soc.*, **2004**, 126, 273-279.
- [26] X. Hu, J.C. Yu, J. Gong, *Fast production of self-assembled hierarchical- Fe_2O_3 nanoarchitectures*. *J. Phys. Chem. C*, **2007**, 111, 11180-11185.
- [27] C. Solans, P. Izquierdo, J. Nolla, N. Azemar, M.J. Garcia-Celma, *Nano-emulsions*. *Curr. Opin. Colloid Interface Sci.*, **2005**, 10, 102-110.
- [28] C. Cannas, A. Ardu, D. Peddis, C. Sangregorio, G. Piccaluga, A. Musinu, *Surfactant-assisted route to fabricate $CoFe_2O_4$ individual nanoparticles and spherical assemblies*. *Journal of Colloid and Interface*, **2010**, 343, 415-422.
- [29] J.H. Bang, K.S. Suslick, *Sonochemical Synthesis of Nanosized Hollow Hematite*. *J. Am. Chem. Soc.*, **2007**, 129, 2242-2243.
- [30] L. Cabrera, S. Gutierrez, N. Menendezb, M.P. Morales, P. Herrasti, *Magnetite nanoparticles: Electrochemical synthesis and characterization*. *Electrochim. Acta*, **2008**, 53, 3436-3441.
- [31] C. Pascal, J.L. Pascal, F. Favier, M.L.E. Moubtassim, C. Payen, *Electrochemical synthesis for the control of gamma- Fe_2O_3 nanoparticles size. Morphology, microstructure, and magnetic behavior*. *Chem. Mater.*, **1999**, 11, 1, 141-147.
- [32] O. Bomati-Miguel, L. Mazeina, A. Navrotsky, S. Veintemillas-Verdaguer, *Calorimetric Study of Maghemite Nanoparticles Synthesized by Laser-induced Pyrolysis*. *Chem. Mater.*, **2008**, 20, 2, 591-598.
- [33] N.A. Kotov, I. Dekany, J.H. Fendler, *Layer-by-layer self assembly of polyelectrolyte-semiconductor nanoparticle composite films*. *J. Phys. Chem.*, **1995**, 99, 13065-13069.
- [34] J. Park, J. Joo, S.G. Kwon, Y. Jang, T. Hyeon, *Synthesis of monodisperse spherical nanocrystals*. *Angewandte Chemie*, **2007**, 46, 4630-4660.
- [35] N.R. Jana, Y. Chen, X. Peng, *Size and shape-controlled magnetic (Cr, Mn, Fe, Co, Ni) oxide nanocrystals via a simple and general approach*. *Chem. Mater.*, **2004**, 16, 3931-3935.

- [36] A.G. Roca, R. Costo, A.F. Rebolledo, S. Veintemillas-Verdaguer, P. Tartaj, T. González-Carreño, M.P. Morales, C.J. Serna, *Progress in the preparation of magnetic nanoparticles for applications in biomedicine*. J. Phys. D: Appl. Phys., **2009**, 42, 1-11.
- [37] P. Tartaj, M. del Puerto Morales, S. Veintemillas-Verdaguer, T. González-Carreño, C. J Serna, *The preparation of magnetic nanoparticles for applications in biomedicine*. J. Phys. D: Appl. Phys., **2003**, 36, 182-197.
- [38] V. K. Varadan, L.F. Chen, J. Xie, *Nanomedicine: Design and Applications of Magnetic Nanomaterials, Nanosensors and Nanosystem*. John Wiley & Sons, **2008**, 1-484.
- [39] M.A. El-Sayed, *Some Interesting Properties of Metals Confined in Time and Nanometer Space of Different Shapes*. Acc. Chem. Res., **2001**, 257-264.
- [40] R. Hiergeist, W. Andra, N. Buske, R. Hergt, I. Hilger, U. Richter, W. Kaiser, *Application of magnetite ferrofluids for hyperthermia*. J. Magn. Mater., **1999**, 201, 420-422.
- [41] A. Jordan, R. Scholz, P. Wust, H. Fähling, R. Felix, *Magnetic fluid hyperthermia (MFH): Cancer treatment with AC magnetic field induced excitation of biocompatible superparamagnetic nanoparticles*. Journal of Magnetism and Magnetic Materials, **1999**, 201, 413-419.
- [42] P. Moroz, S.K. Jones, B.N. Gray, *Magnetically mediated hyperthermia: current status and future directions*. International Journal of Hyperthermia, **2002**, 18, 267-284.
- [43] W.J. Atkinson, I.A. Brezovich, D.P. Chakraborty, *Usable Frequencies in Hyperthermia with Thermal Seeds*. IEEE T Bio-Med Eng., **1984**, 31, 70-75.
- [44] J.C. Joubert, *Magnetic Microcomposites as Vectors for Bioactive Agents: The State of Art*. An. Quim. Int. Ed., **1997**, 93, 70-76.
- [45] A.S. Lübbe, C. Bergemann, J. Brock, D.G. McClure, *Physiological aspects in magnetic drug-targeting*. J. Magnetism and Magnetic Materials, **1999**, 194, 149-155.
- [46] M. Arruebo, R. Fernandez-Pacheco, M.R. Ibarra, J. Santamaria, *Review: Magnetic nanoparticles for drug delivery*. Nanotoday, **2007**, 2, 22-32.
- [47] P.J. Cassidy, G.K. Radda, *Molecular imaging perspectives*. J. Roy Soc. Interface, **2005**, 2, 133-144.

[48] H. Bin Na, I.C. Song, T. Hyeon, *Inorganic Nanoparticles for MRI Contrast Agents*. *Adv. Mater.*, 2009, 21, 2133-2148.

Superparamagnetic nanoparticles have been widely used for numerous in vitro and in vivo applications. All these biomedical and bioengineering applications require that these nanoparticles need special surface coating of the magnetic nanoparticles, which has to be not only non-toxic and biocompatible but also allow a targetable delivery with particle localization in a specific area. This chapter focuses on the surface modification of the magnetic nanoparticles through organic and inorganic coatings. The type of specific coating depends on the end application and should be chosen by keeping a particular application in mind.

Chapter 2

Magnetic Nanoparticles:

Surface Modification and Silica Nanocomposite

2.0 Surface modification of magnetic nanoparticles

2.1 Introduction

Superparamagnetic iron oxide nanoparticles with appropriate surface chemistry have been widely used experimentally in biomedical field. The biomedical and bioengineering applications require that these nanoparticles have high magnetization values and size smaller than 100 nm with overall narrow particle size distribution, so that the particles have uniform physical and chemical properties.^[1] In addition to these applications, the development of methods aimed at the post-synthetic surface modification of magnetic nanoparticles is important to render them not only non-toxic, biocompatible, soluble in water, but chemically functional, and thus allow a targetable delivery with particle localization in a specific area. Several magnetic oxides have been synthesized using water-based methods like coprecipitation, oil in water microemulsions or micelles strategies, hydrothermal and sonochemistry processes.^[2,3,4,5,6] The disadvantage of these aqueous solution syntheses is that the nanoparticle quality, more specifically their size and shape uniformity and in some cases crystallinity, is rather poor. About ten year ago, a new synthetic procedures have been developed to obtain scalable preparative routes

for high-quality magnetic nanoparticles,^[7] that could be synthesized by thermal decomposition of different types of iron precursors such as iron acetylacetonate,^[8,9] iron pentacarbonyl,^[10] and iron-oleate,^[11] in the presence of surfactants, such as oleic acid and oleylamine. The nanoparticles resulting from this procedure are stable in nonpolar solvents (such as hexane or cyclohexane) and capped with nonpolar end-groups on their surface. The capping molecules (also called ligands) are typically long-chain alkanes with polar groups that bind to the nanoparticles' surface. Although the thermal decomposition method has the advantage of producing very monodisperse particles, it has the big disadvantage that the resulting nanoparticles are only dispersible in nonpolar solvents, which to some extent limits their applications in biological fields. Hence, to make ferrite magnetic nanoparticles suitable for biological applications, the hydrophobic surfactant coating needs to be replaced by a hydrophilic, biocompatible, and functional coating that allows controlled interaction with biological species. In literature recently lot of work has been made in this direction; hydrophobic magnetic nanoparticles have been coated with organic or inorganic systems.^[9,12-14]

2.2 Surface modification

The colloidal stabilization of the magnetic nanoparticles in both aqueous and physiological medium is crucial for their therapeutic applications and can be achieved by either charging the surface or conjugating it by macromolecules for steric hindrance. The surface charge can be monitored and ensured by suitable means such as changing pH of the medium or modifying with functional groups. The steric stabilization can be achieved by attaching/grafting of organic small molecules, macromolecules, and inorganic coating on the surface. The steric stabilization is indeed less sensitive to the ionic strength of the suspension medium and can be easily achieved in both polar and non-polar medium. The oxide nanoparticles may be stabilized either during their synthesis or in a post-synthesis process. The in situ modification during synthesis process has several advantages including reduced agglomeration.^[15]

2.2.1 Organic coating

The binding affinity of large surfactant molecules or long polymer chains to the nanoparticles may be lost due to steric hindrances, which could otherwise be easily overcome by using small molecules having multiple functional groups such as carboxyl (COOH), amine (NH₂), thiol (SH), phosphate and sulfates. These stabilizers can be tailored for dispersibility into aqueous media or other biocompatible fluids. The presence of hydroxyl groups on the surface of oxide nanoparticles provides a versatile route for multiple functionalities. Furthermore, the presence of a large number of functional groups on the surface of nanoparticles may be used for linkage of various biomolecules as well as drugs. Among various small molecules, *citrate* moiety having multiple carboxylate functionalities,^[17] *aminesilane* for amine groups used as stabilizing agent,^[18] and *dimercaptosuccinic acid* (DMSA), because having thiol functionality achieved great deal of attention due to their higher binding affinity towards metal and metal oxide nanoparticles.^[19]

Macromolecules. A variety of polymer molecules have been used for steric stabilization of oxide nanoparticles in aqueous and high ionic strength media.^[20] The polymer shell improves the stability of nanoparticles in solution and allows the encapsulation of a therapeutic agent. Further, these stabilizers provide a means to tailor the surface properties of nanoparticles such as surface charge and chemical functionality or their thermosensitive properties. Major factors with regard to polymeric stabilizer that may affect the performance of nanocarriers include the chemical nature of the polymer (i.e., hydrophilicity/hydrophobicity, biocompatibility and biodegradation), the molecular weight of the polymer, the manner in which the polymer is grafted or attached (i.e., physically or chemically), the conformation of the polymer and the degree of particle surface coverage. Among various macromolecules, *dextran* has been widely used for surface modification mostly because of its favorable size (chain length) and biocompatibility, which enables optimum polar interactions (mainly chelation and hydrogen bonding). Dextran coating not only provides a smooth outline and narrow size distribution but also retains the essential superparamagnetic behavior of iron oxide

nanoparticles and a significantly prolonged the storage stability.^[21] PEG is hydrophilic, water-soluble, biocompatible polymer and extensively used to increase blood circulation times.^[22]

Other coating. The amphiphilic molecules such as *liposomes* have been successfully used to stabilize oxide nanoparticles for therapeutic application.^[23] Liposomes have also the ability to encapsulate a large number of nanoparticles and deliver them together to the specific target site. Both hydrophilic and hydrophobic foreign molecules such as drugs and biomolecules can be easily anchored to the amphiphilic liposomes which can enhance the multifunctionality of a system.

2.2.2 Mechanisms of surface modification by organic molecules

Ligand exchange. This is an alternative method for tuning the surface properties of nanoparticles. The concept of ligand exchange is very simple: mixing nanoparticles with the free ligands results in replacement of outgoing ligands with the incoming ones.^[24] Exchanging weakly bound ligands for strongly binding ligands is to replace a strongly bound ligand with a ligand present in high concentration during the exchange procedure. This drives the equilibrium towards the thermodynamically less stable nanoparticles (NP) coated with weakly binding ligands; thus satisfying Le Chatelier's principle:

$$K = \frac{[NP - X_n][Y]^m}{[NP - X_m][X]^n}$$

where n and m are the number of molecules of X and Y respectively.^[25]

The position of this equilibrium depends on the properties of the incoming and outgoing ligand. If the ligands have similar structure, the equilibrium constant is close to 1.^[26] For functionalized ligands, however, the situation becomes much more complicated. The true equilibrium may be difficult to achieve as there are some very slow processes on the nanoparticle surface which do not go to completion even after many days. These processes can disturb the apparent equilibrium position. The exact number of ligands

per nanoparticle is often unknown, and not all ligands can be exchanged; this makes accurate determination of the equilibrium constant difficult. Additionally, the position of equilibrium seems to depend on the exact ratio of incoming to outgoing ligands, presumably due to the different reactivity of different binding sites on the nanoparticles surface.^[24] The main advantages of the method are the simplicity and the fact that the process not increase the size of the nanoparticles due to the small size of the exchange agents such as silanes,^[27] tetramethylammonium hydroxide,^[28] silsesquioxane,^[29] carboxylic,^[30] phosphonic,^[31] mercaptoalkanoic acids,^[32] and polymers.^[25] However, this method relies on the exchange of the surfactant coating ligands with the substitutional molecule of which one end carrying a functional group that is reactive toward the nanocrystal surface and the other end carrying a hydrophilic group as carboxylic or sulfonic acid, that are found to stabilize the particles for longer time.^[34] Due to the relatively high prevalence of potential ligands in vivo, including thiols, carboxylic acids, peptides, sugars and phosphates; ligands on nanoparticles intended for in vivo use must have a high enough affinity for the nanoparticles that they will not undergo significant exchange with these species. The stability of ligand shells is governed by many of the same factors that stabilize self-assembled monolayers. Stability is dominated by the strength of the ligand-surface bond, but the ability of the ligand tails to pack in an ordered fashion is also significant. The structure and hence the stability of a ligand shell can be altered by the position of a single methyl group,^[35] the presence or absence of a single unsaturated bond^[36] or other packing factors such as chain length^[37] and π - π stacking.^[38] The concentration of free ligands available to form a monolayer also influences the ligand orientation and hence degree of stabilization afforded.^[39] Light induced reactions at the nanocrystals/ligand interface can also often lead to desorption of the ligands.^[25,40] In aqueous solution, the ligand-nanoparticle interaction is basically the same but a number of different effects important for stability arise. Most commonly, hydrophilic nanoparticles are stabilized by electrostatic repulsion by the equally charged ligand molecules on the particle surface. However, in the presence of high salt concentration the electric field is shielded and the nanoparticles can come close to each other until eventually attractive forces cause the particles to agglomerate, as induced

dipole interaction, Van-Der-Waals force, or hydrogen bonds.^[41] Depending on the isoelectric point (pI) and the pH of the solution, nanoparticles can also lose or change the sign of their charge.

In conclusion, ligand exchange in nanoparticles can be compared with ligand substitution reactions in metal complex,^[25] but in reality the mechanism appears to be more complex. Indeed the nanoparticles have a electronic structure very complex and hardly comparable with that of mononuclear complex, and on the success of ligand exchange process also depends on the shape, the size, the polydispersity of nanoparticles size, and from their high degree of packing and crystalline order.

Intercalation. Another strategy used to convert hydrophobic nanoparticles in hydrophilic is to create a system of forces and hydrophobic interactions causes the hydrocarbon chains to intercalate, forming a new bilayers. In this way, the ligand bilayer allows one to transfer hydrophobic particles from the organic solvents to aqueous phase. The molecules acting as phase-transfer agents have to be amphiphilic, comprise a hydrophobic and a hydrophilic part, commonly one or more aliphatic chains and a polar, often charged, end group. One common class of such surfactants for the transfer from organic to aqueous phase are quaternary ammonium salts in which four hydrocarbon chains are bound to a nitrogen atom that is thus positively charged, the counter ions usually being chloride or bromide.

2.2.3 Inorganic coating

Silica (SiO₂), *gold* (Au)^[33] and *silver* (Ag) are extensively used for surface modification of the oxide nanoparticles which forms core-shell structures, and provides stability to the nanoparticles in solution and further help in binding various biological molecules and drugs to the surface of nanoparticles through suitable functional groups. There has been considerable interest in stabilizing oxide nanoparticles with noble metal shells such as Au and Ag. The magnetic oxide nanoparticles with metal coating can be effectively stabilized in corrosive biological conditions and can be readily functionalized through

the well-established metal-sulfur chemistry. The magnetic core-shell nanoparticles with tunable plasmonic properties have great potential for nanoparticle-based diagnostic and therapeutic applications.^[42]

The stabilization of oxide nanoparticles by silica can easily be achieved either by Stöber process or microemulsion method.^[9,43]

2.2.4 Silica coating

Silica has been exploited as a coating material for magnetic nanoparticles for the following advantages:

- synthesis as well as physical and chemical properties of colloidal silica are well documented;
- is chemically stable in most solvents and can be exposed to high temperatures;
- is highly stable in water;
- its surface is easily functionalizable;
- show low toxicity (size dependent);
- provides protection against chemical degradation of the magnetic core and prevent the release of potentially toxic components of the core;
- the thickness of the coating can be tuned;
- the porosity as well as the order of the pores can be controlled.

In particular, mesoporous materials are a promising candidate in many applications due to their extraordinary properties such as monodisperse and tunable pore size, high surface area and pore volume in an inert and biocompatible matrix having a surface that is easily modified. Combining mesoporous silica with magnetic nanoparticles produces a nanocomposite system that can be manipulated through the use of a magnetic field. The major advantage on the application of the composites for biomedical purposes is that they can show multiple properties integrated in the same material, such as fluorescence, magnetism, cellular labelling, and/or therapeutic functions. These materials can be

moved quickly to specific target locations, in-vivo or in-vitro, and have a significant potential in drug delivery, medical diagnostics, and magnetic resonance imaging.^[44]

In cases where attempts have been made to embed magnetic centers into mesoporous silica nanoparticles, the synthesized materials suffer from insufficient magnetic contrast achieved due to the low mass percentage (<1%) of incorporated magnetic nanoparticles or destruction of the well-ordered, high surface area character of the silica structure. The resulting low magnetic response is due to the thick mesoporous silica shell^[45] or the large size of the mesoporous silica nanoparticles^[46] and suggests that a large dose (e.g. 175 mg or 500 mg magnetic nanoparticles/kg) would have to be injected, for example, to perform in vivo magnetic resonance imaging (MRI).^[47] To date, these shortcomings largely limit the practical use for in vivo biomedical applications. To realize the full potential of multifunctional magnetic mesoporous silica nanoparticles, a synthesis must be designed that produces small, easily dispersed, and well-ordered silica particles with higher mass percentage of incorporated magnetic centers.^[48]

Mesoporous silica can be also used as an ideal matrix to produce fluorescent particles that find a broad range of applications that involve tagging, tracing, and labeling.^[45,49] A myriad of organic (dyes, pigments) and inorganic (dyes, pigments, quantum dots, luminescent nanoparticles) fluorescent materials have been developed. Fluorescence of colloidal particles is typically achieved by incorporating either inorganic or organic fluorescent materials into a matrix. Inorganic dyes are typically more stable against oxidation and photobleaching. However, their limited variety, relatively low quantum yields, and limited compatibility restrict their broad utilization. The large variety of organic dyes, their high quantum yields, their absence of blinking, their excellent aqueous stability, and their relatively low toxicity make them attractive for use in fluorescent particles. The main problem associated with organic dyes is their relatively fast photobleaching. Some dyes can interfere with some biological processes. Sealing organic dyes into a silica matrix seems to be one of most promising approaches because of the wide compatibility of silica with other-including biological-materials. Hence, it is plausible to expect straightforward functionalization of fluorescent silica particles with various sensing molecules to give the particles preference for adhering to specific

molecules or materials.^[50] Recently, a novel synthesis of one-step self-assembly of mesoporous silica particles with encapsulated organic dyes was proposed.^[51,52] It is a templated sol-gel self-assembly of mesoporous particles with fluorescent dye added in relatively large concentrations (up to 0.01M) to the synthesizing bath. The dye molecules are physically entrapped inside 2-4 nm diameter mesochannels during the synthesis. In some cases, physical encapsulation of the fluorescent dyes creates also a problem. For example, open pore particles cannot protect the dye^[53] from leaking. Encapsulation within special mesoporous silica particles (origami-particles),^[51,52] which have self-sealed cylindrical pores, shows virtually no leakage of the dyes out of the particles.^[54] Another possibility is to seal the pores of the silica nanoparticles with an external coating layer of PEG, which further increases their stability in solution.^[47] The combination of a magnetic and a fluorescent entity may provide a new two-in-one multifunctional nanomaterials with a broad range of potential applications. First of all, multi-modal magnetic-fluorescent assays would be very beneficial for in vitro and in vivo-bioimaging applications such as MRI and fluorescence microscopy. Second of all, these nanocomposites can be utilised as agents in nanomedicine. For example, one of their most promising applications is a bimodal anticancer therapy, encompassing photodynamic and hyperthermic capabilities. Fluorescent-magnetic nanocomposites can also serve as an all-in-one diagnostic and therapeutic tool, which could be used, for example, to visualise and simultaneously treat various diseases. Another exciting application of magnetic-fluorescent nanocomposites is in cell tracking, cytometry and magnetic separation, which could be easily controlled and monitored using fluorescent microscopy. Finally, these nanocomposites can be used as nano-blocks to build various nanoelectronic and photonic devices by applying an external magnetic field to manipulate or arrange the magnetic nanoparticles and using fluorescence confocal microscopy to visualise and control their positioning. Thus magnetic-fluorescent nanocomposites are very promising materials, but there are some challenges to overcome in their fabrication. One of the main obvious problems is the complexity in the preparation of these nanocomposites, which frequently involves a multi-step synthesis and many purification stages. Therefore, the production of magnetic-fluorescent

nanocomposites is quite technically and time demanding. A specific difficulty in the preparation of two-in-one magnetic fluorescent nanocomposites is the risk of quenching of the fluorophore on the surface of the particle by the magnetic core. In addition, if there are a number of fluorescent molecules attached to the surface of the particle they may act to quench each other. There are several reasons for choosing mesoporous silica as a coating for magnetic particles in the fabrication of fluorescent-magnetic nanocomposites. First of all, the mesoporous silica coating provides an effective barrier to quenching of any fluorophores by the magnetic cores. In fact quenching can be controlled by the thickness of the silica shell. Second of all, the mesoporous silica is relatively inert and optically transparent allowing incorporation of fluorescent dyes or QDs directly into the silica spheres.^[55] Recently, the union of near-infrared fluorescent (NIRF) dyes with magnetic nanoparticles has received significant attention due to the deep penetration of NIRF light through tissues. The integration of NIRF detectability may allow for these magneto-optic nanocomposites to be used for both presurgical planning by MRI and intraoperative resection of malignant tissues by optical imaging. Since both MRI and optical signals come from the same nanocomposites, the MR image can serve as a roadmap to the fluorescently labeled tumor cells.^[56]

References

- [1] A.K. Gupta, M. Gupta, *Synthesis and surface engineering of iron oxide nanoparticles for biomedical applications*. *Biomaterials*, **2005**, 26, 3995-4021.
- [2] P. Tartaj, M.P. Morales, S. Veintemillas-Verdaguer, T. González-Carreño, C.J. Serna, *The preparation of magnetic nanoparticles for applications in biomedicine*. *J Phys D: Appl Phys.*, **2003**, 36, 182-197.
- [3] C. Cannas, A. Ardu, D. Peddis, C. Sangregorio, G. Piccaluga, A. Musinu, *Surfactant-assisted route to fabricate CoFe_2O_4 individual nanoparticles and spherical assemblies*. *Journal of Colloid and Interface Science*, **2010**, 343, 415-422.
- [4] Kannan M. Krishnan, *Biomedical Nanomagnetism: A Spin Through Possibilities in Imaging, Diagnostics, and Therapy*. *Ieee Transactions on Magnetism*, **2010**, 46, 7, 2523-2558.
- [5] S. Laurent, D. Forge, M. Port, A. Roch, C. Robic, L. Vander Elst, R.N., Muller, *Magnetic Iron Oxide Nanoparticles: Synthesis, Stabilization, Vectorization, Physicochemical Characterizations, and Biological Applications*. *Chem. Rev.*, **2008**, 108, 2064-2110.
- [6] A.H. Lu, E.L. Salabas, F. Schüth, *Magnetic nanoparticles: Synthesis, Protection, Functionalization, and Application*. *Angew. Chem. Int. Ed.*, **2007**, 46, 1222-1244.
- [7] T. Hyeon, *Chemical synthesis of magnetic nanoparticles*. *Chem. Commun.*, **2003**, 8, 927-934.
- [8] Shouheng Sun, Hao Zeng, *Size-Controlled Synthesis of Magnetite Nanoparticles*. *J. Am. Chem. Soc.*, **2002**, 124, 8204-8205.
- [9] C. Cannas, A. Musinu, A. Ardu, F. Orrù, D. Peddis, M. Casu, R. Sanna, F. Angius, G. Diaz, G. Piccaluga, *CoFe_2O_4 and $\text{CoFe}_2\text{O}_4/\text{SiO}_2$ Core/Shell Nanoparticles: Magnetic and Spectroscopic Study*. *Chem. Mater.*, **2010**, 22, 3353-3361.
- [10] T. Hyeon, S.S. Lee, J. Park, Y. Chung, Bin Na H., *Synthesis of Highly Crystalline and Monodisperse Maghemite Nanocrystallites without a Size-Selection Process*. *J. Am. Chem. Soc.*, **2001**, 123, 12798-12801.
- [11] J. Park, K. An, Y. Hwang, H.J. Noh, J.Y. Kim, J.H. Park, N.M. Hwang, T. Hyeon, *Ultra-large-scale syntheses of monodisperse nanocrystals*. *Nat. Mater.*, **2004**, 3, 891-895.

- [12] Gao J., Gu H., Xu B., *Multifunctional magnetic nanoparticles: design, synthesis, and biomedical applications*. Acc. Chem. Res., **2009**, 42, 1097-1107.
- [13] Pellegrino T., Manna L., Kudera S., Liedl T., Koktysh D., Rogach A.L., Keller S., Rädler J., Natile G., Parak W.J., *Hydrophobic nanocrystals, coated with an amphiphilic polymer shell: A general route to water soluble nanocrystals*. Nano Lett., **2004**, 4, 703-707.
- [14] Yang P., Ando M., Murase N., *Encapsulation of emitting CdTe QDs within silica beads to retain initial photoluminescence efficiency*. Journal of Colloid and Interface Science, **2007**, 316(2), 420-427.
- [15] Hu, F.Q., Wei, L., Zhou Z., Ran Y.L., Li Z., Gao M.Y., *Preparation of biocompatible magnetite nanocrystals for in vivo magnetic resonance detection of cancer*. Adv. Mater., **2006**, 18, 2553-2556.
- [16] Fu Y., Du X., Sergei A.K., Qiu J., Qin W., Li R., Sun J., Liu J., *Stable aqueous dispersion of ZnO quantum dots with strong blue emission via simple solution route*. J. Am. Chem. Soc., **2007**, 129, 16029-16033.
- [17] Munnier E., Cohen-Jonathan S., Linassier C., Douziech-Eyrolles L., Marchais H., Soucè M., Hervè K., Dubois P., Chourpa I., *Novel method of doxorubicin-SPION reversible association for magnetic drug targeting*. Int. J. Pharma, **2008**, 361, 170-176.
- [18] Barick K.C., Aslam M., Prasad P.V., Dravid V.P., Bahadur D., *Nanoscale assembly of amine functionalized colloidal iron oxide*. J. Magn. Magn. Mater., **2009**, 321, 1529-1532.
- [19] Valois C.R.A., Braz J.M., Nunes E.S., Vinolo M.A.R., Lima E.C.D., Curi R., Kuebler W.M., Azevedo R.B., *The effect of DMSA-functionalized magnetic nanoparticles on transendothelial migration of monocytes in the murine lung via a β_2 integrin-dependent pathway*. Biomaterials, **2010**, 31, 366-374.
- [20] Lim J.K., Majetich S.A., Tilton R.D., *Stabilization of superparamagnetic iron oxide core-gold shell nanoparticles in high ionic strength media*. Langmuir, **2009**, 25, 13384-13393.
- [21] Yu F., Yang V.C., *Size-tunable synthesis of stable superparamagnetic iron oxide nanoparticles for potential biomedical applications*. J. Biomed. Mater. Res. A, **2010**, 92, 1468-1475.

- [22] Xie J., Xu C., Kohler N., Hou Y., Sun S., *Controlled PEGylation of monodisperse Fe₃O₄ nanoparticles for reduced non-specific uptake by macrophage cells*. *Adv. Mater.*, **2007**, *19*, 3163-3166.
- [23] Floris A., Ardu A., Musinu A., Piccaluga G., Fadda A.M., Sinico C., Cannas C., *SPION@liposomes hybrid nanoarchitectures with high density SPION association*. *Soft Matter*, **2011**, *7*, 6239-6247.
- [24] Caragheorghopol A., Chechik V., *Mechanistic aspects of ligand exchange in Au nanoparticles*. *Phys. Chem. Phys.*, **2008**, *10*, 5029-5041.
- [25] Nguyen T.K. Thanh, Luke A.W. Green, *Functionalisation of nanoparticles for biomedical applications*. *Nano Today*, **2010**, *5*, 213-230.
- [26] Kassam A., Bremner G., Clark B., Ulibarri G., Lennox R.B., *Place Exchange of Reactions of Alkyl Thiols on Gold Nanoparticles*. *J. Am. Chem. Soc.*, **2006**, *128*, 3476-3477.
- [27] De Palma R., Peeters S., Van Bael M.J., Van den Rul H., Bonroy K., Laureyn W., Mullens J., Borghs G., Maes G., *Silane ligand exchange to make hydrophobic superparamagnetic nanoparticles water-dispersible*. *Chem. Mater.*, **2007**, *19*, 1821-1831.
- [28] Maceria V.S., Liz-Marzan L.M., Farle M., *Water-Based Ferrofluids from Fe_xPt_{1-x} Nanoparticles Synthesized in Organic Media*. *Langmuir*, **2004**, *20*, 6946-6950.
- [29] Frankamp B.L., Fischer N.O., Hong R., Srivasta S., Rotello V.M., *Surface Modification using Cubic Silsesquioxane Ligands. Facile Synthesis of Water-Soluble metal Oxide Nanoparticles*. *Chem. Mat.*, **2006**, *18*, 956-959.
- [30] Lattuada M., Hatton T.A., *Functionalization of monodisperse magnetic NPs*. *Langmuir*, **2007**, *23*, 2158-2168.
- [31] Traina C.A., Schwartz J., *Surface modification of Y₂O₃ nanoparticles*. *Langmuir*, **2007**(18), 9158-9161.
- [32] Bagaria H.G., Ada E.T., Shamsuzzoha M., Nikles D.E., Johnson D.T., *Understanding mercapto ligand exchange on the surface of FePt nanoparticles*. *Langmuir*, **2006**, *22*, 4319-4326.
- [33] Xu Z., Hou Y., Sun S., *Magnetic core/shell Fe₃O₄/Au and Fe₃O₄/Au/Ag nanoparticles with tunable plasmonic properties*. *J. Am. Chem. Soc.*, **2007**, *129*, 8698-8699.

- [34] Zhang Q., Song K., Zhao J., Kong X., Sun Y., Liu X., Zhang Y., Zeng Q., Zhang H., *Hexanedioic acid mediated surface–ligand-exchange process for transferring NaYF₄:Yb/Er (or Yb/Tm) up-converting nanoparticles from hydrophobic to hydrophilic*. Journal of Colloid and Interface Science, **2009**, 336, 171-175.
- [35] Agasti S.S., You C.C., Arumugam P., Rotello V.M., J. Mater. Chem., **2008**, 18, 70-73.
- [36] Tadmor R., Rosensweig R.E., Frey J., Klein J., *Resolving the puzzle of ferrofluid dispersant*. Langmuir, 2000, 16, 9117-9120.
- [37] Porter M.D., Bright D.L., Allara D.L., Chidsey C.E.D., *Spontaneously organized molecular assemblies. 4. Structural characterization of n-alkyl thiol monolayers on gold by optical ellipsometry, infrared spectroscopy, and electrochemistry*. J. Am. Chem. Soc., 1987, 109, 3559-3568.
- [38] Stellaci F., Bauer C.A., Meyer-Friedrichsen T., Wenseleers W., Marder S.R., Perry J.W., *Ultrabright Supramolecular Beacons Based on the Self-Assembly of Two-Photon Chromophores on Metal Nanoparticles*. J. Am. Chem. Soc., **2003**, 125, 328-329.
- [39] Parak W.J., Pellegrino T., Micheel C.M., Gerion D., Williams S.C., *Conformation of oligonucleotides attached to gold nanocrystals probed by gel electrophoresis*. Nano Lett., 2003, 3, 33-36.
- [40] Stouwdam J.W., Shan J., Van Veggel F., Pattantys-Abraham A.G., Young J.F., Raudsepp M., *Photo-stability of Colloidal PbSe and PbSe/PbS Core/shell Nanocrystals in Solution and in the Solid State*. J. Phys. Chem. C, **2007**, 111, 1086-1092.
- [41] Laakson T., Ahonen P., Johans C., Kontturi K., *Stability and Electrostatics of Mercaptoundecanoic Acid-Capped Gold nanoparticles with varying Counterion Size*. Chem. Phys. Chem., **2006**, 7(10), 2143-2149.
- [42] Xu Z., Hou Y., Sun S., *Magnetic core/shell Fe₃O₄/Au and Fe₃O₄/Au/Ag nanoparticles with tunable plasmonic properties*. J. Am. Chem. Soc., **2007**, 129, 8698-8699.
- [43] Stöber W., Fink A., Bohn E.J., *Controlled growth of monodisperse silica spheres in the micron size range*. Coll. Interf. Sci., **1968**, 26, 62-69.

- [44] Xavier Le Guével, Robert Nooney, Colette McDonagh, Brian D. MacCraith, *Synthesis and characterization of monodisperse, mesoporous, and magnetic sub-micron particles doped with a near-infrared fluorescent dye*. Journal of Solid State Chemistry, **2011**, 184, 1545–1550.
- [45] Kim J, Lee JE, Lee J, Yu JH, Kim BC, An K, Hwang Y, Shin CH, Park JG, Kim J, Hyeon T, *Magnetic fluorescent delivery vehicle using uniform mesoporous silica spheres embedded with monodisperse magnetic and semiconductor nanocrystals*. J. Am. Chem. Soc., **2006**, 128, 688-689.
- [46] Lin, Y.-S., Wu, S.-H., Hung, Y., Chou, Y.-H., Chang, C., Lin, M.-L., Tsai, C.-P., Mou, C.-Y., *Multifunctional Composite Nanoparticles: Magnetic, Luminescent, and Mesoporous*. Chem. Mater., **2006**, 18, 5170-5172.
- [47] Kim, J., Kim, H. S., Lee, N., Kim, T., Kim, H., Yu, T., Song, I.C., Moon, W.K., Hyeon, T., *Multifunctional Uniform Nanoparticles Composed of a Magnetite Nanocrystal Core and a Mesoporous Silica Shell for Magnetic Resonance and Fluorescence Imaging and for Drug Delivery*. Angew. Chem., Int. Ed., **2008**, 120, 8566-8569.
- [48] S.H. Wu, Y.S. Lin, Y. Hung, Y.H. Chou, Y.H. Hsu, C. Chang, C.Y. Mou, *Multifunctional Mesoporous Silica Nanoparticles for Intracellular Labeling and Animal Magnetic Resonance Imaging Studies*. Chem. Bio. Chem, **2008**, 9, 53-57.
- [49] S. Iyer, C. D. Woodworth, R. M. Gaikwad, Y. Y. Kievsky, I. Sokolov, *Towards nonspecific detection of malignant cervical cells with fluorescent silica beads*. Small **2009**, 5, 2277-2284.
- [50] Eun-Bum Cho, Dmytro O. Volkov, Igor Sokolov, *Ultrabright Fluorescent Silica Mesoporous Silica Nanoparticles: Control of Particle Size and Dye Loading*. Adv. Funct. Mater. **2011**, 21, 3129–3135.
- [51] S. P. Naik, I. Sokolov, *Ultra-bright fluorescent silica particles: physical entrapment of fluorescent dye rhodamine 640 in nanochannels*. In Nanoparticles: Synthesis, Stabilization, Passivation and Functionalization. ed. R. Nagarajan, ACS, **2008**, 214.
- [52] I. Sokolov, Y. Kievsky, J. M. Kaszpurenko, *Self-Assembly of Ultrabright Fluorescent Silica Particles*. Small, **2007**, 3, 419-423.

- [53] Y.Y. Kievsky, B. Carey, S. Naik, N. Mangan, D. ben-Avraham, I. Sokolov, *Dynamics of molecular diffusion of rhodamine 6G in silica nanochannels*. Journal of Chemical Physics, **2008**, 128, 151102 .
- [54] I. Sokolov, D. O. Volkov, *Ultrabright fluorescent mesoporous silica particles*. J. Mater. Chem., **2010**, 20, 4247-4250.
- [55] Serena A. Corr, Yury P. Rakovich, Yurii K. Gun'ko, *Multifunctional Magnetic-fluorescent Nanocomposites for Biomedical Applications*. Nanoscale Res Lett, **2008**, 3, 87-104.
- [56] C. Sun, J. S. H. Lee, M. Q. Zhang, *Magnetic nanoparticles in MR imaging and drug delivery*. Adv. Drug Deliv. Rev., **2008**, 60, 1252-1265.

Chapter 3

Colloidal Magnetic Nanoparticles prepared by high temperature thermal decomposition of organometallic precursors assisted by surfactants (HTDSA)

In this chapter colloidal nanoparticles of magnetite (Fe_3O_4) and cobalt ferrite (CoFe_2O_4) with narrow particle size distribution are obtained by high-temperature decomposition of organometallic precursors in the presence of oleic acid and oleylamine. Particle size and magnetic properties are tuned by varying reaction conditions or by seed-mediated growth. The as-synthesized nanoparticles have a cubic spinel structure and spherical morphology, as characterized by XRD, TEM, HRTEM. The presence of the capping agents that makes the particles hydrophobic is evidenced by FTIR and TGA analysis. The magnetic properties are size and chemical composition dependent as verified by SQUID measurements.

Colloidal Magnetic Nanoparticles prepared by high temperature thermal decomposition of organometallic precursors assisted by surfactants (HTDSA)

3.0 Experimental

3.1 Introduction

Much progress has been made over the past ten years on the synthesis of monodisperse nanoparticles. Mechanistic studies have shown that monodisperse nanocrystals are produced when burst of nucleation that enables separation of the nucleation and growth processes is combined with the subsequent diffusion-controlled growth process through which the crystal size is determined. Among the several chemical methods proposed to synthesize uniform nanocrystals of metals and metal oxides the thermal decomposition of metal-surfactant complexes seems the most promising.^[1] In this synthesis the decomposition of organometallic precursors in the presence of surfactants leads to the formation of intermediates species that reacts forming small clusters, which successively growth results in nanoparticles. The growing process is mainly controlled by the binding strength of surfactant molecules on the surface of nanoparticles. The relative amounts of the starting reagents including organometallic compounds, surfactants, and solvents are the key parameters for controlling the size and morphology of nanoparticles. The reaction temperature as well as the time may also be crucial for the precise control of size and morphology. The obtaining of colloidal nanoparticles can be described in terms of a sequence of ideal steps of nucleation and growth, then can be distinct in main three phases:

- first phase: the decomposition of organometallic precursor (i.e. metal acetylacetonates, acetates or metallocarbonyls) produces reactive species that forms monomer complexes with surfactant molecules;
- second phase: nucleation process, where the assembling of the monomers form the crystals. In this process, the numbers of generated nucleus per unit of time follows an Arrhenius law;
- third phase: the crystalline particles can growth through the addition of other units of monomer in solution or loose units due to dissolution, depending on supersaturation condition of the solution and on the size of particles (the solubility depends on particle size).

Thermal decomposition, nucleation and growth process of the nanoparticles are schematically shown in *figure 1*.

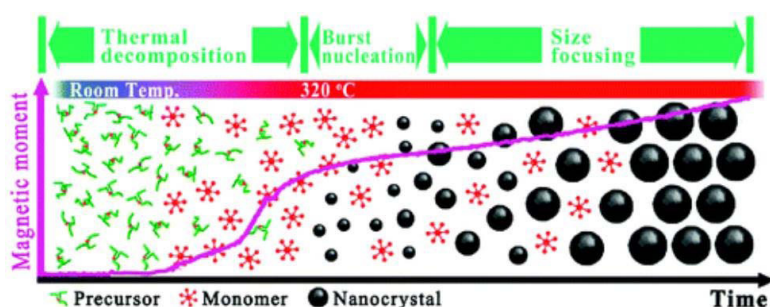


Figure 1. Schematic process of nucleation and growth of the nanoparticles.

3.2 Nucleation and growth mechanism in HTDSA strategy

The classic study by La Mer and Dinegar^[2] has shown that the colloidal synthesis of monodisperse nanocrystals consisting of three components (precursors, organic surfactants and solvents) requires a single, temporally discrete nucleation event, followed by the slower, controlled growth on existing nuclei. The principal advantage of this method is that highly monodisperse nanoparticles are synthesized; the main disadvantage is that the synthesis is carried out in organic, non-polar solvents and the

particles are hydrophobic requiring a further phase transfer to make them hydrophilic. The required growth parameters can be achieved by the rapid addition of reagents (precursors) into a hot coordinating solvent containing surfactants (figure 2).

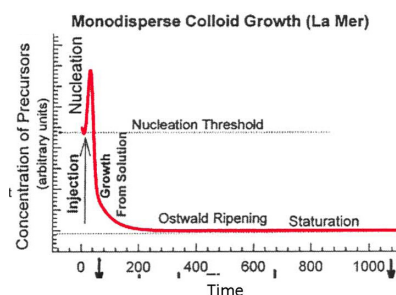


Figure 2. La Mer mechanism for monodisperse colloidal nanoparticles.

The temperature is kept high enough to decompose the reagents, transforming them into active atomic or molecular species (monomers) with concentration above the nucleation threshold. This supersaturation is relieved by a short burst nucleation of nanocrystals. Upon nucleation the concentration of monomers in solution drops below the critical concentration for nucleation; the existing nuclei then grow by the incorporation of additional monomers present in the solution. For crystalline nanocrystals to form in this thermolysis process, the constituent atoms should be able to rearrange, overcome thermal barriers, and anneal during the growth. Hence, the temperature for growth of the nanocrystals must be chosen to be high enough to promote this atomic rearrangement and annealing. However, nanocrystals melt^[3] at substantially lower temperatures (reduction of the melting temperature, by a factor of 1/2, compared to the bulk, is often observed for nanocrystals 2–3 nm in diameter) which is driven by the fact that in the nanoscale the surface energy of the liquid phase is much smaller than the corresponding solid with crystallographic facets, edges or corners. Thus, inorganic colloidal nanocrystals can be grown at substantially lower temperatures where organic molecules such as surfactants are stable. For this synthesis to be effective, appropriate precursors such as organometallic compounds, that rapidly decompose to produce monomers, need to be identified. The best precursors are simple molecules (e.g., metal

carbonyls) with “leaving groups” (e.g., CO) that readily depart leaving behind the desired monomers. Another important parameter influencing crystal growth is the strength with which the surfactant molecules adhere to the surface of the growing crystal.^[4] Surfactants are adsorbed and desorbed rapidly from the surface of nanocrystal allowing the addition of atoms to the crystal already existing. The adhesion should be strong enough to protect the crystals with a monolayer coating, on average, to prevent them from agglomeration but, locally, weak enough to allow the surfactant to exchange on and off the surface of the growing crystal.^[5] The latter ensures that regions of the surface of the crystal are accessible for growth. Examples of such surfactants that “dynamically solvate” the new crystal include alkyl phosphine oxides, alkyl phosphinic acids, fatty acid and amines and some nitrogen containing aromatics. In addition, the surfactants form complexes with the reactive monomer species. The diffusion rate and stability of these complexes in solution, as well as the adhesion of the surfactants to the growing nanocrystal surface are both temperature dependent. Hence, choosing the right temperature is the key to controlling the growth of the nanocrystals. The variation in growth rate as a function of size, in literature has been studied in detail.^[6] For small sizes with very high surface energies, the crystals are unstable due to the large number of surface atoms and lead to negative growth. At large sizes, with small surface/volume ratios, the crystals are stable and grow. The critical size, where the crystals neither grow nor shrink, depends on the concentration of monomers, with high monomer concentrations forming smaller sizes. The peak in growth rate with size is simply an effect of the geometric factor (growth of larger crystals require the incorporation of many more atoms compared to smaller crystals). Moreover, if the monomer concentration is high, smaller crystals will grow more rapidly than larger ones. This leads to a spontaneous narrowing of the size distribution; a process called size-distribution focusing^[7] that has been well demonstrated in experiments.^[8] In general, to obtain monodisperse nanocrystals, it is desirable to temporally separate the nucleation from the growth step and essentially, the nucleation must occur on a short time scale (as in the rapid injection of precursors). Alternatively,^[9] such synthesis can also be accomplished by mixing the reagents at a temperature low enough to preclude any

reaction. Then the chemical reaction is accelerated by the increase in solution temperature at a controlled rate to achieve the required supersaturation, which is followed by the burst nucleation. Adjusting the reaction conditions, which include time, temperature and concentrations of surfactants and precursors, in a systematic way allows good control of the crystal structure^[10] and nanocrystal size in the synthesis. In general, tailoring the ratio of the concentration of precursors to that of the surfactant controls the size since a high surfactant/precursor ratio favors the formation of a larger number of smaller nuclei and thus a smaller nanocrystal size. Alternatively, the particle size can also be controlled either by the binding strength or the steric bulkiness of the surfactant stabilizer. Short chain surfactants (e.g., tributylphosphines) allow faster growth resulting in bigger particles while bulkier ones (e.g., trioctylphosphines) slow the rate of materials being added to the nanocrystals leading to smaller size. Similarly, using a pair of surfactants, one e.g. carboxylic acid, like oleic acid, which binds tightly to the nanocrystal surface and hindering growth and the other, e.g., alkylphosphine or ammine, like TOPO or oleylamine, binding weakly and promoting growth, has also been shown to be an effective way to control size. Many such systems also exhibit a second growth phase called Oswald ripening^[11] where the high surface energy of the small particles promote their dissolution and the materials are re-deposited on the larger nanocrystals. This also increases the size distribution. If the growth rate is further increased beyond this focusing regime, nanocrystals with a variety of anisotropic shapes (such as disks, rods, etc.) are formed.^[12,13] Such kinetic control of shape^[14] can be further facilitated using selective adhesion of surfactants.^[15] The rate of adhesion of surfactants and their dynamic exchange rate in solution are different for different crystallographic faces of a faceted crystal. Organic molecules that preferentially adhere to specific crystallographic planes can be used to modify their relative growth rates when compared to the rest resulting in anisotropic shapes. In summary, the size and morphology of the nanoparticles can be controlled by controlling the reaction times, the residence time at the temperature of decomposition, but also the concentration and ratios of the reactants, nature of the solvent, metal precursors, complexing strength, but also through addition of seeds.^[16] The adsorption of a surfactant onto the surface of the

nanoparticle stabilizes the colloid solution for long time. However, this type of process must be improved to be suitable for industrial preparation, especially in terms of safety of the reactant and the high temperature required.^[17]

3.3 Synthesis of Spinel Ferrite Nanoparticles

In literature, the thermal decomposition at high temperature of iron(III) acetylacetonate, $\text{Fe}(\text{acac})_3$, in the presence of 1,2-hexadecanediol, of oleic acid and oleylamine (as a mixture of surfactants) and phenyl ether or benzyl ether as dispersing solvents, has been reported as an effective method for the synthesis of monodisperse nanoparticles of maghemite ($\gamma\text{-Fe}_2\text{O}_3$) or magnetite (Fe_3O_4), depending on the experimental conditions. The same reaction with the addition of other acetylacetonates as $\text{Co}(\text{acac})_2$ or $\text{Mn}(\text{acac})_2$, leads to the formation of CoFe_2O_4 or MnFe_2O_4 nanoparticles with a narrow particle size distribution.^[1,18]

In this work, magnetite and cobalt ferrite nanoparticles were prepared by HTDSA method, using iron(III) acetylacetonate ($\text{Fe}(\text{acac})_3$, Janssen Chimica, 99%), cobalt(II) acetylacetonate ($\text{Co}(\text{acac})_2$, Janssen Chimica, 99%), 1,2-hexadecanediol (1,2-HD, Aldrich 97%), oleic acid (OA, Aldrich, 90%), oleylamine (OM, Aldrich, <70%), phenyl ether (PE, Aldrich, 99%), and benzyl ether (BE, Aldrich, 99%).

Four cobalt ferrite samples of different sizes from about 5 to 11 nm (CoFe1 , CoFe2 , CoFe3 , CoFe4)^[18,19] were synthesized by thermal decomposition using 1 mmol of $\text{Co}(\text{acac})_2$, 2 mmol of $\text{Fe}(\text{acac})_3$, 10 mmol of 1,2-HD, 6 mmol (CoFe1 , CoFe2 , CoFe3) or 7 mmol (CoFe4) of OA, 6 mmol (CoFe1 , CoFe2 , CoFe3) or 7 mmol (CoFe4) of OM, and 20 mL of phenyl ether (CoFe1) or benzyl ether (CoFe2 , CoFe3 , CoFe4). All the reagents were mixed into a three-neck, round-bottom flask and stirred magnetically at room temperature. Under reflux, the mixtures were heated gradually to 200 °C and kept at this temperature for 30, 60, and 120 min for CoFe1 , CoFe2 , and CoFe3/CoFe4 respectively. The temperature was then increased rapidly up to 265 °C for CoFe1 , and up to 295 °C for CoFe2 , CoFe3 and CoFe4 samples and the mixtures were kept for 30 min,

CoFe1 and CoFe2, and 60 min, CoFe3 and CoFe4 at this temperature. During the process, the initial reddish-orange color of the solutions gradually changed to dark-black, indicating the formation of the oleyl-cobalt ferrite nanoparticles. The black-colored mixture was cooled to room temperature by removing the heat source. Ethanol (40 mL) was then added to destabilize the mixture and the black material was recovered via centrifugation. The black product was then dispersed in hexane, centrifuged to remove any undispersed residue, destabilized with ethanol, centrifuged once more and then redisperse in hexane, giving rise to a ferrofluid that retains its stability for several months. Before SQUID, FTIR and TGA characterization, in order to obtain a powder, the product was recovered once again by adding an excess of ethanol and centrifugation (4500 rpm, 15 min) and drying the wet material at 40 °C overnight. The scheme of the synthesis is shown in figure 3.

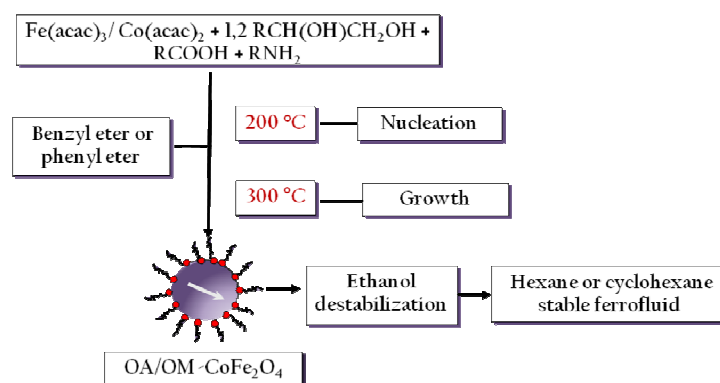


Figure 3. Schematic representation of the synthesis of OA/OM-CoFe₂O₄ samples by HTDSA method.

With a similar procedure in N₂ atmosphere, Fe₃O₄ (MAG) nanoparticles with sizes from 4 to 12 nm have been achieved. Samples of cobalt ferrite and of magnetite were prepared by a one step method, except for the MAG3 sample that was obtained by *seed-mediated growth method* starting from MAG2. In this case, Fe(acac)₃ (2 mmol), 1,2-hexadecanediol (10 mmol), benzyl ether (20 mL), oleic acid (2 mmol), and oleylamine (2 mmol) were mixed and magnetically stirred under a N₂ flow. 84 mg of MAG2 sample dispersed in

hexane (4 mL) was added. The mixture was first heated up to 100 °C for 30 min to remove hexane, then to 200°C for 1 h. Under a blanket of nitrogen, the mixture was further heated to reflux (300°C) for 30 min. The black-colored mixture was cooled to room temperature by removing the heat source, and the same procedure described above was followed in order to recover and wash the product. In *tables 1a* and *1b*, the key parameters.

Table 1a. Key Parameters of the Synthesis Procedure (a) and (b).

Sample	$\langle D_{\text{TEM}} \rangle$ (nm)	Fe(acac) ₃ (mmol)	Co(acac) ₂ (mmol)	1,2-HD (mmol)	OA (mmol)	OM (mmol)	BE mL	PE mL
CoFe1	4.6	2	1	10	6	6	-	20
CoFe2	6.5	2	1	10	6	6	20	
CoFe3	7.8	2	1	10	6	6	20	
CoFe4	11	2	1	10	7	7	20	
MAG1	4.4	2	-	10	6	6	-	20
MAG2	6.6	2	-	10	6	6	20	
MAG3	7.3	2	-	10	2	2	20	
MAG4	12	2	-	10	7	7	20	

Table 1b.

Sample	Solvent	Thermal step 1	Thermal step 2
CoFe1	Phenyl ether	30 min at 200°C	30 min at 265°C
CoFe2	Benzyl ether	60 min at 200°C	30 min at 295°C
CoFe3	Benzyl ether	120 min at 200°C	60 min at 295°C
CoFe4	Benzyl ether	120 min at 200°C	60 min at 295°C
MAG1	Phenyl ether	30 min at 200°C	30 min at 265°C
MAG2	Benzyl ether	120 min at 200°C	60 min at 295°C
MAG3	Benzyl ether	60 min at 200°C	30 min at 295°C
MAG4	Benzyl ether	120 min at 200°C	60 min at 295°C

3.3.1 CoFe₂O₄ nanoparticles: Characterization

The X-ray diffraction patterns (*figure 4*) of all the CoFe₂O₄ samples in the 10-70° 2θ range, indicate the presence of a unique CoFe₂O₄ phase with a cubic spinel structure (PDF Card 22-1086). The broad reflections, indicating the formation of a nanophase, become gradually narrower going from CoFe1 to CoFe4, and as a consequence the

calculated average coherent domain size increases from 5.0 to 8.3 nm (table 2). The calculated cell parameter is 8.39 Å for all the samples, equal, within the experimental error, to the theoretical value (8.391 Å).

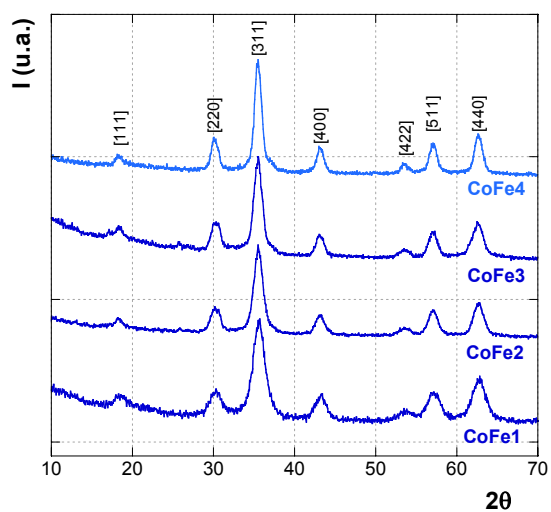


Figure 4. XRD patterns of the CoFe1, CoFe2, CoFe3 and CoFe4 samples.

In all the CoFe_2O_4 samples nanoparticles self-assemble in hexagonal close-packed superlattice, due to the high degree of uniformity in diameter (figure 5(a)).^[19] The presence of surfactants at the nanoparticle surface keeps them isolated from each other by a coating layer of about 2 nm. As an example, in figure 5 some TEM (a) and HRTEM (b,c) images for the samples CoFe3 and CoFe4 have been reported.

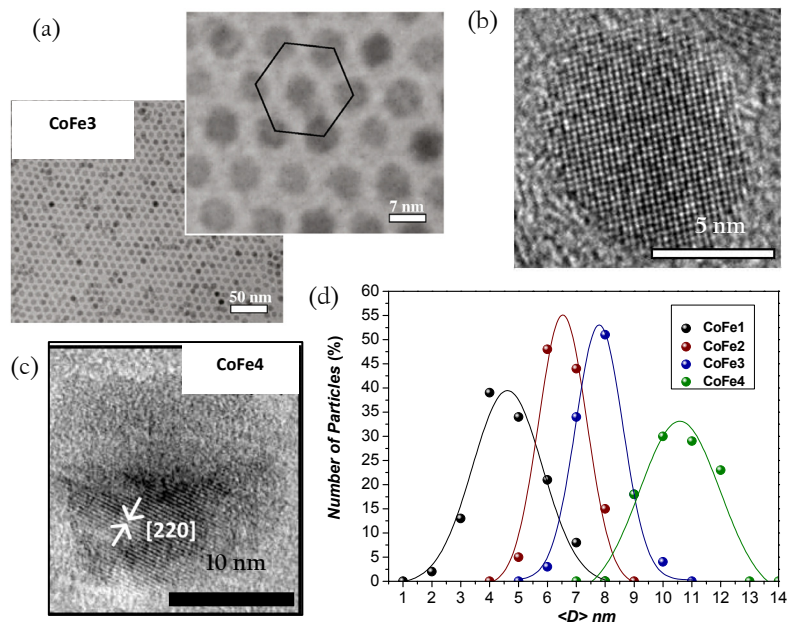


Figure 5. Bright field TEM images of CoFe3 sample at low magnification (a); at high magnification (b) High Resolution TEM of the sample CoFe4(c); particle size distribution of the CoFe samples extracted from TEM images (d).

The high resolution image (*figure 5 (b)*) of the sample CoFe3 shows a well crystallized spheroidal nanoparticle, as indicated clearly by atomic lattice fringes. Similar images have been collected for the CoFe1 and CoFe2 samples. Differently from the other samples, CoFe4 often shows nanoparticles with a rough spheroidal shape and poor crystallinity (*figure 5 (c)*).

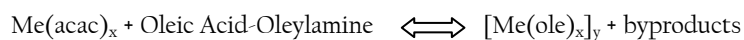
Table 2. Mean Particle Size from XRD and TEM Data.

Sample	$\langle D \rangle_{\text{XRD}}^*$ (nm)	$\langle D \rangle_{\text{TEM}}^\dagger$ (nm)	σ (%)
CoFe1	5.0	4.6	17
CoFe2	6.3	6.5	13
CoFe3	7.6	7.8	10
CoFe4	8.3	11	15

* $\langle D \rangle_{\text{XRD}}$ has been calculated on the [311] reflection using the Sherrer equation and the Warren correction; $\dagger \langle D \rangle_{\text{TEM}}$ has been calculated by particle size distribution on about 200 nanoparticles in different images using an Image software. The standard deviation σ , is calculated from the following equation: $\sigma = \left\{ \frac{\sum [n_i(D_i - \langle D \rangle)^2]}{N} \right\}^{1/2}$

From particle size distributions, obtained by bright field mode micrographs (*figure 5(d)*), a mean particle size of 4.7, 6.5, 7.8 and 11 nm for CoFe1, CoFe2, CoFe3 and CoFe4 samples respectively, have been evaluated (*table 2*). The good agreement between $\langle D \rangle_{\text{XRD}}$ and $\langle D \rangle_{\text{TEM}}$ for the samples CoFe1, CoFe2 and CoFe3 confirms the high degree of crystallinity of the particles. For the sample CoFe4, being the crystallite size (coherent domain) significantly lower than the particle size obtained by TEM, it can be supposed that the high content of surfactants, used during the synthesis, can influence the atomic rearrangement during the growth step inhibiting the crystallization process, as observed by HRTEM image reported in *figure 5(c)*. A decrease of polydispersity is observed increasing particle size (*table 2*) going from CoFe1 to CoFe3, and this trend can be directly correlated with the synthesis parameters. In fact, in order to obtain different particle size, two different strategies can be applied. The first one involves the increase of the permanence time at 200 °C (30 min for CoFe1, 1h for CoFe2 and 2h for CoFe3); the trend of the CoFe series confirms the literature data that indicate as a better mono-dispersion can be obtained increasing the time length of the first thermal step at 200 °C.^[1] The second strategy consists on the increasing of the surfactant amount: CoFe4 sample has been prepared increasing the concentration of the surfactants (oleic acid and oleylamine) from 6 mmol to 7 mmol (see *table 1a*). In literature some authors have reported that the increase of the surfactant concentration induces a decrease on the

nanoparticles size, some others confirm our trend.^[20,21] This result could be justified supposing that during the thermal decomposition of the metallorganic precursor (Me(acac)_x), and the nucleation step (200°C) an intermediate metal complex ([Me(ole)_x]_y) can form and influence the size of the nuclei and the subsequent phase of growth of the nanoparticles, according to the following reaction:



FTIR and Thermal analysis were performed in order to study the presence of the capping agent bound to the nanoparticle surface. As an example, in figure 6 is reported the FTIR spectra of the CoFe4 sample and of the 1:1 mixture of the surfactants (OA-OM).

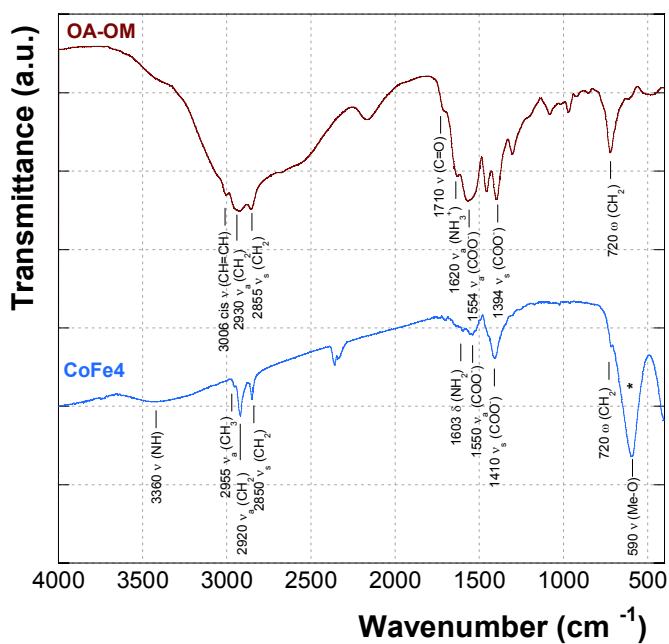


Figure 6. FTIR spectra of the mixture of the surfactants (OA-OM) (a), and CoFe4 sample (b).

The FTIR spectrum of the surfactant mixture reveals modes characteristic of the oleyl group:^[22,23] the peaks at 2855 and 2930 cm^{-1} are due to the symmetric and asymmetric CH_2 stretching modes, and the peak at 3006 cm^{-1} is attributed to a cis $-\text{CH}=\text{CH}-$ arrangement.^[23] The peak at 1710 cm^{-1} , which is typical of the $\nu(\text{C}=\text{O})$ mode of the COOH group is very small. The asymmetric and symmetric stretching at 3370 cm^{-1} and 3294 cm^{-1} , as well as the scissoring modes at 1608 cm^{-1} of the NH_2 group are absent.

The most obvious explanation for the almost complete absence of these peaks is that the mixture of oleic acid and oleylamine consists of an acid-base complex of $-\text{COO}^-$ and $-\text{NH}_3^+$ ions. This is further confirmed by the presence of modes associated with $\nu_a(\text{COO}^-)$ and $\nu_s(\text{COO}^-)$ modes of the carboxylate group observed at 1554 and 1394 cm^{-1} .^[22]

A shoulder is observed at 1620 cm^{-1} , which can be attributed to the antisymmetric deformation of $-\text{NH}_3^+$ group, considering that protonated amines display an antisymmetric deformation in the 1625-1560 cm^{-1} range and a symmetric deformation in the 1550-1505 cm^{-1} range.^[24,25] The modes observed in spectrum in the frequency region below 1500 cm^{-1} arise from complex combinations of the ν C-C stretch, ν C-O stretches, CH_2 deformations and other motions related to NH_3^+ , which are too complex to be assigned. In particular, the spectrum shows an intense peak at 720 cm^{-1} which is typical of the CH_2 rocking modes. Comparison of the FTIR spectra of the mixture OA-OM and CoFe4 sample gives several interesting information. The strong asymmetric $\nu_a(\text{CH}_2)$ and symmetric $\nu_s(\text{CH}_2)$ stretching bands at 2920 and 2850 cm^{-1} are known to be characteristic for the CH_2 chains that are present in oleic acid.^[26] The presence of oleic acid was further confirmed by CH_3 stretching at 2955 cm^{-1} , and two carboxylate stretchings at 1550 and 1410 cm^{-1} . These carboxylate stretchings confirm the observations made by other researchers^[27,28] that oleic acid is chemisorbed onto the nanoparticles' surface via its carboxylate group through a bidentate bond rather than a monodentate bond. The spectrum of CoFe4 nanoparticles also shows modes characteristic of the amine group: a large peak at ~ 3360 cm^{-1} , which can be attributed to the stretching mode $\nu(\text{N-H})$ of the NH_2 group and a peak at 1603 cm^{-1} due to the NH_2 scissoring mode. The presence of these peaks would suggest the presence of oleylamine

even if the formation of $-\text{COO}^- - \text{NH}_3^+$ acid-base complex. The strong band at 590 cm^{-1} is characteristic of the Me-O vibrations related to the ferrite nanoparticles.

The TGA analysis of all the samples give information about the amount of surfactant bound to the nanoparticle surface. In *figure 7* is reported, as an example, the thermogravimetric analysis of CoFe1: beside the slight weight loss up to 200°C , that can be attributed to the sorbed water, a noticeable weight loss between 200°C and about 350°C , due to the total thermal decomposition of the hydrocarbon chain, can be evidenced. The percentage weight loss increases with decreasing size of the nanoparticles (larger surface area/volume ratio) from 28% for CoFe1 to 13% for CoFe4.

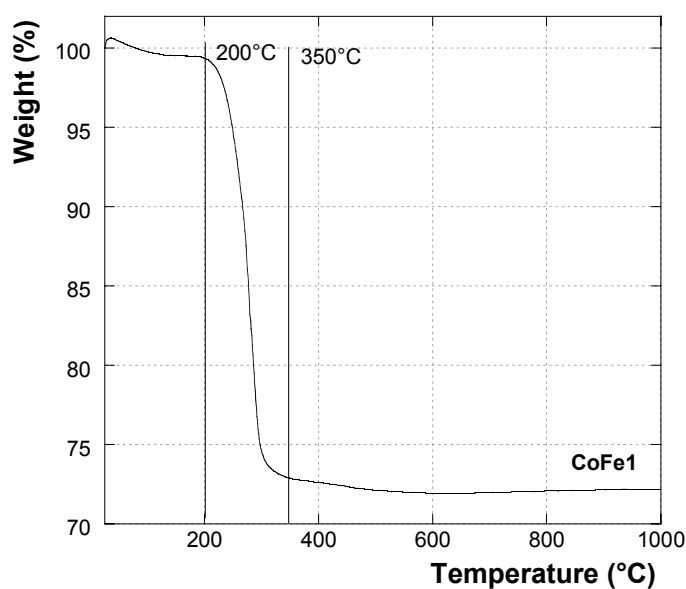


Figure 7. FTIR Thermal analysis for the CoFe1 sample.

Moreover, to verify the actual Fe and Co content, ICP-AES analysis has been performed using multiple standard additions method. In each sample, the ratio Fe to Co has been found higher than the theoretical value of 2. Some differences have been also found between the sample prepared by phenyl ether (CoFe1) and those synthesized by

benzylether (CoFe₂, CoFe₃, CoFe₄): the Fe/Co molar ratio for the CoFe₁ sample is 3.6 while for CoFe₂, CoFe₃ and CoFe₄ is 3. These results can be due to the differences in iron(III) and cobalt(II) acetylacetonates thermal decomposition,^[29] as can be evidenced by the thermal analysis reported in figure 8.

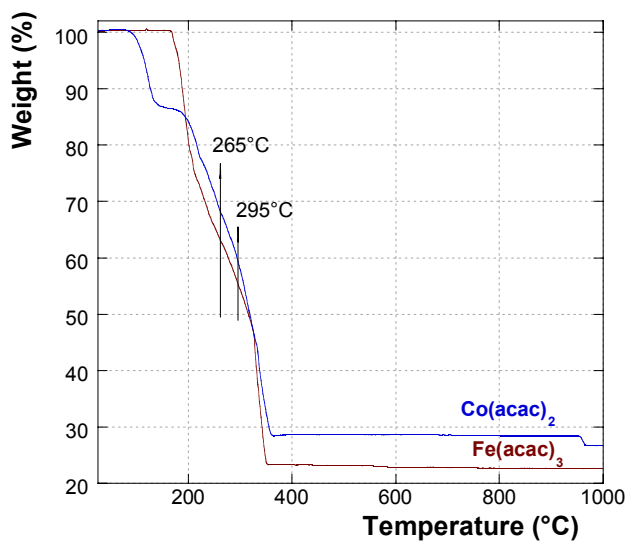


Figure 8. Thermal analysis for the Fe(acac)₃ and Co(acac)₂.

Moreover, an increase of the growing temperature from about 260 °C (diphenyl ether) to about 300 °C (dibenzyl ether) can justify the different Fe/Co values. However, the presence of oleylamine and 1,2-exadecandiol (reducing reagents) can also influence the growth mechanism of the nanoparticles. In fact, under reductive environment, iron(III) ions can be partially reduced to iron(II) ions and therefore may compete with Co(II) ions in the growth process^[30]

Three of the four samples have been submitted to magnetic measurements by SQUID. ZFC-FC curves exhibit a maximum, and the corresponding temperature (T_{max}) is directly proportional to the average blocking temperature.^[31] An irreversible magnetic behavior is observed below a given temperature (T_{irr}) that is related to the blocking of

the biggest particles. An irreversible magnetic behavior is observed below a given temperature (T_{irr}) that is related to the blocking of the biggest particles. The difference between T_{max} and T_{irr} provides a qualitative measure of the magnetic anisotropy distribution, which is strictly connected with the size distribution in the absence of interparticle interactions.^[32] With the increase of particle size, T_{max} (table 3) increases and this can be mainly ascribed to increase of particles volume, even if the influence of interparticle interactions should be taken into account.

Table 3. Table with T_B , T_{max} , T_{irr} values and difference between the two for each of the CoFe1, CoFe2 and CoFe3 samples.

Sample	$\langle D \rangle_{TEM}$ (nm)	σ %	T_{max} (K)	T_{irr} (K)
CoFe1	4.6	17	207(5)	247(5)
CoFe2	6.5	13	224(4)	285(4)
CoFe3	7.8	10	262(5)	283(2)

As expected, T_{irr} follow the same trend of T_{max} (figure 9(a)), indicating superparamagnetic behavior at room temperature for the CoFe1, CoFe2, and CoFe3 samples.

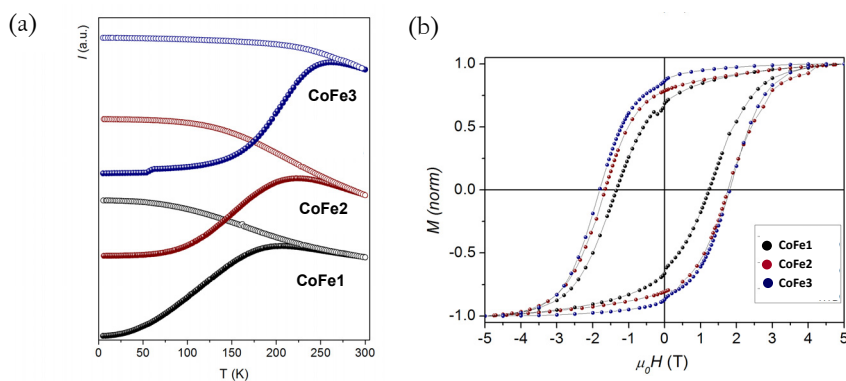


Figure 9. ZFC (full symbols) and FC(empty symbols) magnetizations for CoFe1 (black), CoFe2 (red) and CoFe3 (blue) recorded with an applied field of 2.5 mT (a); Hysteresis loops at 5K of CoFe1 (black), CoFe2 (red) and CoFe3 (blue) (b).

Field dependence of magnetization investigated at 300 K shows completely reversible behavior, (i.e. zero remanence magnetization and zero coercivity) confirming that all the samples are in superparamagnetic state. Conversely at 5 K, being the nanoparticles in the blocked state, all the samples show an hysteretic behavior (*figure 9(b)*). Saturation magnetization (M_s) and coercive field (H_c) are reported in *table 4*.

Table 4. Table with M_s , M_r/M_s and H_c values recorded to 5K, of the CoFe samples.

Sample	$\langle D \rangle_{TEM}$ (nm)	σ %	M_s ($A\ m^2\ Kg^{-1}$)	M_r/M_s	H_c 5K (T)
CoFe1	4.6	17	70(2)	0.7	1.29(3)
CoFe2	6.5	13	68(2)	0.8	1.71(2)
CoFe3	7.8	10	67(2)	0.9	1.81(4)

M_s values are lower than the bulk one ($-90\ Am^2kg^{-1}$)^[33] and they are almost independent from particles size in the investigated range. Coercivity values, from 1.29 T to 1.81 T, increase as the particle size increases, showing an unexpected behavior. In fact, entering the nanoscale, the surface component (K_s) plays the key role in regulating the magnetic anisotropy, and usually H_c increases with the decrease of particle size. However, it is well known that the interactions between molecules and surface atoms of nanoparticles can induce modification on surface anisotropy, leading to a decrease of K_s .^[34] In our sample the presence of the surfactant bound to the particle^[18] reduces surface anisotropy; then the key role is played by the magnetocrystalline component, leading to the observed increase of coercivity with particle size. The high values of M_r/M_s suggest a tendency toward cubic anisotropy with the increase of particle size.^[35]

3.3.2 Fe₃O₄ nanoparticles: Characterization

X-ray diffraction patterns of the magnetite samples (MAG series), shown in *figure 10*, evidence Bragg reflections ascribable to a unique cubic iron oxide phase with an average coherent domain that increases going from MAG1 to MAG4 (*table 5*). Unfortunately XRD data cannot discriminate between magnetite (PDF Card 19-0629) and maghemite

(PDF card 25-1402) structure, therefore, although the black color of the sample should suggest the presence of magnetite, we cannot assert that the sample is made up of pure magnetite. The calculated cell parameter is always between 8.37 Å and 8.38 Å for all samples; this value is lower than the theoretical one for magnetite (8.40 Å) and higher than that for maghemite (8.34 Å), suggesting a partial oxidation of the Fe(II). Preliminary Mossbauer Spectroscopy measurements further confirm that the Fe(II)/Fe(III) molar ratio is never equal to the theoretical value (1/2). It is probable that the contact of the nanoparticles with the air during the time elapsed from their synthesis up to their characterization can induce an oxidation of Fe(II) to Fe(III), at least at the nanoparticle surface.

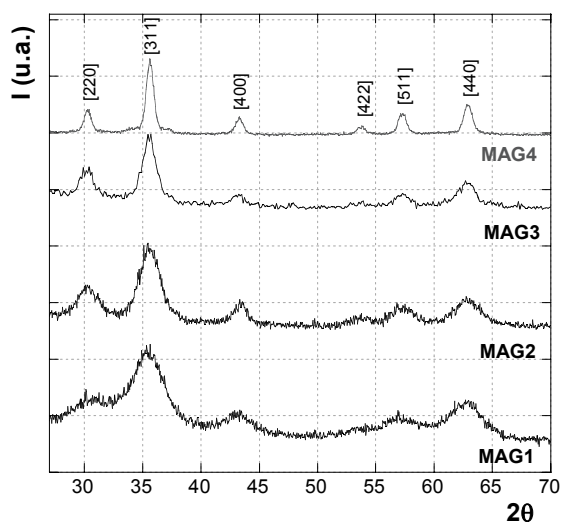


Figure 10. XRD patterns of MAG1, MAG2, MAG3, and MAG4 samples.

Table 5. Table with Mean Particle Size from XRD Pattern, Mean Particle Size from TEM Data

Sample	$\langle D \rangle_{\text{XRD}}^*$ (nm)	$\langle D \rangle_{\text{TEM}}^\dagger$ (nm)	σ (%)
MAG1	3.9	4.4	17
MAG2	4.6	6.5	15
MAG3	7.2	8.0	12
MAG4	11	12	16

$\langle D \rangle_{\text{XRD}}$ has been determined on the [311] reflection using Sherrer equation and the Warren correction; $\langle D \rangle_{\text{TEM}}$ has been calculated via particle size distribution on about 200 nanoparticles in different images using Image software. The standard deviation σ , is calculated from the following equation: $\sigma = \sqrt{\frac{\sum [D_i - \langle D \rangle]^2}{N}}$

TEM analysis of the Fe_3O_4 samples (MAG) confirms the versatility of the HTDSA procedure in tuning nanoparticles size. As in the case of CoFe series the nanoparticles show a spherical morphology, and a self-assemble in hexagonal close-packed superlattice, due to their narrow particle size distribution and to the organic coating layer (figure 11).

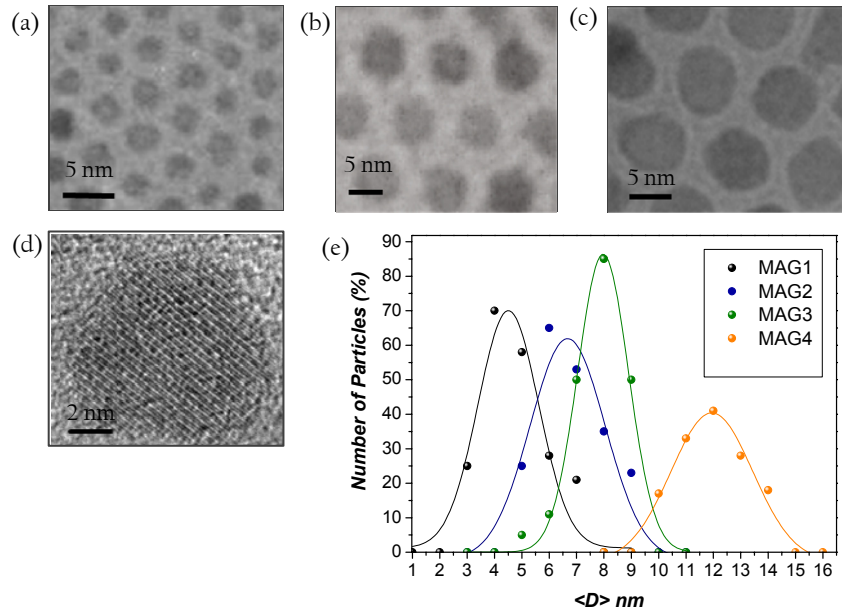


Figure 11. Bright field TEM images for MAG1 (a), MAG2 (b), and MAG3(c) samples; HRTEM image of a single Fe_3O_4 nanoparticle for MAG3 sample (d); Particle size distribution of all MAG samples(e).

The high resolution image (figure 11(d)) shows that Fe_3O_4 nanoparticles, as in the case of CoFe_2O_4 samples, have a spheroidal shape and are single crystallites, as indicated clearly by atomic lattice fringes. Particle size distributions for MAG samples have allowed to evaluate the mean diameter and the polydispersity (table 5). In this case the polydispersity

values are quite similar in all the sample, although as in the case of the CoFe, a slight higher value has been obtained for the sample prepared by using phenyl ether.

The samples of magnetite as the cobalt ferrite series are subjected to TGA and FTIR analysis. It is observed also in this case the presence of the surfactants (oleic acid-oleylamine) bound on the surface of the nanoparticle. The thermal treatment up to 350°C allow to remove completely the surfactants and the weight loss is nanoparticle size dependent (19% for MAG4 and 49% for MAG1). The higher percentage of surfactant present on the magnetite samples, respect to the cobalt ferrite ones, can be due to the different number of the washing cycles.

Among the four samples MAG1, MAG2 and MAG3 have been selected for magnetic characterization. Temperature dependence of magnetization has been investigated by ZFC-FC protocols. The analysis of the ZFC-FC curves (*figure 12(a)*), as expected, shows an increase of T_{max} and of the interparticle interactions by increasing the average size of nanoparticles. Values of the T_{max} , and T_{irr} obtained are reported in *table 6*.

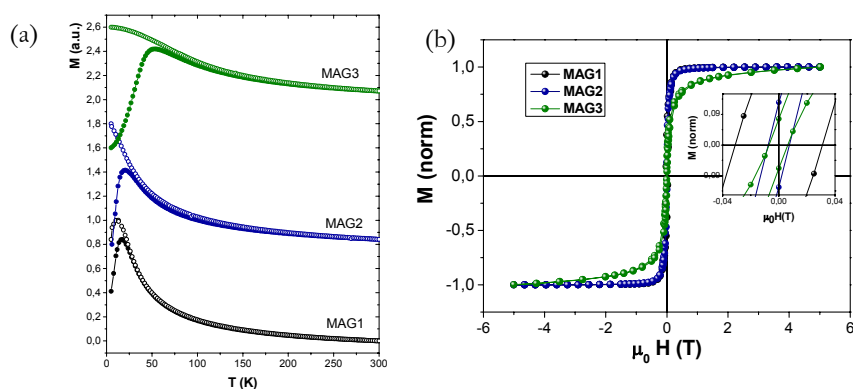


Figure 12. ZFC (full symbols) and FC(empty symbols) magnetizations for MAG1 (black), MAG2 (blue) and MAG3 (green) recorded with an applied field of 2.5 mT (a); Hysteresis loops at 5K of MAG1 (black), MAG2 (blue) and MAG3 (green)(b).

Table 6. Table with T_B , T_{max} , T_{irr} values and difference between the two for each of the samples.

Sample	$\langle D_{TEM} \rangle$ (nm)	σ (%)	T_{max} (K)	T_{irr} (K)	$T_{irr}-T_{max}$ (K)
MAG1	4.4	17	16.9(3)	100(20)	80(20)
MAG2	6.5	15	20.3(8)	200(30)	180(30)
MAG3	8.0	12	53(2)	200(20)	150(30)

Field dependence of magnetization investigated at 300 K shows completely reversible behavior, confirming that all the samples are in superparamagnetic state. Conversely at 5 K, being the nanoparticles in the blocked state, all the samples show an hysteretic behavior (*figure 12(b)*). Saturation magnetization (M_s) and coercive field (H_c) are reported in *table 7*.

Table 7. Table with M_s , M_r/M_s and H_c values of the magnetite samples.

Sample	$\langle D_{TEM} \rangle$ (nm)	σ (%)	M_s ($A\ m^2\ Kg^{-1}$)	M_r/M_s	H_c 5K (mT)
MAG1	4.4	17	48.2(6)	0.068(2)	6.7(1)
MAG2	6.5	15	54.1(2)	0.10(3)	7(3)
MAG3	8.0	12	50.8(1)	0.39(4)	30(6)

M_s values are similar for all the samples but widely lower than that of the corresponding bulk magnetite ($82\ A\ m^2\ Kg^{-1}$) and maghemite ($92\ A\ m^2\ Kg^{-1}$).^[36] In any case these values are comparable to those obtained in the literature for samples with similar size and prepared with similar method.^[33] Some authors reports that the bulk values can be reached just with samples with particles size of at least 150 nm.^[37] Coercivity values are in all cases very small if compared with CoFe samples. In particular, MAG1 and MAG2 show a equal H_c value; this behavior can be caused by the reduced size of these two samples and to the similar average coherent domain (3.9 nm for MAG1 and 4.6 for MAG2). In these cases the surface anisotropy contribution of to the total anisotropy is very high. When the particle size further increases, the component of magnetocrystalline anisotropy prevails over that surface.

In order to study the effect of chemical composition on magnetic properties, magnetite (MAGI) and cobalt ferrite (CoFeI) nanoparticles with similar particle diameter, prepared by HTDSA method, have been selected. Despite similar mean particle size, temperature dependences of magnetization measured by ZFC and FC protocol have completely different features. In particular, the temperature corresponding to the maximum in ZFC curve has a strong increase in cobalt ferrite sample (*table 8*), indicating an increasing of $\Delta E_a \propto KV$.

Table 8. Mean particles from TEM dat ($\langle D \rangle_{\text{TEM}}$); Temperature corresponding to the maximum in ZFC curve (T_{max}), coercive field (H_c) recorded at 5K.

Sample	$\langle D \rangle_{\text{TEM}}$ (nm)	σ (%)	T_{max} (K)	H_c 5K (T)
CoFeI	4.6	17	207(5)	1.29(3)
MAGI	4.4	17	16.9(3)	6.7(1) mT

For spherical particles with similar size, ΔE_a increasing can be only ascribed to a strong increase of anisotropy (K). This picture is confirmed by field dependence of magnetization at 5 K (*figure 13(d)*), showing an hysteretic behavior with coercive field value (i.e. the magnetic field to which corresponds a magnetization equal to 0).

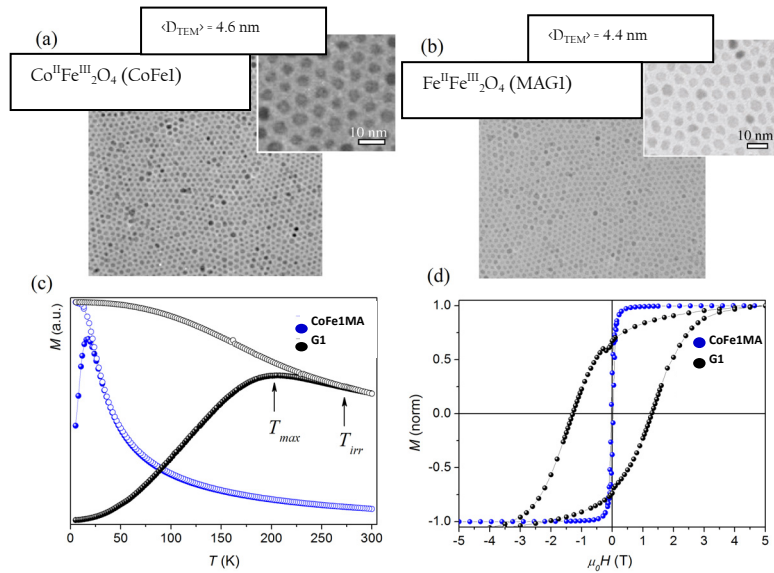


Figure 13. Bright field TEM images of CoFe_2O_4 nanoparticles (CoFeI) (a); Bright field TEM images of Fe_3O_4 nanoparticles (MAGI) (b); ZFC (full symbols) and FC (empty symbols) magnetizations for CoFeI (black); and MAGI (blue) recorded with an applied field of 2.5 mT (c); Hysteresis loops at 5 K for CoFeI (black) and MAGI (blue).

The high coercivity observed in the CoFe_2O_4 sample can be associated to the strong magnetocrystalline contribution of Co^{2+} ions ($3d^7$), which have a non-zero orbital momentum.^[38]

3.4 Conclusions

Exploring, understanding and exploiting the complex behavior in magnetic materials at nanoscale is the key and the challenge not only for fundamental research, but it is crucial for biomedical applications. Spinel ferrites are an ideal magnetic system to understand and govern magnetic properties through size tuning and chemical manipulations due to the strong sensitivity of their properties to the cationic distribution. The selected synthetic strategy has allowed to obtain nanoparticles with tunable size, high

crystallinity and a narrow particle size distribution. Temperature, time and amount of surfactants are the key parameters in order to modify the nucleation and growth kinetics and therefore the size of the particles. The molecular coating, keeping the nanoparticles isolated from each other, ensures the achievement of weak-interacting systems.

References

- [1] S. Sun, H. Zeng, D.B. Robinson, S. Raoux, P.M. Rice, S.X. Wang, G. Li, *Monodisperse MFe_2O_4 ($M = Fe, Co, Mn$) Nanoparticles*. J. Am. Chem. Soc., **2004**, 126, 273-279.
- [2] V.K. LaMer, R.H. Dinegar, *Theory production and mechanism of formation of monodispersed hydrosols*. J. Amer. Chem. Soc., **1950**, 72, 4847-4854.
- [3] P. Buffat, J.P. Borel, *Size effect on the melting temperature of gold particles*. Phys. Rev. A, **1976**, 13, 2287-2298.
- [4] Y.P. Bao, W. An, C.H. Turner, K.M. Krishnan, *The critical role of surfactants in the growth of cobalt nanoparticles*. Langmuir, **2009**, 26, 478-483.
- [5] C.B. Murray, D.J. Norris, M.G. Bawendi, *Synthesis and characterization of nearly monodisperse CdE, E=S, Se, Te. Semiconductor nanocrystallites*. J. Amer. Chem. Soc., **1993**, 115, 8706-8715.
- [6] Y. Yin, A.P. Alivisatos, *Colloidal nanocrystal synthesis and the organic-inorganic interface*. Nature, **2005**, 437, 664-670.
- [7] H. Reiss, *The growth of uniform colloidal dispersions*. J. Chem. Phys., **1951**, 19, 482-487.
- [8] X. Peng, J. Wickham, A.P. Alivisatos, *Kinetics of II-VI and III-V colloidal semiconductor nanocrystal growth: "Focusing" of size distributions*. J. Amer. Chem. Soc., **1998**, 120, 5343-5344.
- [9] C.B. Murray, S. Sun et al., *Colloidal synthesis of nanocrystals and nanocrystal superlattices*. IBM J. Res. Develop., **2001**, 45, 47-56.
- [10] Y. Bao, M. Beerman, A.B. Pakhomov, K.M. Krishnan, *Controlled crystalline structure and surface stability of cobalt nanocrystals*. J. Phys. Chem. B., **2005**, 109, 15, 7220-7222.
- [11] C.B. Murray, C.R. Kagan, M.G. Bawendi, *Synthesis and characterization of monodisperse nanocrystals and close-packed nanocrystal assemblies*. Annu. Rev. Mater. Sci., **2000**, 30, 545-610.
- [12] X. Peng, L. Manna, W. Yang et al., *Shape control of CdSe nanocrystals*. Nature, **2000**, 404, 59-61.
- [13] V.F. Punttes, K.M. Krishnan, A.P. Alivisatos, *Synthesis of colloidal cobalt nanoparticles with controlled size and shapes*. Top Catalysis, **2002**, 19, 145-148.

- [14] A. Puzder, A.J. Williamson, N. Zaitseva, G. Galli, L. Manna, A.P. Alivisatos, *The Effect of Organic Ligand Binding on the Growth of CdSe Nanoparticles Probed by Ab Initio Calculations*. Nano Lett., **2004**, 4, 2361-2365.
- [15] Y. Yin, A.P. Alivisatos, *Colloidal nanocrystal synthesis and the organic-inorganic interface*. Nature, **2005**, 437, 664-670.
- [16] K.M. Krishnan, *Biomedical Nanomagnetism: A Spin Through Possibilities in Imaging Diagnostics, and Therapy*. IEEE Transactions on Magnetics, **2010**, 46, 7, 2523-2558.
- [17] S. Laurent, D. Forge, M. Port, A. Roch, C. Robic, L. Vander Elst, R.N. Muller, *Magnetic Iron Oxide Nanoparticles: Synthesis, Stabilization, Vectorization, Physicochemical Characterization, Biobiological Applications*. Chem. Rev., **2008**, 108, 2064-2110.
- [18] D. Peddis, F. Orrù, A. Ardu, C. Cannas, A. Musinu, G. Piccaluga, *Interparticle Interactions and Magnetic Anisotropy in Cobalt Ferrite Nanoparticles: Influence of Molecular Coating*. Chem. Mater., **2012**, 24, 6, 1062-1071.
- [19] C. Cannas, A. Musinu, A. Ardu, F. Orrù, D. Peddis, M. Casu, R. Sanna, F. Angius, G. Diaz, G. Piccaluga, *CoFe₂O₄ and CoFe₂O₄/SiO₂ Core/Shell Nanoparticles: Magnetic and Spectroscopic Study*. Chem. Mater., **2010**, 22, 3353-3361.
- [20] N. Shukla, C. Liu, P.M. Jones, D. Weller, *FTIR study of surfactant bonding to FePt nanoparticles*. Journal of magnetism and Magnetic Materials, **2003**, 266, 178-184.
- [21] M. Gasgnier, *IR spectra of some potassium carboxylates*. Journal of Materials Science Letters, **2001**, 20, 1259-1262.
- [22] D. Lin-Vien, N.B. Colthup, W.G. Fateley, J.G. Grasselli, *The Hand Book of Infrared and Raman Characteristic Frequencies of Organic Molecules*. Academic Press: Boston, **1991**, 155-178.
- [23] G. Lawrie, I. Keen, B. Drew, A. Chandler-Temple, L. Rintoul, P. Fredericks, L. Grøndahl, *Interactions between alginate and chitosan biopolymers characterized using FTIR and XPS*. Biomacromolecules, **2007**, 8, 2533-2541.
- [24] S.Y. Lee, M.T. Harris, *Surface modification of magnetic nanoparticles capped by oleic acids: characterization and colloidal stability in polar solvents*. J. Colloidal Interface Sci., **2006**, 293, 401-408.

- [25] A.L. Willis, N.J. Turro, S. O'Brien, *Spectroscopic characterization of the surface of iron oxide nanocrystals*. Chem. Mater. **2005**, 17, 5970-5975.
- [26] L. Zhang, R. He, H.C. Gu, *Oleic acid coating on the monodisperse magnetite nanoparticles*. Appl. Surf. Sci., **2006**, 253, 2611-2617.
- [27] J. Von Hoene, R.G. Charles, W.M. Hickam, *Thermal Decomposition of Metal Acetylacetonates: Mass Spectrometer Studies*. J. Phys. Chem., **1958**, 62, 1098-1101.
- [28] J.I. Gittleman, B. Abeles, S. Bozowski, *Superparamagnetism and relaxation effects in granular Ni-SiO₂ and Ni-Al₂O₃ films*. Physical Review B, **1974**, 9, 3891-3897.
- [29] M.F. Hansen, S. Morup, *Estimation of blocking temperatures from ZFC/FC curves*. J. Magn. Magn., **1999**, 203, 214-216.
- [30] Bodker F., Mørup S., Linderøth S., *Surface effects in metallic iron nanoparticles*. Phys. Rev. Lett., **1994**, 72, 282-285.
- [31] N.A. Usov, S.E. Peschany, *Theoretical hysteresis loops for single-domain particles with cubic anisotropy*. J. Magn. Magn. Mater., **1997**, 174, 247-260.
- [32] Cullity B.D., *Introduction to Magnetic Materials*. Series, **1972**.
- [33] Moumen N., Bonville P., Pileni M., *Control of the Size of Cobalt Ferrite Magnetic Fluids: Mössbauer Spectroscopy*. Phys. Chem., **1996**, 100, 14410-14416.

In this chapter oleic acid-oleylamine hydrophobic nanoparticles are converted in hydrophilic systems by ligand exchange and intercalation processes. Hydrophobic nanoparticles obtained by high temperature surfactant assisted approaches show high crystallinity, narrow size distribution and tunable particle size but cannot be use directly for biological purposes, therefore it is necessary to transform them into aqueous dispersible systems. With this aim several molecules like succinic acid, dimercaptosuccinic acid, carboxylic acid-silane and poly[ethylene glycol]-silane, are used to be exchanged with the capping agents of the nanoparticles. Cetyltrimetil ammonium bromide are also employed because can intercalate oleic-acid and oleylamine molecules bound at the nanoparticle surface and makes the nanoparticles hydrophilic.

Transferring of hydrophobic nanoparticles into water:

Ligand exchange and Intercalation processes

4.0 Experimental

4.1 Introduction

The literature has a wealth of evidence showing that long chain carboxylic acids and amines, used as ligands during the synthesis, control the nucleation and growth kinetic, stabilize the nanoparticles and preventing agglomeration. Among the different carboxylic acids the most common are oleic,^[1] lauric,^[2] acids, while the most common ammine are oleylamine, octylamine and trioctylphosphine oxide (TOPO). These ligands being long chain molecules (C>12) with one polar group, are not soluble in water, thus to gain water solubility they has to be substituted with other molecules with further functional groups that allow the transferring to water. Alternately an intercalation process can be employed by using molecules that interact with the apolar carbon chain.

4.2 Ligand Exchange with carboxylic acid and alkylsilane

In the present work ligand exchange is performed on oleic acid/oleylamine capped cobalt ferrite nanoparticles (see chapter 3) by using two different dicarbossilic acid with short chain (C4) and two different alkylsilane:

- Dimercaptosuccinic acid (DMSA);

- Succinic acid (SA);
- *n*-(trimethoxysilylpropyl)ethylene diamine triacetic acid (carboxylic acid-silane, Si_CA);
- 2-[methoxy-(polyethyleneoxy)propyl] trimethoxysilane (poly[ethylene glycol]-silane, Si_PEG)

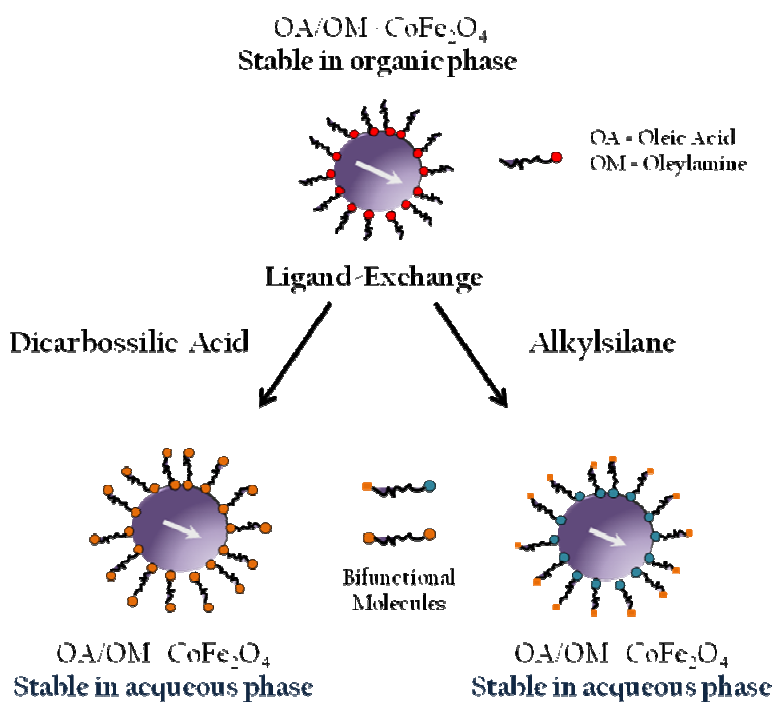


Figure 1. Schematic illustration of the conversion of oleic acid/oleylamine capped-nanoparticles into hydrophilic systems by exchange ligand process.

4.2.1 Ligand Exchange with short chain carboxylic acids

Hydrophobic cobalt ferrite nanoparticles of 11 nm in size (CoFe₄) are transformed into hydrophilic by a ligand exchange reaction using meso-2,3-dimercaptosuccinic acid (DMSA, Aldrich, 98%), or succinic acid (SA, Aldrich, ≥99.4%), dimethyl sulfoxide, DMSO (Fluka AG. Buchs SG, ≥99%), and toluene (Riedel-de Haen, ≥99.7%).

Succinic acid and dimercaptosuccinic acid (DMSA), (*figure 2*) have been chosen for the following reasons:

- they tend to be hydrophilic due to their polarity and ability to form hydrogen bonds;
- they can easily replace the oleic acid bound on the surface of nanoparticles;
- they have free ligand groups for further biomolecule conjugations.

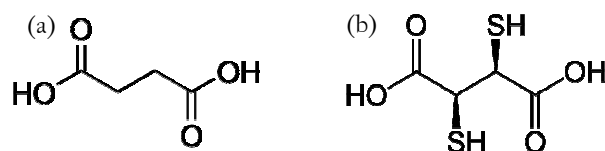


Figure 2. Butanedioic acid (Succinic acid, SA) (a) 2,3-bis(sulfanyl)butanedioic acid (Meso 2,3-dimercaptosuccinic acid, DMSA)(b).

In a typical synthesis, in a glass flask, a magnetic nanoparticles dispersion (5.5 mg of nanoparticles in 3.5 mL of toluene, 6.7 mM), is added to the bifunctional molecule solution in DMSO (12.6 mg of DMSA in 0.7 mL of DMSO or 8.15 mg SA in 0.7 mL, 98.6 mM), sonicated for 5 minutes and mechanically stirred for 24 hours. After 24 hours the complete exchange process can be verified through an evident sedimentation of the black powder on the bottom of the flask and the transparency of the supernatant solution (*figure 3(b)*). To remove free surfactant molecules, the precipitate was recovered

by centrifugation, and washed several times with a 1:1 mixture of acetone and ethanol. The wet powder was then dispersed in 10 mL of water. The colloidal dispersion shows a pH value of about 6 and results to be opalescent dark brown. To favor the deprotonation of the carboxylic groups and the formation of a negative charge at the nanoparticle surface the pH is slightly increased up to 7.5-8 by the adding of NaOH 1M. The dispersion changes color from opalescent-brown to brown-transparent and retain its stability for a long time. (figure 3(d)).

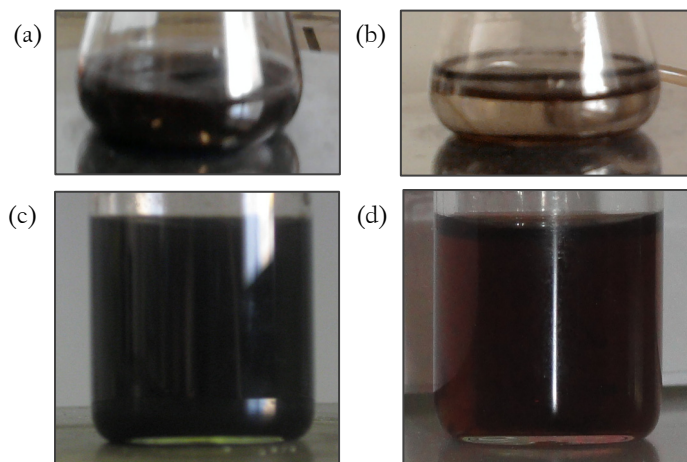


Figure 3. Colloidal dispersion before (a) and after (b) ligand exchange process. Hydrophobic CoFe_2O_4 nanoparticles capped with oleic acid/oleylamine dispersed in cyclohexane (c), hydrophilic CoFe_2O_4 nanoparticles capped with DMSA molecules dispersed in water (CoFe_DMSA).

4.2.2 Characterization

Figure 4 shows TEM images of CoFe₄ sample in Bright Field mode, before and after surface modification via ligand exchange by dimercaptosuccinic acid (CoFe₄_DMSA) or by succinic acid (CoFe₄_SA). Bright field image of CoFe₄ sample (figure 4(a) and (b)) shows nanoparticles of cobalt ferrite of 11 nm in size with nearly spherical morphology. As already observed, the presence of the organic coating allow the self-assembling of the nanoparticles in hexagonal close-packed superlattice. After ligand exchange with DMSA

(figure 4(d), and (e)), as expected, the mean nanoparticles distance among the particles decreases significantly. A similar result is observed in the case of succinic acid-coated nanoparticles (figure 4(g) and (h)), even if an higher degree of aggregation than in the case of DMSA can be evidenced. To verify whether the nanoparticles, once coated with dicarboxylic molecules, have undergone size modifications, due to possible phenomena of dissolution of metal in the presence of carboxylic acid, particle size distributions have been determined after one month from the exchange ligand process (figure 4(c), (f), (i)). The nanoparticle mean size doesn't change, within the limit of the experimental error, after ligand exchange process and an ageing time of one month (table 1).

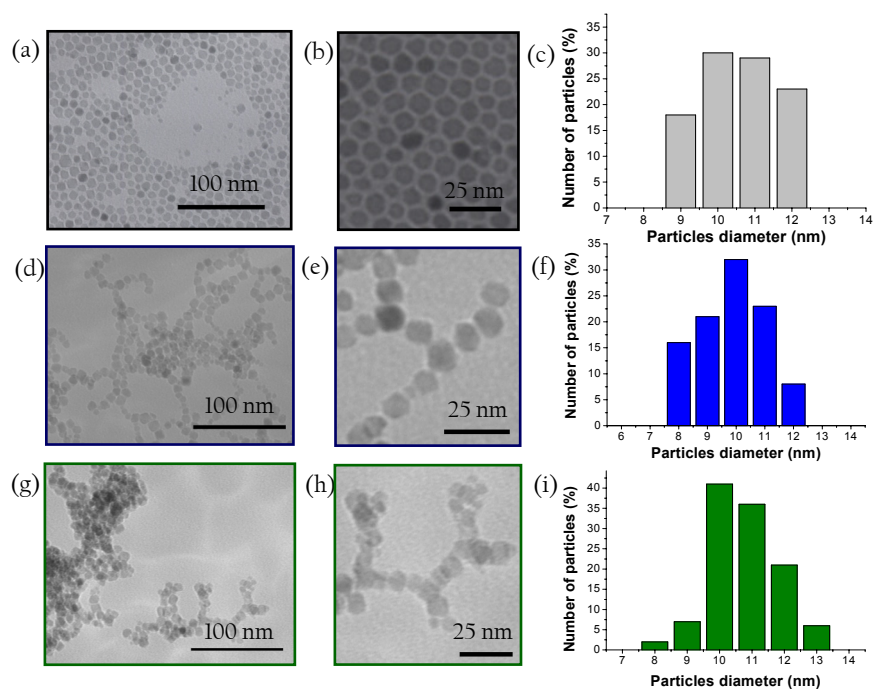


Figure 4. TEM images in Bright Field mode of hydrophobic CoFe_2O_4 nanoparticles and particles size distribution histograms, before (a,b,c), and after ligand exchange with DMSA ($\text{CoFe}_4\text{-DMSA}$ (d,e,f) and SA ($\text{CoFe}_4\text{-SA}$ (g,h,i)).

Table 1. Average size ($\langle D \rangle_{\text{TEM}}$) and polydispersity (σ) of CoFe₂O₄ nanoparticles before and after ligand exchange process by DMSA and SA.

Sample	$\langle D \rangle_{\text{TEM}}$ (nm)	σ (%)
CoFe4	11	15
CoFe4_DMSA	11	14
CoFe4_SA	11	15

To verify the efficiency of the exchange ligand process FTIR spectra on CoFe4 and CoFe4-DMSA (figure 5) or CoFe4-SA (figure 6) samples are performed and compared with the DMSA or SA molecule FTIR spectrum.

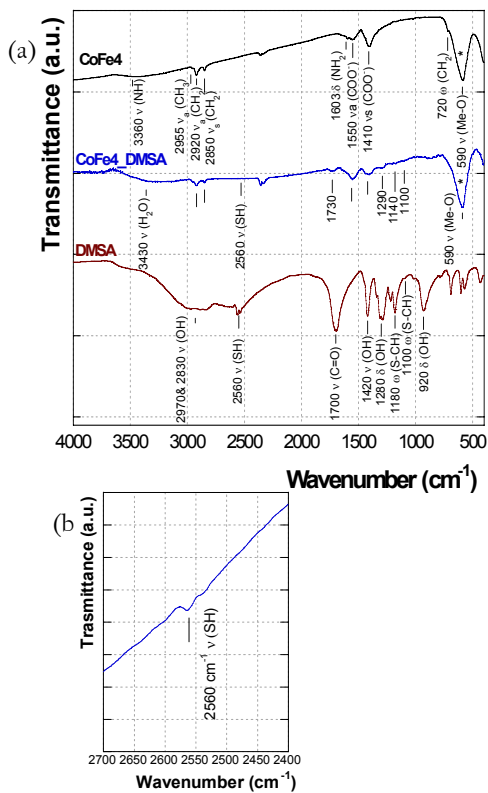


Figure 5. FTIR spectra of CoFe4, CoFe4_DMSA samples and pure DMSA (a), inset detail of peak at 2560 cm⁻¹ of the free SH group (b).

The spectrum of pure DMSA (*figure 5*) reveals a series of adsorptions typical for carboxylic acids that can be schematized as following:

- the bands at 2970, 2830, 1420 cm^{-1} due to the OH stretching modes;
- the adsorptions at 1280, 920 cm^{-1} associated to the OH bending modes;
- the peak at 1200 cm^{-1} attributed to the C-OH stretching mode;
- the peak at 1700 cm^{-1} typical of the $\nu(\text{C}=\text{O})$ mode of the free carbonyl stretching.

Other interesting bands are associated to free thiol groups:

- the peak at 2560 cm^{-1} due to S-H stretching mode;
- the bands at 1140 and 1000 cm^{-1} derived from the S-CH rocking modes.

The spectrum of the oleic acid-oleylamine capped-cobalt ferrite nanoparticles (CoFe4) shows besides the peak at 590 cm^{-1} , ascribed to the Me-O modes in the ferrite nanoparticles, two main peaks at 1550 and 1410 cm^{-1} associated with $\nu_a(\text{COO}^-)$ and $\nu_s(\text{COO}^-)$ of the carboxylate group, suggesting the presence of bidentate carboxylate bonded to the nanoparticle surface.^[3]

The vibrational modes characteristic of the amine group are also present even if they are very weak: a large peak at $\sim 3360 \text{ cm}^{-1}$, which can be attributed to the stretching mode $\nu(\text{N-H})$ of the NH_2 group and a shoulder at about 1600 cm^{-1} due to the NH_2 scissoring mode. The adsorptions at 2920 and 2850 cm^{-1} typical for hydrocarbon chain are due to the symmetric and asymmetric stretching of CH_2 group.^[4]

The comparison of the FTIR spectrum of the sample before and after exchange ligand process gives several interesting information.

Besides the Me-O stretching mode associated to cobalt ferrite phase, a band at 1730 cm^{-1} of the free carbonyl stretching and the small peak associated to free thiol groups at 2560 cm^{-1} (see *figure 5(b)*) indicate the DMSA molecular coating of the nanoparticles. In any case, the presence of some other bands due to the symmetric and asymmetric carboxylate stretching and to the sharp methylene peaks of the oleyl chain suggests that some oleic acid residuals is retained on the surface of CoFe_2O_4 nanoparticles. These data suggest oleic acid and oleylamine have been only partially exchanged with DMSA. Similar results have been obtained for succinic acid-capped nanoparticles (CoFe4_SA)

(figure 6) indicating a partial substitution of the original capping agent with succinic acid.

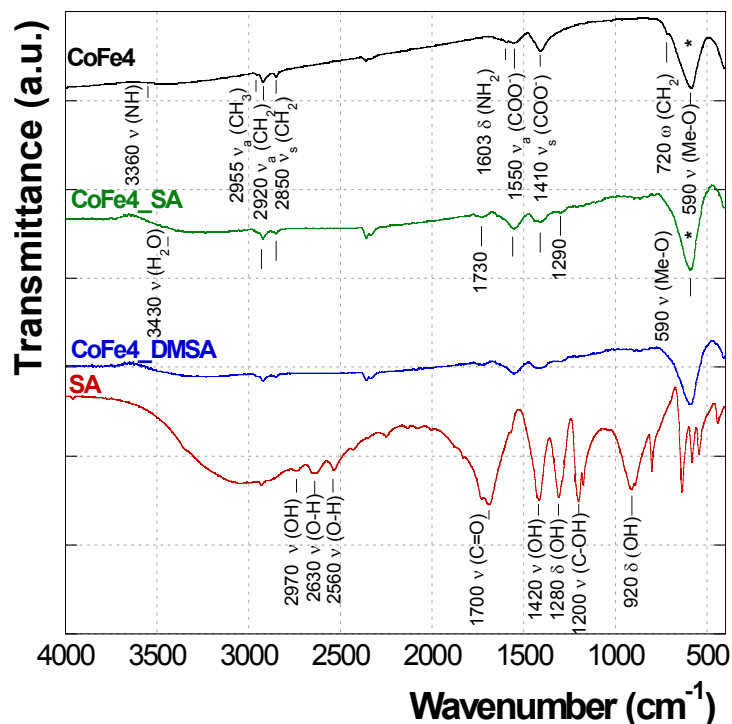


Figure 6. FTIR spectra of the pure Succinic Acid (SA), CoFe4, CoFe4_DMSA and CoFe4_SA samples.

In order to study the stability over time, the colloidal suspensions at pH-7-7.5 has been kept under visual observation. The CoFe4_DMSA dispersion is visibly stable up to 2 month after which start to sediment. On the contrary CoFe4_SA suspension start to sediment just only after a week. It has been taken into account that these observations give information about macroscopic phenomena, therefore to better study the stability over time of the colloidal dispersions from a microscopic point of view it should be necessary to perform further characterizations like the dynamic light scattering in order to measure the hydrodynamic diameter.

The different behavior of the colloidal dispersions CoFe4_DMSA and CoFe4_SA at different pH values can be explained considering the DMSA and SA molecules. These molecules are both small and have a good capacity to complex metallic ions by using one or two of their carboxylic groups.^[5] When nanoparticles are dispersed in water at pH 6-7, both suspensions are unstable because both carboxylic groups can be bonded to the nanoparticles surface. In *figure 7*, as an example, is shown the DMSA molecule in such conformation. No free COOH groups to make the suspensions stable are then present. However, if the nanoparticles are dispersed in alkaline water (7.5-8), a spontaneous process can occur and one of the two carboxylic groups linked to the nanoparticle surface will become free. Under these conditions, the carboxylic groups (COOH) transformed into carboxylates (COO⁻) and will provide enough negative charge to stabilize the colloidal suspension via electrostatic repulsion. These systems with free carboxylate groups as such can be used as MRI contrast agent, in hyperthermia, for magnetic separation and purification and also for conjugating with biological molecules.^[6]

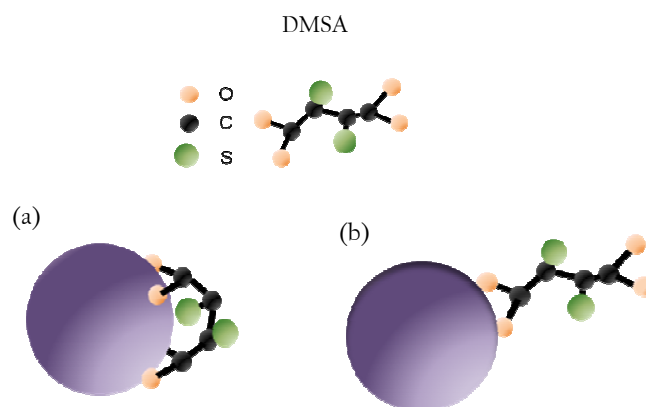
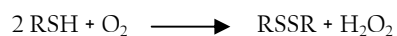


Figure 7. Possible configuration of the DMSA molecules surrounding the magnetic nanoparticles at solution pH of 6-7 (a) and of 7-8 (b).

The observation that at slightly alkaline pH the CoFe4_DMSA dispersion is more stable over time than the CoFe4_SA one can be justified with the further possibility of the

DMSA to form intermolecular disulfide cross-linking between the molecules (figure 8). It is well known in fact, that disulfides can be created by oxidation of the thiol groups in presence of oxygen in aqueous alkaline environment.^[7] The reactions of oxygen with thiol compounds in aqueous solutions are most often described by equations



according to which the reactions gave disulfides and hydrogen peroxide or water.^[8]

However, it is known that oxidation of thiol compounds can afford products containing the S atom in different oxidation states depending on the reaction conditions. In any case, under mild conditions (pH 7-9), thiol compounds are oxidized by oxygen to disulfides,^[9] and only when the pH reach a value of 12, these compounds are transformed predominantly into sulfinic (RSO_2H) and sulfonic (RSO_3H) acids.^[10]

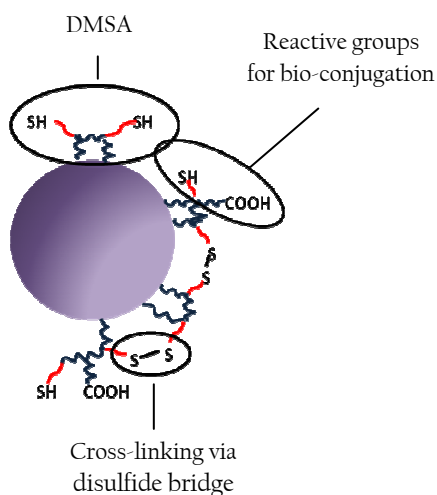


Figure 8. Schematic illustration of meso 2,3- dimercaptosuccinic acid (DMSA)- coated magnetic nanoparticles.

The remaining DMSA free S-H groups can be used to attach target-specific biomolecules, as for instance antibodies for labeling cancer cells or for MRI cancer diagnosis. Using the infrared spectroscopy the band absorption of thiol groups is not evident, which makes difficult the thiol detection.^[6] In contrast, Raman spectroscopy is an excellent tool to detect the thiol group in molecules due to its enhanced Raman scattering. However, detection of thiol groups grafted onto iron oxide nanoparticles using Raman spectroscopy is quite difficult due to the strong absorption of the incident light by the dark cobalt ferrite nanoparticles, leading to very weak Raman scattering from DMSA molecules adsorbed at the nanoparticle's surface. Moreover, by using a visible laser excitation source, the intense emission band of the spinel ferrite nanoparticles hides the thiol characteristic Raman band. To solve this problem, in the literature is proposed the use of both photoacoustic spectroscopy and Raman spectroscopy to monitor thiol groups (S-H) and the associated disulfide bridges (S-S), the latter resulting from the oxidation of the former.^[11]

4.3 Ligand Exchange with alkylsilane

Most ligands reported in literature contain a carboxylate (COO⁻),^[12] a phosphate (PO₃²⁻),^[13] or an alcohol (OH)^[14] endgroup to chemically adsorb to the nanoparticle surface and form a protective coating. It has been noted that the binding of these ligands is noncovalent, which means that they can be more easily desorbed from the surface,^[12] which strongly affects the long-term stability of the nanoparticles. Furthermore, these ligands have only been reported with a limited variety of endgroups, thereby restricting their versatility and applicability. To meet this demand, a more robust and general route for decorating ferrite nanoparticles with diverse functionalities has to be developed. Lately, polymeric grafting is becoming increasingly popular as a way to tune the surface properties of nanoparticles.^[15] However, these methods often rely on several subsequent steps, thereby making the process more complicated and harder to control. Therefore, inspired by the effectiveness and simplicity of silanes self-assembly on metal oxides, they

have been increasingly used to prepare silica-based composites of silane-functionalized nanoparticles.^[16] However, all of these works have mainly focused on the silanization of hydrophilic nanoparticles, made via water-based methods.^[17] Recently alkylsilanes have been proposed also to exchange the hydrophobic ligands on ferrite nanoparticles synthesized via the thermal decomposition method^[18] to render these nanoparticles stable and dispersible in water. Silanes can fulfill high requirements, because they are known to form a densely packed thin film, which is covalently linked to the surface.^[19] At the same time, they exhibit the major advantage that they are commercially available bearing a huge variety of functional endgroups.

From a surface chemistry point of view, ferrites act similarly as metal oxides, presenting a high number of reactive surface hydroxyl groups.^[20] Then ligand exchange is performed by substituting the weak bond with oleic acid/oleylamine with a stronger covalent one between the functional alkylsilanes and the nanoparticles' surface hydroxyl groups (figure 9).

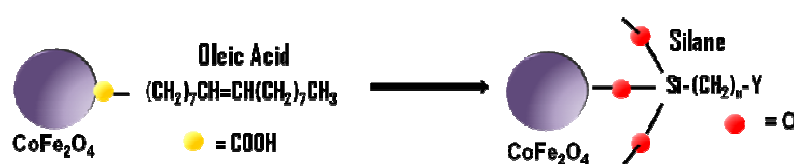


Figure 9. Exchange of oleic acid ligands by silanes on the cobalt ferrite nanoparticle surface.

Silanes are molecules with the general chemical formula $Y-(CH_2)_n-Si-R_3$, where Y represents the headgroup functionality, $(CH_2)_n$ an alkane chain, and $Si-R_3$ the anchor group by which the silane will be grafted to the metal oxide surface (with R being Cl or OR'). Figure 10 gives an overview of silanes containing different endgroups and alkane chain lengths that can be used to perform the ligand exchange.

The characteristics of the deposited silane layer on the particles' surface strongly depend on reaction variables such as the type of solvent, the reaction time, the presence of a catalyst, the type of anchor group, and the silane concentration.

Silanes:

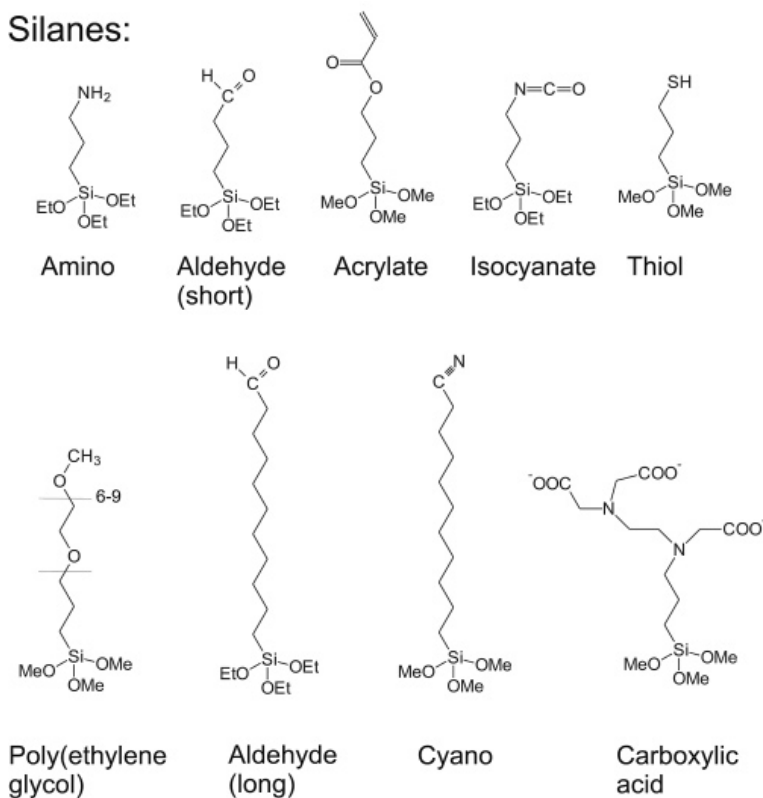


Figure 10. Different silanes bearing a wide variety of endgroups that can be bond on the nanoparticles metal oxide surface.

The ways in which these parameters influence the surface modification process are generally known to be complicated and various.^[19] The situation is even more complicated in the case of nanoparticles in which particle aggregation and interparticle crosslinking can occur.^[16] Moreover, the homogeneity and extent of the silane ligand exchange may be crucial for the final performance of the magnetic nanoparticles. A first important observation regarding the silane ligand exchange procedure concerns the type of anchor groups. If chlorosilanes are applied, the nanoparticles are found to disintegrate

immediately because of the liberation of HCl, which is known to dissolve ferrite materials. Therefore, only (m)ethoxysilanes can be used.

4.3.1 Ligand exchange with alkylsilanes

Hydrophobic ferrite nanoparticles (CoFe₄) have been converted in hydrophilic using also *n*-(trimethoxysilylpropyl)ethylene diamine triacetic acid trisodium salt (Si-CA, ABCR GmbH & Co.KG, 45% in water) or 2-[methoxy-(polyethyleneoxy)propyl] trimethoxysilane (Si-PEG, ABCR GmbH & Co.KG, 90%) and acetic acid (Aldrich, ≥99.7%).

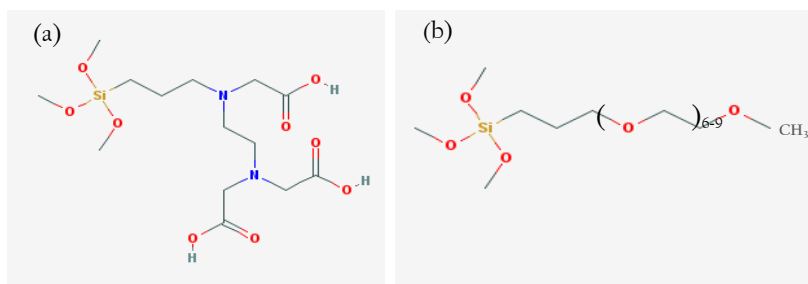


Figure 11. Carboxylic acid-silane, Si-CA (a), and poly[ethylene glycol]-silane, Si-PEG (b) molecular formula.

Acetic acid is added to catalyze the reaction and as a reagent for the hydrolysis and condensation of the alkoxy silane groups. The rate of condensation is determined by the anchor group and by the solvent used.^[21] In the case in which a nonpolar solvent (hexane or cyclohexane) and an alkoxy silane are used, the condensation rates are known to be rather slow.^[16] Therefore, the reaction is performed for long time (e.g., 72 hours) to ensure full exchange of the hydrophobic ligands and to promote a higher density of functional groups on the nanoparticles' surface.^[18]

In a glass container under ambient conditions, 0.5 % (v/v) carboxylic acid-silane (Si-CA) or poly[ethylene glycol]-silane (Si-PEG) solution was added to 5 mL of a dispersion of

hydrophobic CoFe_2O_4 nanoparticles in cyclohexane (2.6 mg cobalt ferrite/mL cyclohexane), containing 0.01% (v/v) acetic acid. The mixture was mechanically stirred for 96 hours, in order to ensure the complete exchange between the hydrophobic surfactants and silane molecules, during which the particles tend to settle on the bottom of the flask (*figure 12*).

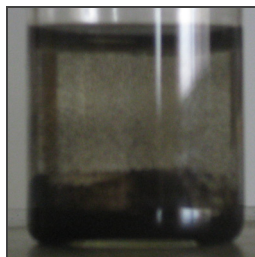


Figure 12. Colloidal dispersion after the ligand exchange with carboxylic acid-silane.

The black-brown powder was separated using a magnet and washed several times by centrifugation with cyclohexane to remove all silane excess. The product was finally redispersed in 10 mL water.

4.3.2 Characterization

Figure 13 shows TEM images of cobalt ferrite nanoparticles in Bright Field mode, before (CoFe_4) and after surface modification via ligand exchange by carboxylic acid-silane ($\text{CoFe}_4\text{ Si-CA}$) or by poly[ethylene glycol]-silane ($\text{CoFe}_4\text{ Si-PEG}$).

The hydrophobic nanoparticles modified with carboxylic acid-silane (*figure 13*(d), (e)) and with poly[ethylene glycol]-silane (*figure 13*(g), (h)) show a slightly higher degree of aggregation if compared with CoFe_4 sample. Silane monolayer around the nanoparticles cannot be easily evidenced by TEM analysis due to both the thin thickness and the low contrast.

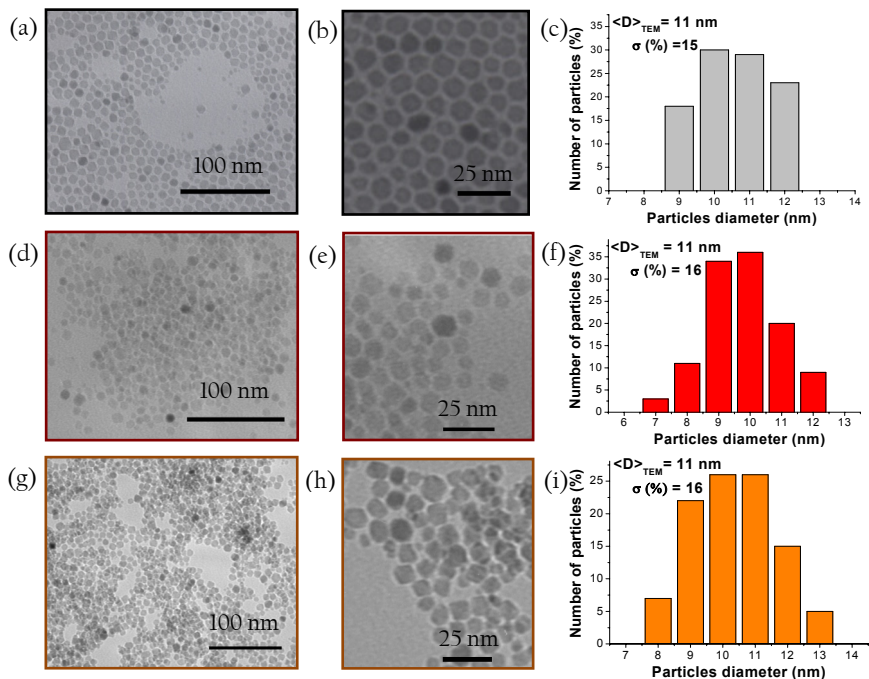


Figure 13. TEM images in Bright Field mode of hydrophobic CoFe_2O_4 nanoparticles and particles size distribution histograms, before (a,b,c), and after ligand exchange with Si-CA ($\text{CoFe}_4\text{-Si-CA}$) (d,e,f) and Si-PEG ($\text{CoFe}_4\text{-Si-PEG}$) (g,h,i).

Therefore, particle size distributions don't show any significant change, within the limit of the experimental error, after exchange ligand process (figure 13 (c), (f), (i)) suggesting that a thin homogeneous layer of alkylsilane covers the nanoparticles.

To verify the successful silane ligand exchange the FTIR spectroscopy has been used once again. FTIR spectra (figure 14) show CoFe_2O_4 nanoparticles before (CoFe_4) and after ligand exchange process with carboxylic acid-silane ($\text{CoFe}_4\text{-Si-CA}$) and poly[ethylene glycol]-silane ($\text{CoFe}_4\text{-Si-PEG}$).

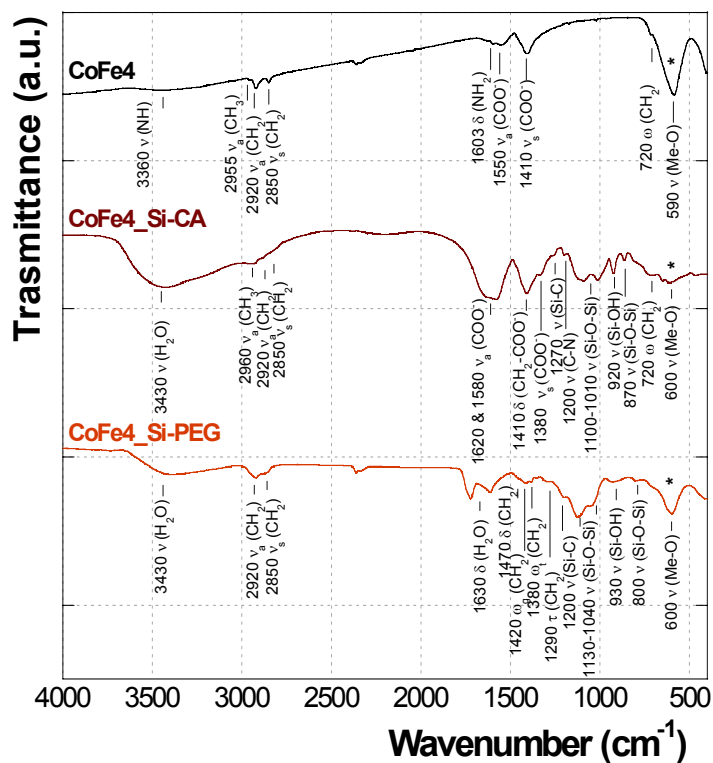


Figure 14. FTIR spectra of the CoFe₄, CoFe₄_Si-CA and CoFe₄_Si-PEG samples.

The most clear evidence of the exchange is that the strong band 590 cm⁻¹, characteristic of the Me-O vibrations related to the ferrite nanoparticle, after ligand exchange, undergoes a broadening and a shift at 600 cm⁻¹; this behavior can be due to the formation of Me-O-Si bonds.^[22] Furthermore, compared to the as synthesized oleic acid/oleylamine stabilized nanoparticles, several new bands are observed between 1000 and 1150 cm⁻¹. These bands are characteristic of silane layers and are originated from Si-O-Si vibrations.^[23] The alkane chain present in both silanes, as well as in the oleyl chain, results in the appearance of typical bands at 2920 and 2850 cm⁻¹, attributed to asymmetric and symmetric CH₂ stretchings respectively. The position and width of

these CH₂ bands is known to give more information about the crystalline packing of the alkane chains in the silane layer.^[24] The observed values (2920-2850 cm⁻¹) and the broadening of the bands implicate that the silane layers deposited on the ferrite nanoparticles do not exhibit an ordered packing. This low degree of order could be attributed to partial condensation between the Si-OH or Si-OR caused by the high radius of curvature of the nanoparticles or to the partial presence of the starting capping agent. Notable, is the appearance of a small band at 2960 cm⁻¹ in the case of carboxylic acid-silane (CoFe₄-Si-CA). This band is ascribed to the symmetric CH₃ stretching of the alkoxy anchor group and gives proof of an incomplete hydrolysis of the silane molecules during ligand exchange. The complete disappearance of the carboxylate stretchings at 1550 and 1410 cm⁻¹ associated at the oleic acid, after ligand exchange with the carboxylic acid-silane (CoFe₄-Si-CA), unfortunately cannot be observed, as they are overshadowed by the broadening of the asymmetric (1620-1580 cm⁻¹), symmetric (1380 cm⁻¹) COO⁻ stretchings, and of the band at 1410 cm⁻¹ of the bending CH₂-COO⁻ group, related to the three carboxylate groups of the carboxylic acid-silane.

The presence of Si-PEG at the surface cobalt ferrite nanoparticles (CoFe₄-Si-PEG) is confirmed by its characteristic ethylene glycol vibrations. The broadening of the bands in the 2800-3000 cm⁻¹ region is the result of strong overlapping of the CH₂ stretchings (asymmetric and symmetric) in the PEG-tail and in the alkane chain. The symmetric CH₂ stretching is found at 2920 and 2850 cm⁻¹, respectively. The bands at 1470, 1420, 1380, 1290, 1200 cm⁻¹ correspond well with the CH₂-O-CH₂ scissoring, wagging (*gauche*), wagging (*trans*), twisting, and stretching, modes, respectively. PEG is known to exhibit different conformations such as amorphous, helical crystalline, and all-trans crystalline, dependent on its chain length and density.^[25] On the basis of the literature data, we can suppose that the PEG-silane coating on the nanoparticles is mainly present as amorphous state.^[26] The stability of the aqueous dispersions of CoFe₄-Si-CA and CoFe₄-Si-PEG have been studied up to three months. As can be seen from the images shown in *figure 15*, the colloidal suspensions in water of CoFe₄-Si-CA (*figure 15(a)*) and CoFe₄-Si-PEG (*figure 15(b)*), are stable up to 2 month.

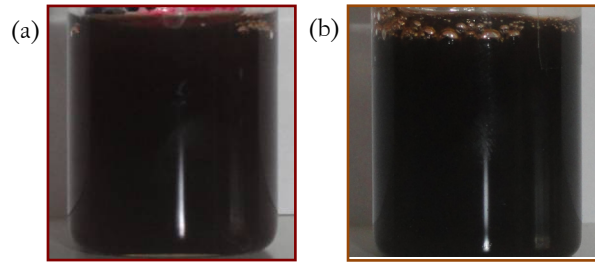


Figure 15. Stability in water of CoFe_Si-CA (a), and CoFe_Si-PEG (b) samples.

4.4 Intercalation process with CTAB (MAG_CTAB)

Cetyltrimethylammonium bromide (CTAB) is a cation surfactant containing a quaternary ammonium group (their hydrophilic head), and a hydrocarbon chain (their hydrophobic tails). When dispersed in water it forms spherical micelles above the critical micellar concentration (CMC of 0.87 mM at 25°C) in which the hydrophilic head group forms the outer surface and the hydrophobic tails point towards the centre.^[28] (figure 16).

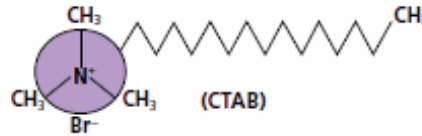


Figure 16. Cationic surfactant cetyltrimethylammonium bromide (CTAB); CMC= 0.87 mM at 25°C.

By the use of this cationic surfactant hydrophobic magnetite nanoparticles of 6 nm in size (sample MAG2, see chapter 3) are transformed into hydrophilic by an intercalation process (figure 17).

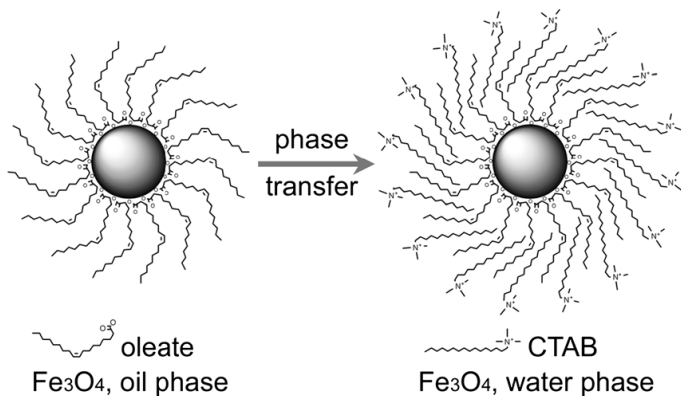


Figure 17. Intercalation process of hydrophobic Fe_3O_4 nanoparticles with CTAB.

The sample MAG2 has been converted in hydrophilic dispersing 4.9 mL of ferrofluid (1.1 mg $\text{Fe}_3\text{O}_4/\text{mL}$ in chloroform), (*figure 18(a)*) in a aqueous solution containing 0.2 g of CTAB in 10 mL of water (0.55 mmol). A vigorous stirring for 1 hour followed by the heating at 60 °C for 30 minutes generate a stable and clear aqueous dispersion of magnetic nanoparticles (*figure 18(b)*). In the first step, when the hydrophobic capped magnetic nanoparticles stable in organic solvent (chloroform) are added into a CTAB aqueous solution, the CTAB molecules intercalate the capping agent stabilizing the magnetic oil droplets leading to the formation of an oil-in-water microemulsion.^[27] Subsequent evaporation of the volatile organic solvent by mild heating drives CTAB molecules to directly interact with the magnetic nanoparticles surface ligands through hydrophobic interactions. The alkyl chains of the CTAB and the magnetic nanoparticles surface ligands intercalate into each other, rendering the CTAB cationic headgroup (quaternary amine) facing outward and the magnetic nanoparticles-CTAB complex water-soluble.^[28,29]

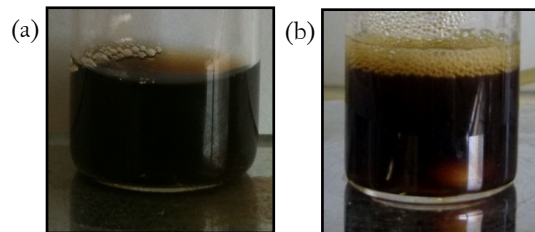


Figure 18. Hydrophobic Fe_3O_4 nanoparticles capped with oleic acid/oleylamine (MAG2) (a), and hydrophilic Fe_3O_4 nanoparticles after intercalation by CTAB molecules (MAG_CTAB) (b).

4.4.1 Characterization

TEM images in Bright Field mode (*figure 19(a)*), before and after the intercalation, show that no evident modification occur, being the mean interparticle distance similar.

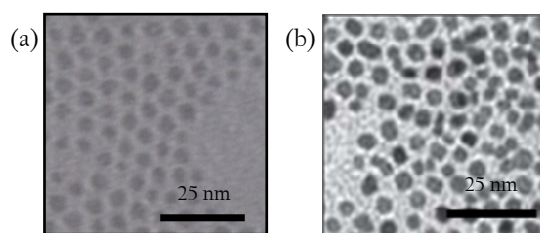


Figure 19. TEM images of Fe_3O_4 sample in Bright Field mode, before (a) and after phase transfer using CTAB (b).

When the hydrocarbon tails of CTAB interpose between the hydrocarbon tails of oleic acid /oleylamine, no evident modification occur. (*figure 19(b)*) TEM bright field images show that the morphology as well as the mean interparticle distance is retained after intercalation, probably because the CTAB (C16) has a similar length hydrocarbon chain (C16) to the oleic acid/oleylamine.

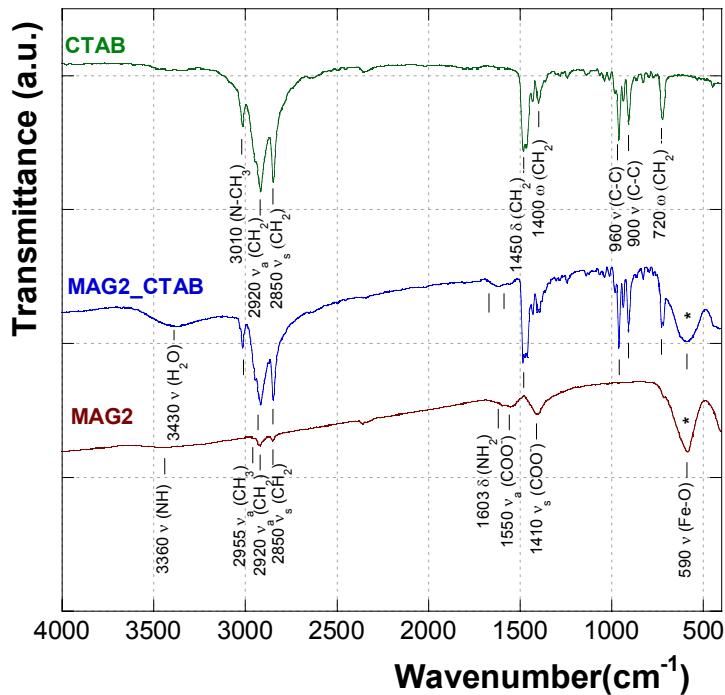


Figure 20. FTIR spectra of CTAB, MAG2 and MAG₂_CTAB samples.

The FTIR spectrum of MAG₂_CTAB sample, after intercalation process, (figure 20) exhibits, beside the main peak of Fe-O mode centered at 590 cm⁻¹, a series of absorptions attributable to the presence of CTAB:

- the bands at 2920, 2850 cm⁻¹ and 1450 cm⁻¹, are identified as symmetric, asymmetric stretching, and bending CH₂ modes;
- the peak at 3010 cm⁻¹ is due to the N-CH₃ mode;
- at 960, 900 cm⁻¹ are centered the adsorption of C-C stretching modes.

The presence of oleic acid molecules bonded to the nanoparticle surface is confirmed by the peak at 1550 cm⁻¹, associated with ν_a(COO⁻) of the carboxylate group.^[3]

The MAG₂_CTAB sample is stable over time for months. The system as such, could be used in the biomedical field.

4.5 Conclusions

In order to successfully prepare and biofunctionalise nanoparticles for a given biomedical application, a wide range of physical, chemical, biological and physiological factors and conditions must be taken into account. Surface modification of hydrophobic nanoparticles can be carried out by different approaches, among which we selected exchange ligand and intercalation processes. The exchange ligand process is one of the most versatile ways to convert an hydrophobic nanoparticle into an hydrophilic system, to add new functionalities and tune the minimum distance between the particles and therefore the magnetic inter-particles interaction. The intercalation process can be also used to convert hydrophobic nanoparticles into hydrophilic system. All these systems, are stable in water and can be employed in MRI and hyperthermia applications.

References

- [1] Jain Tapan K., Morales M.A., Sahoo Sanjeeb K., Leslie-Pelecky Diandra L., Labhasetwar V., *Iron oxide nanoparticles for sustained delivery of anticancer agents*. *Molecular pharmaceuticals*, **2005**, 2(3), 194-205.
- [2] Decuyper M., Joniau M., *Mechanistic Aspects of the Adsorption of Phospholipids onto Lauric Acid Stabilized Fe₃O₄ Nanocolloids*. *Langmuir*, **1991**, 7(4), 647-652.
- [3] N. Shukla, C. Liu, P.M. Jones, D. Weller, *FTIR study of surfactant bonding to FePt nanoparticles*. *Journal of Magnetism and Magnetic Materials*, **2003**, 206, 178-184.
- [4] C. Cannas, A. Musinu, A. Ardu, F. Orrù, D. Peddis, M. Casu, R. Sanna, F. Angius, G. Diaz, G. Piccaluga, *CoFe₂O₄ and CoFe₂O₄/SiO₂ Core/Shell Nanoparticles: Magnetic and Spectroscopic Study*. *Chem. Mater.*, **2010**, 22, 3353-3361.
- [5] Fauconnier, N., Pons J. N., Roger J., Bee A., *Thiolation of maghemite nanoparticles by dimercaptosuccinic acid*. *J. Colloid Interface Sci.*, **1997**, 194, 427-43.
- [6] Chen Z.P., Zhang Y., Zhang S., Xia J.G., Liu J.W., Xu K., Gu N., *Preparation and characterization of water-soluble monodisperse magnetic iron oxide nanoparticles via surface double-exchange with DMSA*. *Colloids and Surfaces A: Physicochem. Eng. Aspects*, **2008**, 316, 210-216.
- [7] G.A. Bagiyani, I.K. Koroleva, N.V. Soroleva, A.V. Ufimtsev, *Oxidation of thiol compounds by molecular oxygen in aqueous solutions*. *Russian Chemical Bulletin, International Edition*, **2003**, 52, 5, 1135-1141.
- [8] D. Cavalli, C. De marko, S. Dupre, *Luminol chemiluminescence studies of the oxidation of cysteine and other thiols to disulfides*. *Arch. Biochem. Biophys.*, **1968**, 124, 18-26.
- [9] L. Pecci, G. Montefoschi, G. Musci, D. Cavallini, *Novel findings on the copper catalysed oxidation of cysteine*. *Amino Acids*, **1997**, 13, 355-367.
- [10] T.J. Wallace, A. Schriesheim, *The base-catalysed oxidation of aliphatic and aromatic thiols and disulphides to sulphonic acids*. *Tetrahedron*, **1965**, 21, 2271-2280.

- [11] M.A.G. Soler, E.C.D. Lima, E.S. Nunes, F.L.R. Silva, A.C. Oliveira, R.B. Azedo, P.C. Morais, *Spectroscopic Study of Maghemite Nanoparticles Surface-Grafted with DMSA*. J. Phys. Chem. A, **2011**, 115, 1003-1008.
- [12] White M.A., Johnson J.A., Koberstein J.T., Turro N.J., *Toward the Syntheses of Universal Ligands for Metal Oxide Surfaces: Controlling Surface Functionality through Click Chemistry*. J. Am. Chem. Soc., **2006**, 128(35), 11356-11357.
- [13] Grancharov S.G., Zeng H., Sun S., Wang S.X., O'Brien S., Murray C.B., Kirtley J.R., Held G.A., *Bio-functionalization of monodisperse magnetic nanoparticles and their use as biomolecular labels in a magnetic tunnel junction based sensor*. J. Phys. Chem. B, **2005**, 109, 1330-13035.
- [14] Hong R., Fischer N.O., Emrick T., Rotello V.M., *Surface PEGylation and Ligand Exchange Chemistry of FePt nanoparticles for Biological Applications*. Chem. Mater., **2005**, 17, 4617-4621.
- [15] Lattuda M., Hatton T.A., *Functionalization of monodisperse magnetic nanoparticles*. Langmuir, **2007**, 23, 2158-2168.
- [16] Bruce I.J., Sen T., *Surface modification of magnetic nanoparticles with alkoxysilanes and their application in magnetic bioseparations*. Langmuir, **2005**, 21, 7029-7035.
- [17] Koh I., Wang X., Varunghese B., Isaacs L., Ehrman S.H., English D.S., *Magnetic iron oxide nanoparticles for biorecognition: evaluation of surface coverage and activity*. J. Phys. Chem. B, **2006**, 110, 1553-1558.
- [18] De Palma R., Peeters S., Van Bael M.J., Van den Rul H., Bonroy K., Laureyn W., Mullens J., Borghs G., Maes G., *Silane ligand exchange to make hydrophobic superparamagnetic nanoparticles water-dispersible*. Chem. Mater., **2007**, 19, 1821-1831.
- [19] Onclin S., Ravoo B.J., Reinhoudt D.N., *Engineering silicon oxide surfaces using self-assembled monolayers*. Angew. Chem. Int. Ed. Engl., **2005**, 44, 6282-6304.
- [20] McCafferty E., Wightman J.P., *Determination of the concentration of surface hydroxyl groups on metal oxide films by a quantitative XPS method*. Surf. Interface Anal., **1998**, 26, 549-564.

- [21] Fadeev A.Y., McCarthy T.J., *Self-Assembly Is Not the Reaction Possible between Alkyltrichlorosilanes and Surfaces: Monomolecular and Oligomeric Covalently Attached Layers of Dichloro-and Trichloroalkylsilanes on Silicon*. Langmuir, **2000**, 16, 7268-7274.
- [22] M. Yamaura, R.L. Camilo, L.C. Sampaio, M.A. Macedo, M. Nakamura, H.E. Toma, *Preparation and characterization of (3-aminopropyl)triethoxysilane-coated magnetite nanoparticles*. Journal of Magnetism and Magnetic Materials, **2004**, 279, 210-217.
- [23] P.J. Launer, *Silicone Compounds Register and Review*. Petrarch Systems: Levittown, PA, **1987**, 69.
- [24] A. Ulman, *An Introduction to Ultrathin Organic Films: from Langmuir-Blodgett to Self-Assembly*. Accademic Press: Boston, MA, **1991**.
- [25] M. Zwahlen, S. Herrwerth, W. Eck, M. Grunze, G. Hähner, *Conformational Order in Oligo(ethylene glycol)-Terminated Self-Assembled Monolayers on Gold Determinated by Soft X-ray Absorption*. Langmuir, **2003**, 19, 9305-9310.
- [26] P. Harder, M. Grunze, R. Dahint, G.M. Whitesides, P.E. Laibinis, *Molecular conformation in oligo(ethylene glycol)-terminated self assembled monolayers on gold or silver surfaces determines their ability to resist protein adsorption*. J. Phys. Chem. B, **1998**, 102, 426-436.
- [27] E.B. Abuin, M.A. Rubio, E.A. Lissi, *Solubility of Water in Water-in-Oil Microemulsions Stabilized by Cetyltrimethylammonium: Effects of the Surfactant Counterion, the Nature and Composition of the Oil, and the Salinity of the Droplets*. Journal of Colloidal and Interface Scienze, **1993**, 158, 129-132.
- [28] Fan, H. Y., E. W. Leve, C. Scullin, J. Gabaldon, D. Tallant, S. Bunge, T. Boyle, M. C. Wilson, C. J. Brinker, *Surfactant-assisted synthesis of water-soluble and biocompatible semiconductor quantum dot micelles*. Nano Lett., **2005**, 5, 645-648.
- [29] Hong Yang, Hong Zhou, Cuixia Zhang, Xuejian Li, He Hu, Huixia Wu and Shiping Yang, *Water-soluble magnetic CoO nanocrystals functionalized with surfactants as T₂-weighed MRI contrast agents in vitro*. Dalton Trans., **2011**, 40, 3616-3621.

In this chapter the synthesis and the microstructure of a series of ordered Mesoporous Silica Nanoparticles (MSN) and Magnetic Mesoporous Silica Nanoparticles (MMSN) are illustrated. With the aim of finding the suitable material to meet biological needs, some parameter of the synthesis (concentration of precursors, type of surfactant, time, concentration of magnetic nanoparticles) are modified so that different porous structures (hexagonal and cubic), different size and different compositions are obtained. The combined use of X ray diffraction at low and wide angle, Transmission Electron Microscopy, N₂-physisorption and Fourier Transformer Infrared Spectroscopy allowed to evidence the interesting features of the nanosystems. Magnetic properties are also studied in the case of the magnetic composites.

Chapter 5

Colloidal Magnetic Mesostructured Silica Nanoparticles

5.0 Experimental

5.1 Introduction

For many years, silica has been employed as a versatile and relatively benign material in material sciences and engineering due to the variety of available chemical and physical modifications that it offers as well as the biocompatibility.^[1] With the rapid advance of nanoscience over the past decades, nanosized porous amorphous silica has been investigated intensively and used in a wide variety of applications including catalytic supports, chromatography, sensor technology, and gas storage. The first mesoporous molecular sieves of the M41S family were developed by researchers at Mobil Corporation in 1992. These materials exhibit narrow pore size distributions, similar to those found for zeolites. Whereas the pore sizes of zeolites are typically less than 10 Å, the pores of the M41S materials can be tailored between 15 and more than 100 Å.^[2] This class of materials is characterized by very large specific surface areas, ordered pore systems, and well-defined pore radius distribution. The M41S materials can be obtained in different compositions, either as pure silica or as aluminosilicate. The M41S family has several well-known members like MCM-41 (Mobil Composition of Matter No. 41), MCM-48 and MCM-50. A unique feature of these materials is that although they are all composed of amorphous silica, they have a long-range ordered framework with uniform mesopores. The structure of MCM-41 (hexagonal phase, space group $p6mm$) consists of a hexagonal packing of one-dimensional channels with a pore diameter ranging between 20 and 100 Å. MCM-48 (cubic $Ia3d$ structure) has a bicontinuous structure, which

consists of two independent and intricately interwoven networks of mesoporous channels, while MCM-50 has a lamellar structure (space group p2) (figure 1).^[3,4]

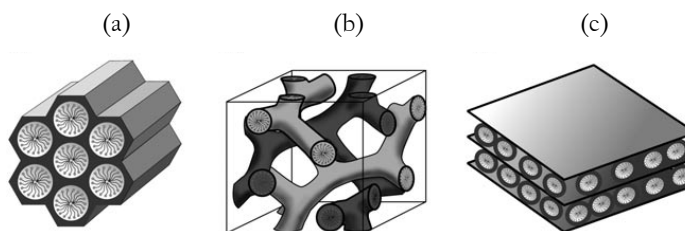


Figure 1. Structures of mesoporous M41S materials: a) MCM-41 (2D hexagonal, space group p6mm), b) MCM-48 (cubic, space group Ia3d), and c) MCM-50 (lamellar, space group p2).

A mesoporous material related to the M41S family is SBA-15 (Santa Barbara Amorphous No. 15). SBA-15 is a hexagonal silica with a larger pore size than MCM-41 (from 89 to more than 300 Å) and thicker silica cell walls. The use of supramolecular aggregates of ionic surfactants (long-chain alkyltrimethylammonium halides) as structure-directing agents (SDAs) was groundbreaking in the synthesis of these materials. These SDAs, in the form of a lyotropic liquid-crystalline phase, lead to the assembly of an ordered mesostructured composite during the hydrolysis and condensation of the silica precursors under basic conditions. The mesoporous materials are obtained by subsequent removal of the surfactant by extraction or calcination. In-depth investigations into the formation process of these composite materials have found that two different mechanisms are involved: on one hand, in true liquid-crystal templating (TLCT), the concentration of the surfactant is so high that under the prevailing conditions (temperature, pH) a lyotropic liquid-crystalline phase is formed without requiring the presence of the precursor inorganic framework materials (normally tetraethyl-(TEOS) or tetramethylorthosilicate (TMOS)).^[5] On the other hand, it is also possible that this phase forms even at lower concentrations of surfactant molecules, for example, when there is cooperative self-assembly of the SDA and the already added inorganic species, in which case a liquid-crystal phase with hexagonal, cubic, or lamellar arrangement can develop (figure 2).^[6,7]

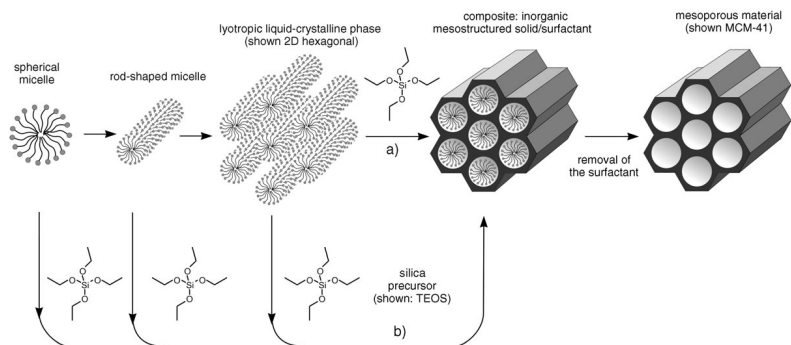


Figure 2. Formation of mesoporous materials by structure-directing agents: a) true liquid-crystal template mechanism, b) cooperative liquid-crystal template mechanism.

In the meantime, the original approach has been extended by a number of variations, for example, by the use of triblock copolymer templates (Pluronic 123) under acidic conditions by which means the so-called SBA silica phases may be synthesized. A fundamental condition for this method is that an attractive interaction between the template and the silica precursor is produced to ensure inclusion of the structure director without phase separation taking place. *Figure 3* illustrates the different interactions that can take place between the inorganic components and the head groups of the surfactants. These interactions are classified as follows: if the reaction takes place under basic conditions (whereby the silica species are present as anions) and cationic quaternary ammonium surfactants are used as the SDA, the synthetic pathway is termed S^+I^- (*figure 3(a)*; S: surfactant; I: inorganic species). The preparation can also take place under acidic conditions (below the isoelectric point of the SiOH-bearing inorganic species; pH-2), whereby the silica species are positively charged. To produce an interaction with the cationic surfactant, it is necessary to add a mediator ion X^- (usually a halide) (S^+XI^- ; pathway (b)). Conversely, when negatively charged surfactants (e.g., long-chain alkyl phosphates) are used as the SDA, it is possible to work in basic media, whereby again a mediator ion M^+ must be added to ensure interaction between the equally negatively charged silica species ($S^-M^+I^-$; pathway (c)); a mediator ion is not required in acidic media (SI^+ ; pathway (d)). Thus, the dominating interactions in

pathways (a-d) are of electrostatic nature. Moreover, it is still possible for the attractive interactions to be mediated through hydrogen bonds. This is the case when nonionic surfactants are used (e.g., S^0 : a long-chained amine; N^0 : polyethylene oxide), whereby uncharged silica species (S^{0I^0} ; pathway (e)) or ion pairs ($S^0(XI)^0$; pathway (f)) can be present.

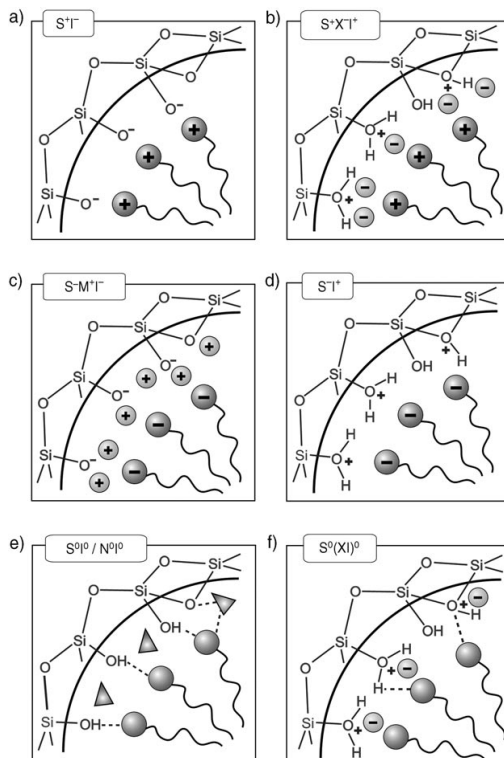


Figure 3. Interactions between the inorganic species and the head group of the surfactant with consideration of the possible synthetic pathway in acidic, basic, or neutral media. Electrostatic: S^+I^- , $S^+X^-I^+$, $S^-M^+I^-$, S^+I^- ; through hydrogen bonds: S^0I^0/N^0I^0 , $S^0(XI)^0$.

The syntheses of ordered mesoporous solids described above are classified as endotemplate methods (“soft-matter templating”). In exotemplate methods

(“nanocasting”), a porous solid is used as the template in place of the surfactant. Thus, this method is also known as “hard-matter templating”. The hollow spaces that provide the exotemplate framework are filled with an inorganic precursor, which is then transformed (cured) under suitable conditions. In this way, the pore system of the template is copied as a “negative image”. After removal of the now-filled exotemplate framework, the incorporated material is obtained with a large specific surface area (figure 4).^[8]

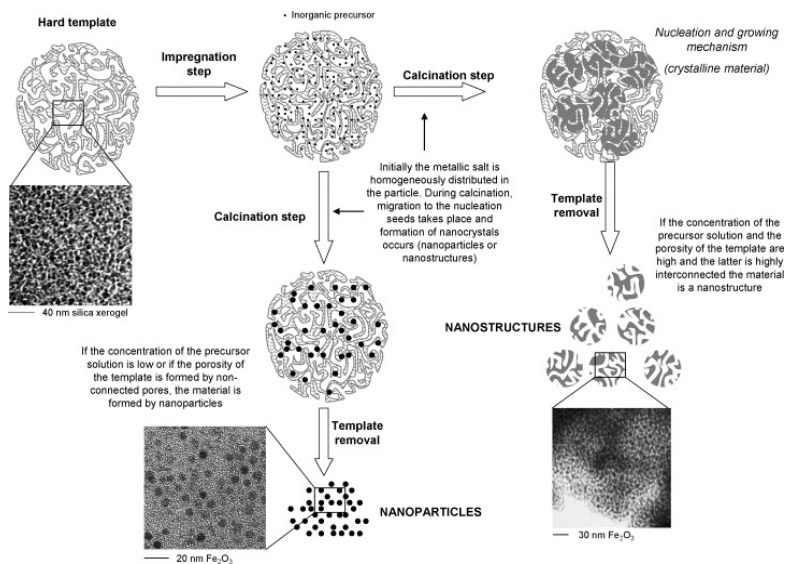


Figure 4. Examples of nanosystems obtained by the method nanocasting.

In fact, silica mesostructured nanoparticles show, besides to the typical features for mesostructured materials, ideal size (up to 100-150 nm) for across the biological membranes making them excellent candidates for imaging, labeling, and therapeutic when associated with magnetic or fluorescent nanoparticles or molecules.^[9] Furthermore, the reduced size and the low density allow to obtain them stable in water in colloidal form.

5.2 Mesoporous Silica Nanoparticles

To date, there have been great efforts made in the development of synthetic approaches for the preparation of mesoporous nanoparticles with narrow particle size distribution. Recent studies have shown that their tendency to aggregate in specific physiological conditions, or sizes greater than 150 nm, limit their use in the biomedical field. In fact mesoporous nanoparticles with diameters greater than 100 nm are rapidly taken up by the reticuloendothelial system (RES), accumulating in the liver and spleen before a loaded drug can be delivered to the target cells/tissue,^[10] but that smaller silica NPs (<50 nm diameter) with poly(ethylene glycol) (PEG) modification have significantly decreased uptake by RES organs and exhibit a longer blood circulation time. Although well-ordered mesoporous nanoparticles with diameters as low as 20 nm have been synthesized using a double surfactant system, the resulting nanoparticles aggregate easily and, thus, discourage effort to incorporate other functionality such as magnetic contrast, because the base nanoparticle is not appropriate for biomedical use.^[11,12]

However, it has been demonstrated that mesoporous silica nanoparticles of size between 25-255 nm have a low toxicity and high stability, for the same size compared to the non-porous silica nanoparticles. It has also been shown that toxicity values depend strongly from integrity of the mesopores.^[13] Therefore it is important to choose the appropriate method of synthesis that allows to obtain silica nanoparticles with mesoporous structure, with such sizes as to be stable, non-toxic, and easily used in different biomedical and pharmaceutical applications. In a typical synthesis of hexagonal mesoporous silica (*figure 5*), the silicate source, tetraethylorthosilicate (TEOS), is mixed with the cationic surfactant cetyltrimethylammonium bromide (CTAB) in a basic aqueous solution. The nanoparticles are formed using the micellar templates of 2.0 to 2.5 nm in size which grow into mesoporous spherical nanoparticles with diameters of 50 to 200 nm, during the base-catalysed sol-gel process. The cationic surfactant is assembled with silicates through electrostatic interaction, producing an ordered mesophase. The mesoporous nanoparticles are obtained by subsequent removal of the

surfactant by extraction in acidic alcohol or calcination, due to the rupture of the electrostatic interaction between the cationic surfactant head groups and the anionic silicates.^[14] It is possible to summarize the formation mechanism of mesoporous nanoparticles in three stages: (1) hydrolysis of alkoxy silanes and formation of silica oligomers, (2) formation of silica/CTAB primary particles, and (3) mesopore growth via aggregation of the primary particles.^[15]

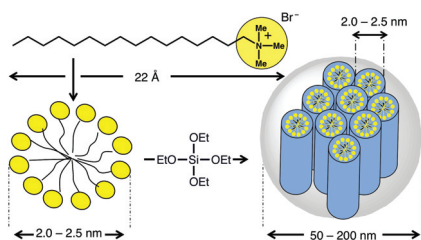


Figure 5. A graphical representation of a typical sol-gel synthesis of mesoporous spherical nanoparticles from cetyltrimethylammonium bromide.

Compared to hexagonal mesoporous silica, the three-dimensional cubic (Ia3d) mesostructure has an interesting mesostructure, which consists of two interpenetrating continuous networks of chiral channels. This unique three-dimensional channel network is thought to provide a highly opened porous host that provides easy and direct access for guest species, thus facilitating inclusion or diffusion throughout the pore channels without pore blockage.^[6] This structure makes the material interesting for example, as a carrier for biologically active molecules.^[16] Conventionally, the synthesis of MCM-48 materials is carried out through hydrothermal routes, but the hydrothermal synthesis methods typically take a long time, require high temperatures. Moreover, it gives a large particle size above 1 μm with irregular morphologies. In contrast to the hydrothermal recipes, the modified Stober method, requires only a short synthesis time at room temperature.^[17] The authors declare that this method produces monodisperse spherical MCM-48 mesoporous silica nanoparticles under the conditions of low cation surfactant (CTAB)/TEOS molar ratio, with high stirring rate. The addition of triblock copolymer Pluronic F127 (figure 6) as a nonionic surfactant decreases the size of silica nanoparticles, thanks to a favorable interaction of F127 with silicates through the

hydrogen bonds, limiting the growth of the mesostructure particle grain.^[12] Recently cubic mesoporous silica nanoparticles were obtained via base-catalysed sol-gel silica reactions using CTAB, TEOS, and functionalized with amino group, through the co-condensation of the high molar amounts of 3-aminopropyl triethoxysilane (APTES).^[18]

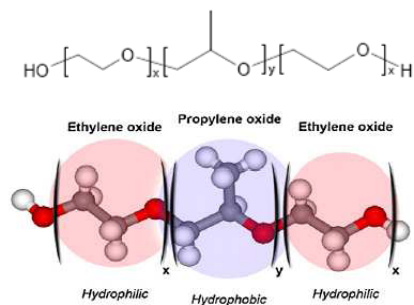


Figure 6. Pluronic F127 is a polymer of polyoxyethylene (PEO) and polyoxypropylene (PPO) with two 96-unit hydrophilic PEO chains surrounding one 69-unit hydrophobic PPO chain.


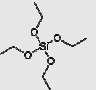
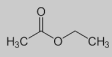
In general, the factors that control the morphology, the mesoporous structure type, and size of silica nanoparticles, are: the cationic surfactant/TEOS molar ratio, time, stirring rate, the addition of a co-surfactant, or functional group, and no less important the chain length of cationic surfactant, because this has effect on the packing parameter, g ($g=V/a_0l$, where V is the total volume of the surfactant chain plus any cosolvent molecules between the chains, a_0 is the effective head-group area at the organic-inorganic interface, and l is the surfactant chain length).^[19]

5.3 Hexagonal and Cubic Mesostructured Silica nanoparticles (MSN_H, MSN_C): synthesis and characterization

5.3.1 Synthesis

Hexagonal mesostructured silica nanoparticles (MSN_H) have been synthesized starting from the following molar ratios: 0.82 TEOS: 8.3 NH₃: 1 CTAB: 2.03 H₂O: 1.87 EtOAc, using cetyltrimethylammonium bromide, CTAB (Aldrich, 96%), ammonia, NH₄OH (Aldrich, 30%), tetraethylorthosilicate, TEOS (Aldrich, 98%), and ethylacetate, EtOAc (Aldrich, 99%), following the procedure schematically described in *figure 7*. In *table 1* the reagents are listed, with the formulas and their functions in the reaction environment.

Table 1. Reactants Information.

Reagents	Formula	Manufacturer	Purity	Function
CTAB Cetyltrimethylammonium Bromide		Aldrich	96%	Templating Agent
TEOS Tetraethylorthosilicate		Aldrich	98%	Precursor of the silica
EtOAc Ethylacetate		Aldrich	99%	Inhibitor of growth of the nanoparticles

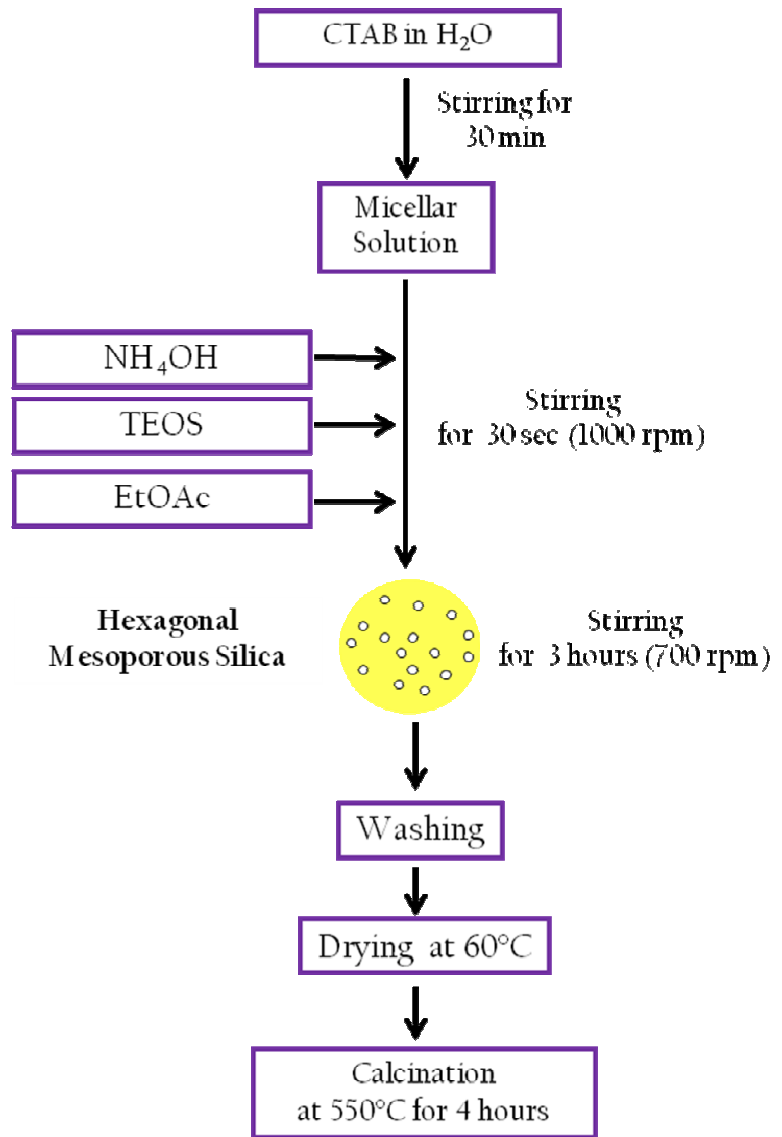





Figure 7. Schematic representation of the synthesis of MSN_H mesoporous silica nanoparticles with hexagonal pore structure (H).

Cubic mesostructured silica (MSN_C) nanoparticles have been obtained by a modification of the well-known Stöber method through a procedure schematically reported in *figure 8*, starting from the following molar ratios: 6.25 TEOS: 125 NH₃: 540 EtOH: 1 CTAB: 4170 H₂O: 0.195 F127.^[12] As for the case of hexagonal mesoporous nanoparticles, silica nanoparticles have been obtained through base-catalyzed sol-gel process, using besides the cationic surfactant CTAB, an anionic surfactant like Pluronic F127. In *table 2* has been reported the information about the reagents.

Table 2. Reactants Information.

Reagents	Formula	Manufacturer	Purity	Function
CTAB Cetyltrimethylammonium bromide		Aldrich	96%	Templating Agent
PLURONIC F127		Aldrich	-	Inhibitor of growth of the nanoparticles
TEOS Tetraethylorthosilicate		Aldrich	98%	Precursor of the silica

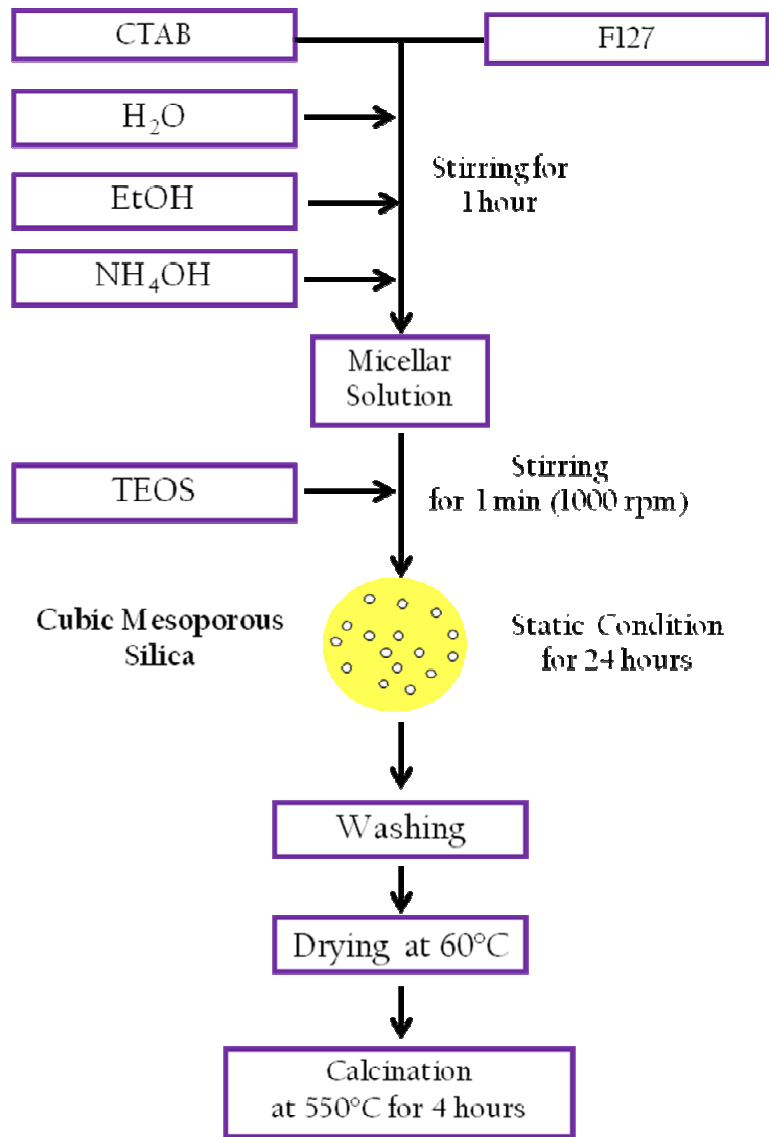


Figure 8. Schematic representation of synthesis of the MSN_C mesoporous silica nanoparticles with cubic pore structure (C).

According to the synthesis described above, three samples for each type of silica (hexagonal and cubic) have been prepared: two samples in identical conditions to check the repeatability of the method (MSN_H_1, MSN_H_2; MSN_C_1, MSN_C_2;), and a third one with a concentration of ethylacetate 1.2 times higher than the other samples (MSN_H_3) or with a concentration of Pluronic F127 1.2 times higher than the other samples (MSN_C_3), to verify how this parameter can influence the particle size and structure of the mesoporous silica nanoparticles. The tables 3a and 3b shows the synthesis conditions of the three samples.

Table 3a. Synthesis conditions for the MSN_H samples.

Sample	CTAB (mmol)	H ₂ O (mmol)	NH ₄ OH (mmol)	TEOS (mmol)	EtOAc (mmol)
MSN_H_1	0.68	13.9	56.75	5.57	12.77
MSN_H_2	0.68	13.9	56.75	5.57	12.77
MSN_H_3	0.68	13.9	56.75	5.57	15.21

Table 3b. Synthesis conditions for the MSN_C samples.

Sample	TEOS (mol)	NH ₃ (mol)	EtOH (mol)	CTAB (mol)	H ₂ O (mol)	F127 (mol)	Static time
MSN_C_1	6.25	125	540	1	4170	0.19	24 h
MSN_C_2	6.25	125	540	1	4170	0.19	24 h
MSN_C_3	6.25	125	540	1	4170	0.23	24 h

5.3.2 Microstructural and textural Characterization

TEM analysis of the sample MSN_H_1 shows nanoparticles with spheroidal morphology (figure 9(a)) and evidences the ordered structure of the pores typical for an hexagonal arrangement (figure 9(b)). The particle size distribution histogram (figure 9(c)) shows a particle size range from 70 to 175 nm, with an average size of 124 nm and a standard deviation of 26 nm (polydispersity 21%). TEM measurements on the sample MSN_H_2

(figure 9(d) and 9(e)), confirm the repeatability of the procedure as regards both the morphology / texture of particles (shape and porosity), and the particle size distribution, being the average particle size value 129 nm and the standard deviation 25 nm (polydispersity 19%).

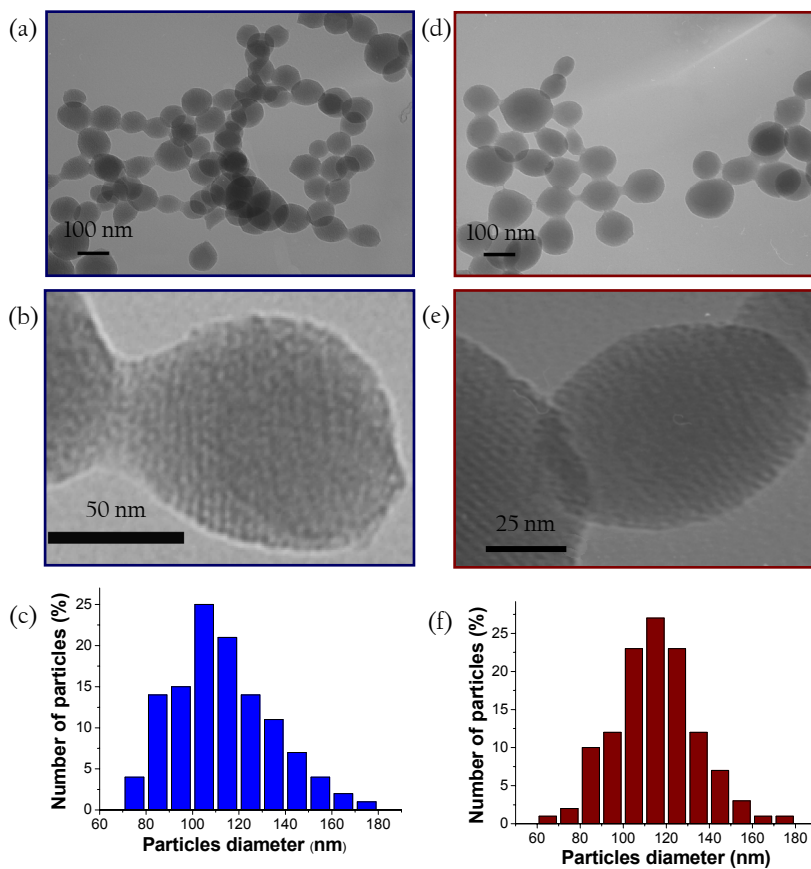


Figure 9. Bright Field TEM images at low and high magnification and particle size distribution histograms of the MSN_H_1 (a,b,c) and MSN_H_2 (d,e,f) mesoporous silica samples.

The sample MSN_H_3 (figure 10(a) and 10(b)), in which the concentration of ethyl acetate has been increased, show the formation of aggregated irregular shaped silica

nanoparticles. This would suggest that, above a certain concentration, the ethyl acetate not only loses its primary function of size modulator and growth inhibitor but also can affect the CTAB templating agent action.

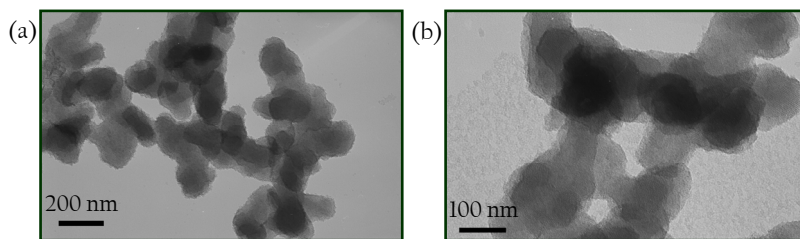


Figure 10. Bright Field TEM images of the MSN_H_3 sample (a,b).

TEM images of the sample MSN_C_1, show spherical nanoparticles (*figure 11(a)*) with a clear bimodal particle size distribution and evidence, for all the nanoparticles, the ordered pore structure typical for pores with cubic arrangement (*figure 11(b)*).

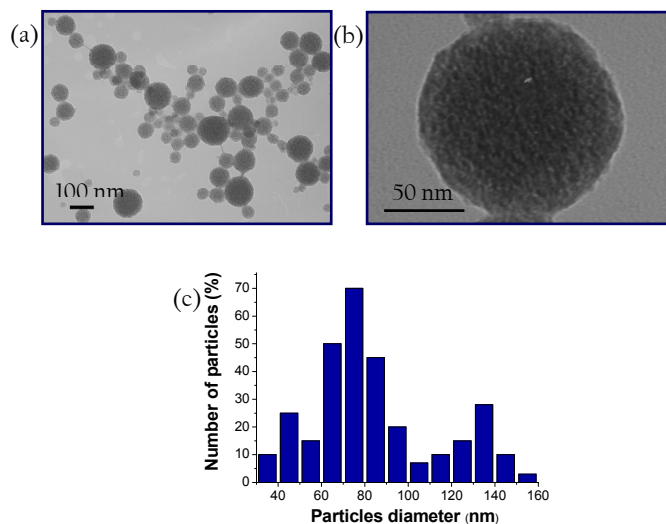


Figure 11. Bright Field TEM images (a,b) and particle size distribution (c) of MSN_C_1 sample.

A fraction of the nanoparticles shows an average particle size centered at 75 nm, while the other one is centered at about 140 nm. This result is in agreement with the literature: monodisperse low porous silica spheres prepared with the Stober method can be obtained solely when the silica particle size is bigger than 200 nm, while for the smaller particles this method leads often to a bimodal or multimodal distribution. The analysis of the sample MSN_C_2 confirms the presence of spherical nanoparticles with a bimodal size distribution, proving the repeatability of the synthesis.

When the concentration of Pluronic F127 is increased (MSN_C_3) a small decrease on the size of the two nanoparticle fractions can be evidenced: the smaller particles are centered at ca. 65 nm (-10 nm) while the bigger one are centered at 125 (-20 nm). This would suggest that the Pluronic acts as size modulator and growth inhibitor. In any case, to better verify this effect it should be useful to prepare a series of samples in which the concentration of the F127 is changed in a wider range.

As expected, the wide-angle X-ray diffraction pattern of the thermally treated MSN_H and MSN_C samples (*figure 12 (a) and (c)*) shows the silica amorphous nature, as evidenced by the presence of a broad halo centered at about $2\theta = 23^\circ$.

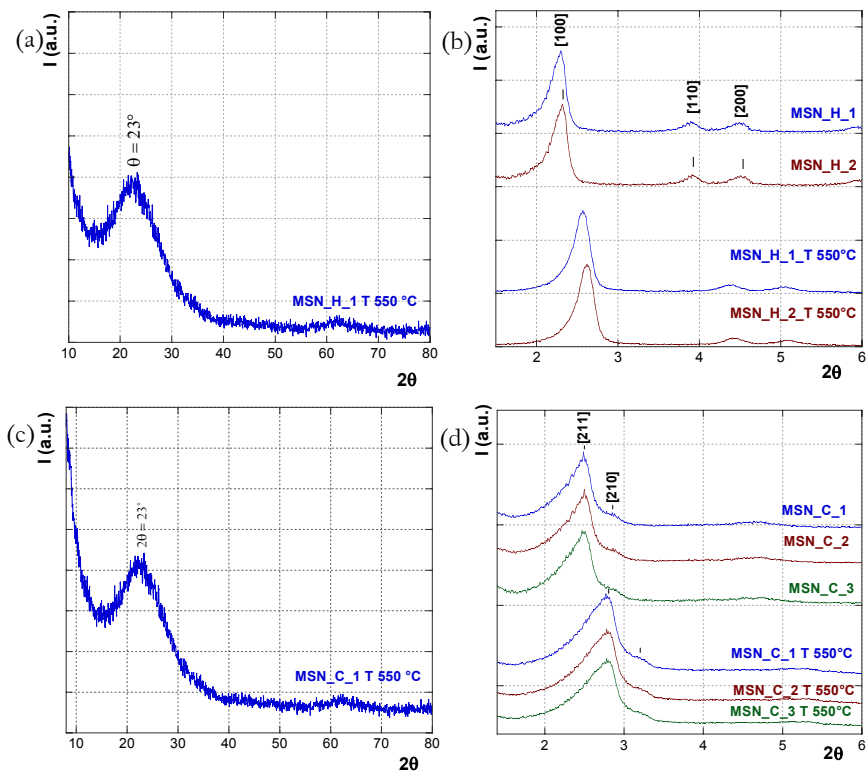


Figure 12. Wide angle XRD pattern of MSN_H_1 and MSN_C_1 samples (a and c) and Low angle XRD patterns of MSN_H and MSN_C samples before and after calcination at 550°C in air (b and d).

The Low-angle X-ray diffraction patterns (*figure 12(b)*), for the MSN_H_1 and MSN_H_2 samples, before and after calcination, show three characteristic reflexes, (100),(110),(200), indicating a long-range ordering and a hexagonal pore structure (space group $p6mm$). It can be noticed that the samples after calcination show a shift of reflexes versus θ higher values and a corresponding decrease of the cell parameter (*table 4a*), probably due to contraction of porous structure caused by the elimination of the surfactant.^[13] For all the MSN_C samples the low angle patterns evidence two characteristic reflexes, (211), (210), typical for a cubic pore structure (space group $Ia3d$).

As for the samples with exagonal pore structure, as expected, the calcination induces the a shift of the two reflexes versus higher θ values (*table 4b*)

N_2 adsorption-desorption isotherms (*figure 13*) for the MSN_H and MSN_C exhibit the characteristic IV behavior for a well-developed micro-mesoporous structure.^[20] The first step in a relative pressure range of 0.20-0.4 is attributed to the nitrogen condensation that took place at the internal mesopores, and second step above 0.95 in the adsorption represents the formation of interstitial pores. All the samples show high surface area (S_{BET}) and total pore volume (V_p), with mesopores diameter (D_{pore}) in the 2.3-2.6 nm range. The textural and structural parameters are reported in *table 4*.

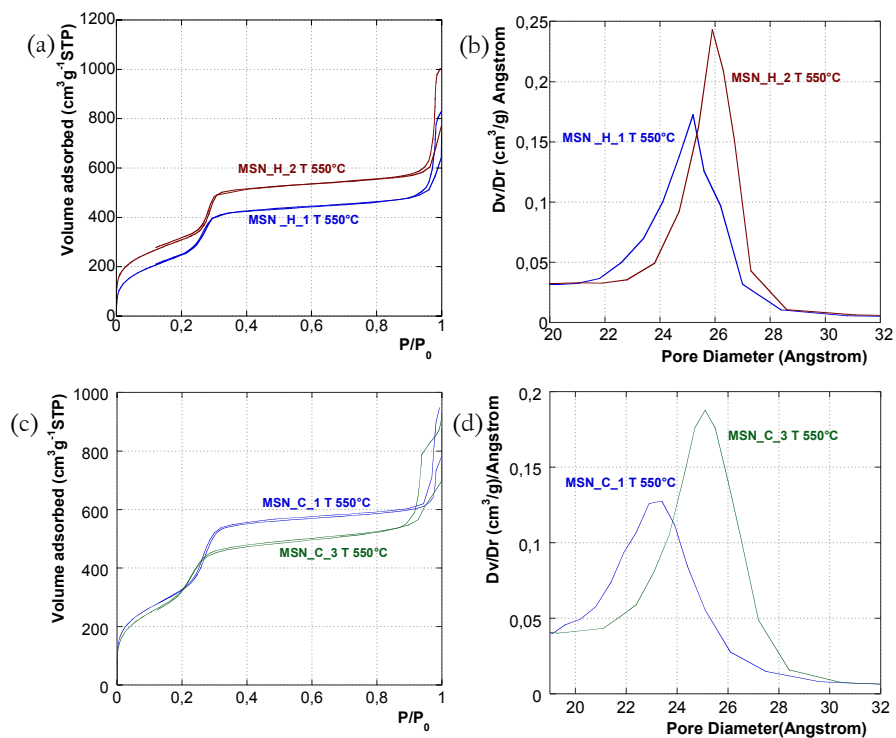


Figure 13. Nitrogen adsorption-desorption isotherms (a, c), and the pore size distribution (b, d) for MSN_H and MSN_C samples.

Table 4a. Structural Parameters of MSN_H_1 and MSN_H_2 samples.

Sample	S_{BET} ($\text{m}^2 \text{g}^{-1}$)	V_p ($\text{cm}^3 \text{g}^{-1}$)	$(w_{\text{BjH}})^\dagger$ (nm)	d_{100} (nm)	a_0^* (nm)	D_{pore} (nm)
MSN_H_1	-	-	-	3.8	4.4	-
MSN_H_1 T 550°C	992	0.9	1.4	3.4	4.0	2.5
MSN_H_2	-	-	-	-	4.4	-
MSN_H_2 T 550°C	1140	1.0	1.4	3.4	3.9	2.6

*The lattice parameter (a_0) was calculated by the equation: $a_0 = \frac{2d_{100}}{\sqrt{3}}$ through X-ray diffraction data. †The wall thickness (w_{BjH}), was calculated from the difference between the lattice parameter (a_0) and the pore size (D_{pore}).

Table 4b. Structural Parameters of MNS_C_1 and MNS_C_3 samples.

Sample	S_{BET} ($\text{m}^2 \text{g}^{-1}$)	V_p ($\text{cm}^3 \text{g}^{-1}$)	$(w_{\text{BjH}})^\dagger$ (nm)	d_{211} (nm)	a_0^* (nm)	D_{pore} (nm)
MSN_C_1	-	-	-	3.5	8.7	-
MSN_C_1 T 550°C	1441	0.9	1.3	3.2	7.7	2.3
MSN_C_3	-	-	-	3.5	8.7	-
MSN_C_3 T 550°C	1292	1.1	1.3	3.2	7.8	2.5

*The lattice parameter (a_0) was calculated by the equation: $a_0 = \sqrt{6} \times d_{211}$ through X-ray diffraction data. †The wall thickness (w_{BjH}), was calculated by the equation: $\left(\frac{a_0}{3.092}\right) - \left(\frac{D_{\text{pore}}}{2}\right)$

The FTIR spectrum of the samples MSN_H and MSN_C, before calcinations, (figure 14 (a) and 14 (b)) exhibits a series of adsorptions attributable to the presence of CTAB (MSN_H) and CTAB/F127 (MSN_C): the symmetric (3010 cm^{-1}), CH_3 stretching modes, symmetric, asymmetric ($2920\text{-}2850 \text{ cm}^{-1}$) stretching, the bending (1450 cm^{-1}), and the rocking ($1400\text{-}720 \text{ cm}^{-1}$) modes of CH_2 group. Once the samples are subjected to

calcinations, the spectra show a series of bands typical of vibrational modes of pure silica: the symmetric stretching modes of the Si-O-Si group at 1240 cm^{-1} , 1060 cm^{-1} , and 800 cm^{-1} , the stretching mode at 960 cm^{-1} of the Si-OH group, and the bending mode at 460 cm^{-1} of O-Si-O group. The absence of bands associated to CTAB or F127 suggests that the surfactants have been completely removed during the calcinations treatment.

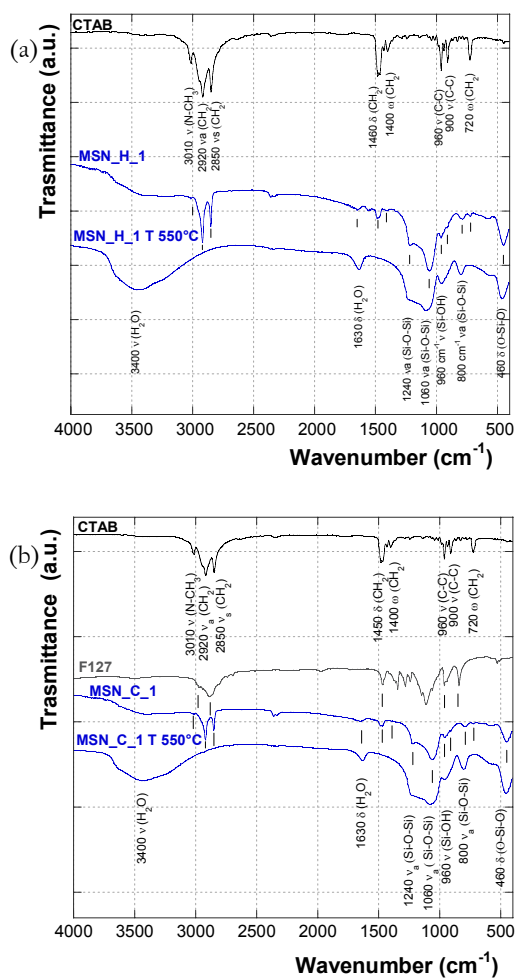


Figure 14. FTIR spectra of the samples MSN_H_1 (a), MSN_C_1 (b) before and after calcinations in air. CTAB and F127 spectra have been also reported for comparison.

The thermogravimetric analysis of the MSN_H (*figure 15(a)*) and MSN_C (*figure 15(b)*) samples before the calcination show a first weight loss up to 200 °C due to desorption of physically adsorbed water, and a second one, from 200 °C to 550 °C due to the complete removal of the surfactants. The weight loss in this range is similar for all the samples (from 45 to 47%). Beyond the temperature of 550 °C a small weight loss is observable due the collapse of the structure of the mesoporous silica, due to the condensation of the Si-OH groups to form adjacent Si-O-Si groups with the consequent elimination of the water molecules. For comparison, thermogravimetric analysis of the CTAB and the F127 has been reported.^[21-23] As expected, the thermally treated samples show only a small weight loss (2-3%) up to 200°C due to the adsorbed water.

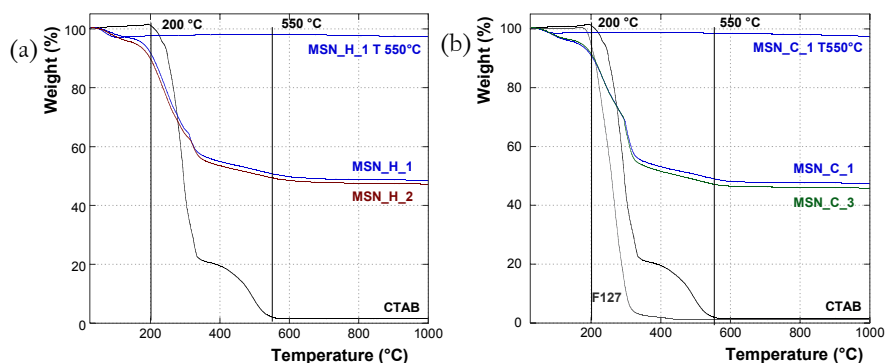


Figure 15. Thermogravimetric curves of the samples (a) MSN_H_1 and MSN_H_2; (b) MSN_C_1 and MSN_C_3, before and after calcination in air. CTAB and F127 have been also reported for comparison.

For a possible use of the silica nanoparticles in the biomedical field is of fundamental importance to study the stability of the colloidal suspensions in water. The products recovered by centrifugation at 10000 rpm has been washed several times in water and the stability over time has been studied up to four months. As can be seen from the images shown in *figure 16* the samples MSN_H_1, MSN_H_2 (*figure 16*) and MSN_C_1, MSN_C_2 and MSN_C_3 (*figure 17*) are stable for over 4 months (*figure 16(a)* and (b)), while the sample MSN_H_3 in which the amount of the ethyl acetate was increased

(figure 16(c)) become unstable after less than a week. The stability in water of the samples MSN_H_1 and MSN_C1 after the treatment at 550 °C has been also studied; the dried powder dispersed in water and submitted to several (5-6) short (15 seconds) ultrasound treatment cycles is stable up to 3 days. It has been taken into account that the stability over time has been studied solely through a visual observation and in order to study the phenomenon for the microscopic point of view it should be necessary to perform further characterizations.



Figure 16. Stability in water of MSN_H_1 (a), MSN_H_2 (b) after 4 months and of MSN_H_3 (c) after one week.

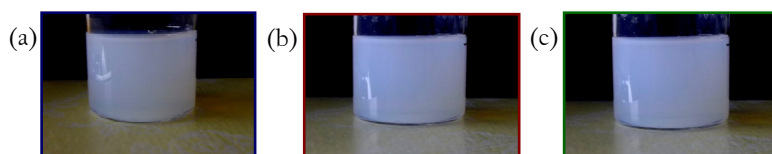


Figure 17. Stability in water of the MSN_C_1 (a), MSN_C_2 (b), and MSN_C_3 (c) samples after 4 months.

5.4 Magnetic mesostructured silica based nanoparticles (MMSN_H and MMSN_C): Synthesis, characterization and magnetic properties

5.4.1 Introduction

As underlined in the other chapters, the hydrophobic magnetic nanoparticles prepared by HTDSA method, being dispersible in organic solvents, cannot be used, as such, for biomedical applications. In chapter 4 has been demonstrated how to convert them in hydrophilic systems through exchange ligand and intercalation processes, but the

corresponding molecular organic-functionalized nanoparticles could interact with other molecules in the biological environment, so that a more robust coating is often preferred for some applications. For this point of view, silica can be considered the ideal coating-material, and sol-gel represents the most versatile approach in order to prepare magnetic low-porosity or high-porosity silica based systems. Recently, we have demonstrated that monodisperse low-porosity core-shell $\text{CoFe}_2\text{O}_4\text{-SiO}_2$ nanoparticles can be prepared starting from hydrophobic nanoparticles and a base-catalyzed sol-gel process in the presence of an oil in water (cyclohexane/Igepal-CO520/water) microemulsion.^[24] However, the low porosity of these systems can limit their applications, therefore, it should be very useful to set up new synthetic methodologies in order to prepare new magnetic composites with high mesoporosity. The high surface area and the presence of mesopores should allow the encapsulation of an high number of magnetic nanoparticles (high saturation magnetization), the entrapment of other inorganic nanoparticles with optical properties, and the physically or chemically bound of high concentrations of organic molecules.

The proposed synthetic strategy is based on the use of a sol-gel process in the presence of “pseuso micelles”, made up of an inorganic core and an organic shell that ends with a polar head, that have been used as the *building block* for the formation of the mesophase. In this context, the molecule CTAB plays a key role: it allows the dispersion of hydrophobic magnetic nanoparticles into a polar solvent, the common reaction environment for sol-gel routes, and can be used as template (porogen agent) for the ordered pore structure. By analogy with the synthetic route used for pure mesostructured silica nanoparticles (paragraph 5.3), this strategy should lead to the formation of functionalizable magnetic mesostructured silica nanospheres with high surface area and high porous volume (*figure 18*).

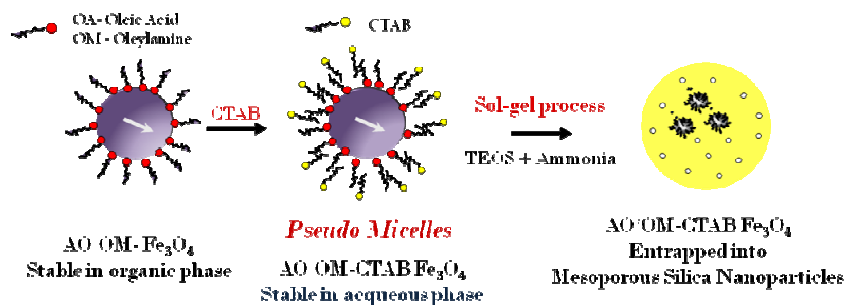


Figure 18. Schematic illustration of the magnetic nanoparticles encapsulation into a mesoporous silica nanoparticles.

5.4.2 MMSN_H Synthesis

In order to prepare magnetic mesoporous silica nanospheres with hexagonal and cubic pore structure, hydrophobic magnetic nanoparticles made up of oleic acid/oleylamine capped magnetite (MAG_6nm for the MMSN_H composites, and MAG_12nm for the MMSN_C samples), have been first made hydrophilic by intercalation with CTAB molecules (MMSN_H composites) or with CTAB and F127 (MMSN_C composites), following a procedure similar to that described in chapter 4. Then, the resulting “pseudo micelles” have been used, instead of pure CTAB micelles, to create the hexagonal pore structure that has been coated, through a base-catalyzed sol-gel process, by TEOS and then silica. This soft-chemistry strategy should permit to entrap the preformed magnetic nanoparticles into mesostructured silica nanospheres without any significant modification of their magnetic properties. The synthesis procedures, schematically described in *figure 18* (MMSN_H samples) and in *figure 19* (MMSN_C), have been used to prepare two composites with hexagonal pore structure with 5% (MMSN_H_1) and 10% (MMSN_H_2) in weight of the magnetic phase and one composite with a cubic pore arrangement (MMSN_C_1) with 5% in weight of magnetite.

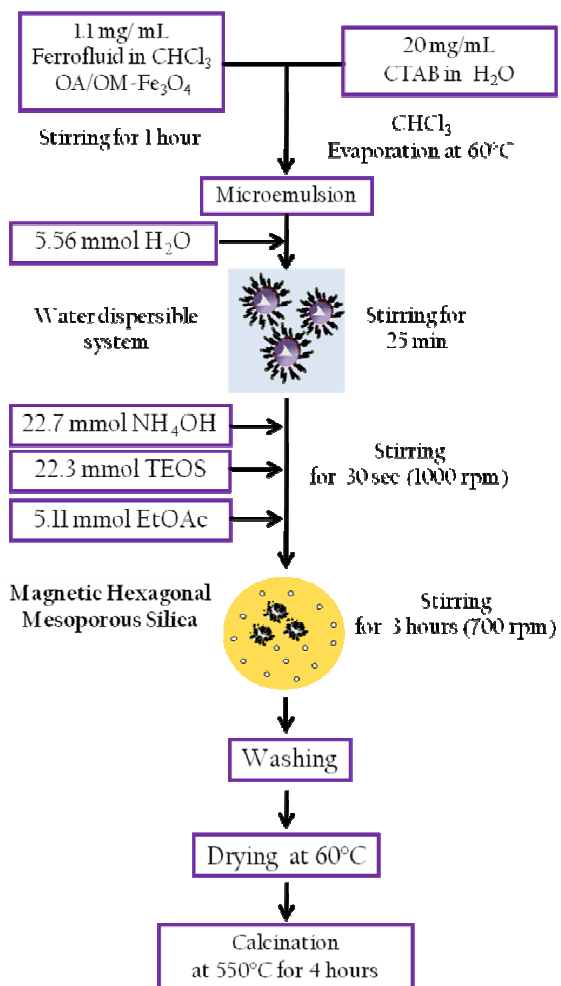


Figure 18. Schematic representation of synthesis of MMSN_H magnetic mesoporous silica composites with hexagonal pore structure (H). The amounts are referred to the sample MMSN_H_1 with 5% in weight of the magnetic phase.

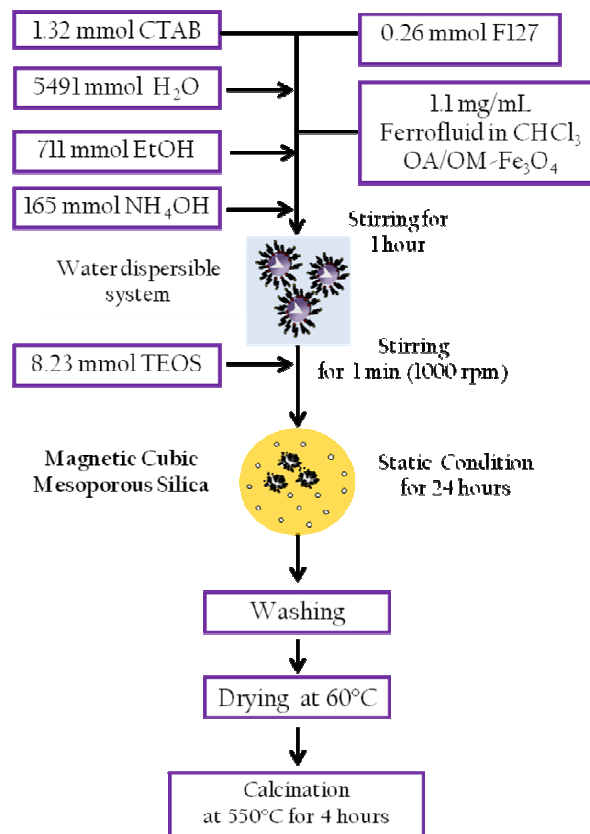


Figure 19. Schematic representation of synthesis of MMSN_C magnetic mesoporous silica composites with cubic pore structure (H). The amounts are referred to the sample MMSN_C_1 with 5% in weight of the magnetic phase.

5.4.3 Characterization

TEM images (figure 20(b,c)) of the MMSN_H_1 revealed that the mesoporous silica spheroidal-hexagonal nanoparticles possess a well-ordered mesoporous structure and are quite uniform in size (polydispersity of 16%) with an average particle diameter of around 76 nm, which is within applicable size range for biomedical applications. Each

silica sphere contained several single magnetite nanocrystals of 6 nm in size (from ca 3 to 10), and, as observed by the dark field mode image, the embedded magnetite nanocrystals retained the original size and crystallinity. The MMSN_H_2 sample, with the double concentration of the magnetic phase, still preserve the ordered pore arrangement, as well as the size and the shape. The particle size distribution, reported in *figure 20*, indicates an average particle size of 73 nm and a polydispersity of 15%; values just slightly lower than that obtained for the most diluted sample. It can be further notice that the magnetic particle are not homogeneously disperse inside the silica porous nanosphere, but rather they tend to cluster: this effect can be due to the magnetic interparticle interaction or to a different self-assembling process of the “CTAB-Oleic Acid-Magnetic Nanoparticle” micelles compared to that of the pure CTAB micelles. Another important result that derive from the incorporation of the preformed magnetic phase, is that the average size and polydispersity values of the nanoparticles are strongly reduced; this represents a great advantages for their possible application. A possible explanation of this behaviour can be found in the differences in the self-assembling phenomenon that derive from the differences in the porogen agent. The interactions among CTAB micelles for the formation of the mesophase are certainly different from the ones among the “pseudo hybrid micelles”.

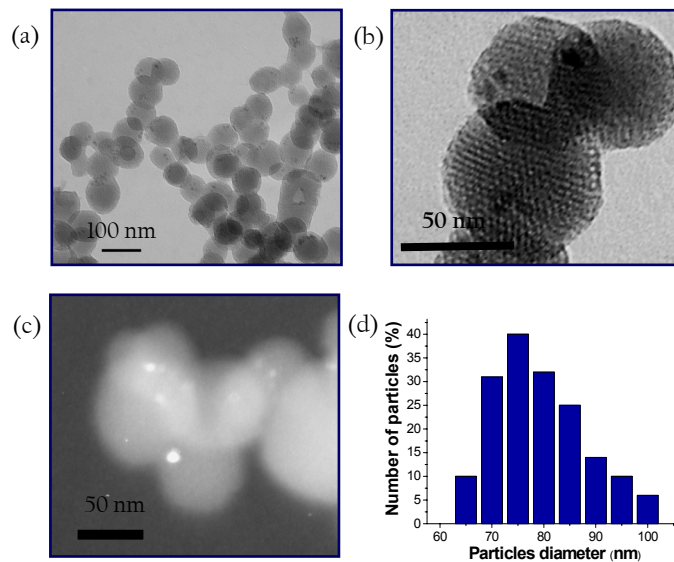


Figure 20. TEM images, in Bright Field mode and at different magnifications (a,b), in Dark Field mode (c), and particle size distribution (d) of the sample MMSN_H_1 (5% in weight).

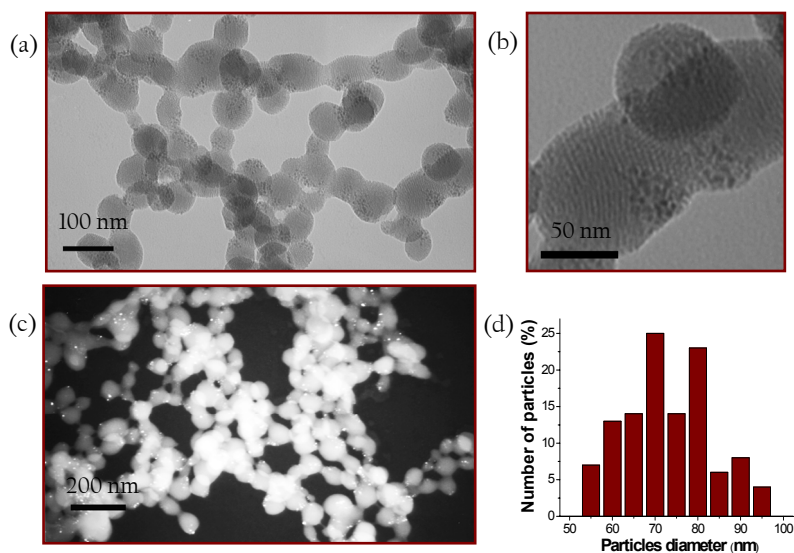


Figure 21. TEM images, in Bright Field mode and at different magnifications (a,b), in Dark Field mode (c), and particle size distribution (d) of the sample MMSN_H_2 (10% in weight).

TEM analysis of MMSN_C_1 sample evidences a monodisperse system with spherical morphology of the particles (figure 22(a)). The monomodal particle size distribution (figure 22(d)) shows a size range from 95 to 135 nm, with average size of 110 nm and standard deviation of 8.6 nm (polydispersity 8%). Bright field and dark field images show as all the silica particles contain from 1 to 5 magnetic nanoparticles, and no pure silica nanoparticles are observed; silica nanoparticle size gradually increases by increasing the number of encapsulated magnetic nanoparticles. As in the case of the hexagonal systems, the incorporation of the magnetic phase induces an improvement on the nanoparticle features: the particle size distribution from bimodal becomes monomodal and the polydispersity decreases.. Unfortunately, differently from the MMSN_ H samples, TEM images, also at high magnification, don't allow to give information about the micro/mesoporosity or about the pore order.

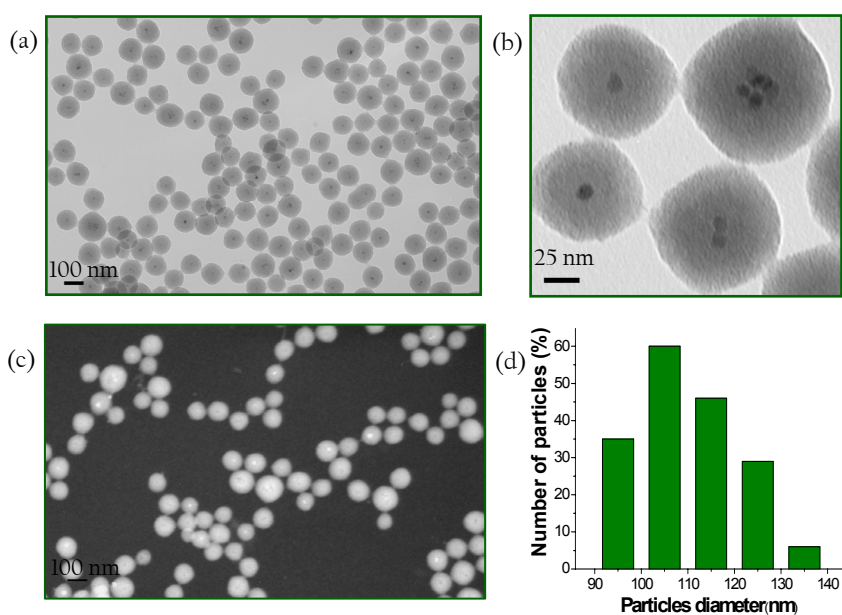


Figure 22. TEM images, in Bright Field mode and at different magnifications (a,b), in Dark Field mode (c), and particle size distribution (d) of the sample MMSN_C_1 (5% in weight).

Figure 23(a) shows the wide angle XRD patterns of the magnetic mesoporous silica nanocomposite samples with hexagonal pores structure (MMSN_H_1 and MMSN_H_2), before and after calcination at 550°C. For comparison, the magnetic core of 6 nm in size (MAG_6nm) and the pure hexagonal mesoporous silica before and after thermal treatment (MSN_H_1) have been also reported. XRD pattern of the MMSN_H samples before thermal treatment revealed besides the halo associated to the amorphous silica, small and broad reflections due to the presence of the magnetic nanophase. Their intensity increases with the magnetic phase content, while their width is similar to that of the magnetic core, confirming that the size of the preformed magnetic nanoparticles is retained also after the treatment in air at 550°C. However, it has to be taken into account that the thermal treatment in air should lead to a complete oxidation of Fe(II) to Fe(III) with the consequent conversion of the magnetite into the maghemite phase with similar structure. Furthermore, the thermal treatment induces an evident shift of the silica band maximum versus higher 2θ values (from ca. 21° to ca. 23°): this effect, being clearly visible also in the pure silica sample, suggests a rearrangement of the Si-O-Si and Si-OH bonds due to the elimination of the surfactants (CTAB and oleic acid). Similar results have been observed for the MMSN_C_1 sample with cubic pore structure (*figure 23(b)*), though the shift of the silica halo is very slighter if compared with the hexagonal porous systems thus suggesting a weaker interaction between silica and the surfactants (CTAB+FI27).

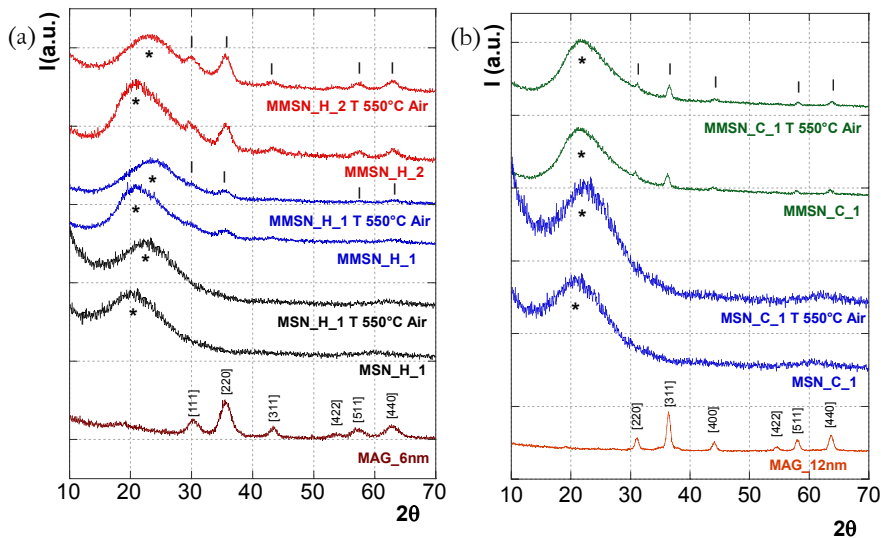


Figure 23. Wide-angle XRD patterns of the (a) MMSN_H_1 and MMSN_H_2 and of the (b) MMSN_C_1 samples before and after calcination in air. For comparison the magnetic phases MAG 6nm and MAG 12nm and pure silica samples MSN_H_1 and MSN_C_1 before and after thermal treatment in air have been reported.

Low-angle X-ray diffraction measurements have been also performed to extract information on the pores structure (figure 24(a)). The MMSN_H samples, before and after thermally treatment in air, show the three characteristic reflexes, (100),(110),(200), indicating a long-range ordering of the hexagonal pore structure (space group $p6mm$), confirming TEM data. It can be noticed that, as for the pure silica samples (MMSN_H), the MMSN_H samples after calcination show a shift of reflexes at higher values of θ probably due to contraction of porous structure due to the surfactant removal. Unlike literature data, the ordering of the porous structure doesn't decrease as the concentration of the guest phase increases, thus opening the possibility to synthesize mesoporous composites with higher amount of magnetic phase.

Low-angle X-ray diffraction patterns for the MMSN_C_1 sample before and after thermally treatment in air (figure 24(b)) have been also performed in order to understand if the magnetic composite shows an ordered porous structure. The two characteristic

reflexes (211) and (220), indicate a cubic pore arrangement with the space group Ia3d as to the pure silica sample (MSN_C) and the hexagonal-composites, the calcination induce the shift of reflexes at higher values of θ , due to the removal of CTAB and F127 molecules and the consequent contraction of the pore structure.

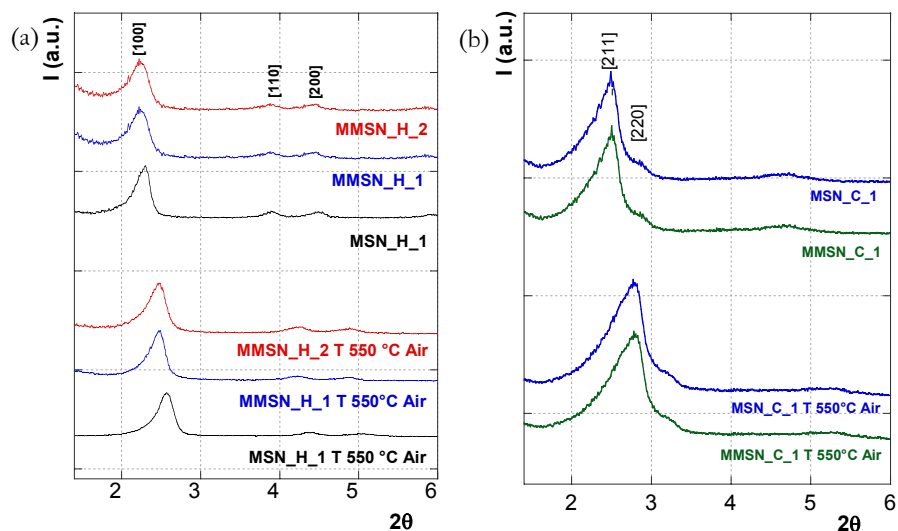


Figure 24. Low-angle XRD patterns of the (a) MMSN_H_1 and MMSN_H_2 and of the (b) MMSN_C_1 samples before and after calcination in air. For comparison pure silica samples MSN_H_1 and MSN_C_1 before and after thermal treatment in air have been reported.

In figure 25 are reported the nitrogen adsorption-desorption isotherms (figure 25(a)) and the pore size distribution (figure 25(b)) of samples MMSN_H_1, and MSN_H_1, after calcination in air.

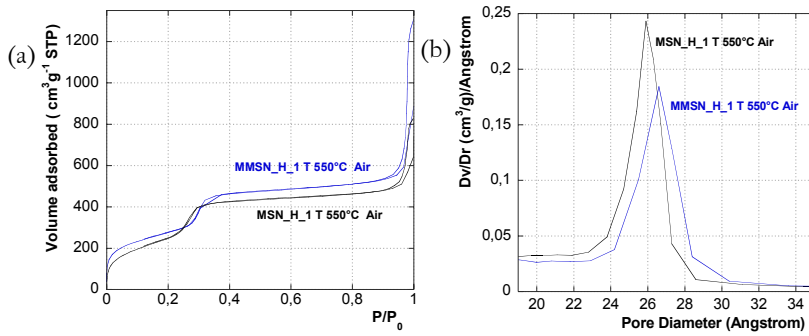


Figure 25. N₂-adsorption-desorption isotherms (a), and pore size distribution (b) of the MMSN_H_1, and MSN_H_1 samples calculated at 550°C.

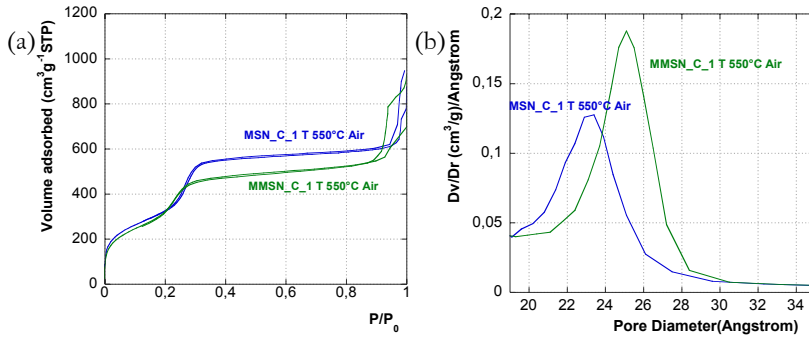


Figure 26. N₂-adsorption-desorption isotherms (a), and pore size distribution (b) of the MMSN_C_1, and MSN_C_1 samples calculated at 550°C.

The N₂ adsorption-desorption isotherms of the thermal treated MMSN_H_1 composite (figure 25(a)) exhibit, as for the pure silica (MSN_H_1), the characteristic IV behavior for a well-developed micro-mesoporous structure. A step in a relative pressure range of 0.20-0.4 is attributed to the nitrogen condensation that took place at the internal mesopores, and second step above 0.95 in the adsorption represents the formation of interstitial pores. All measured structural and textural characteristics are listed in table 5. The MMSN_H_1 sample treated at 550°C in air have high Brunauer-Emmett-Teller (BET) surface area (992 m²/g) and a large total pore volume (0.9 cm³/g). The Barret-Joyer-Halenda (BJH) method was applied to calculate the pore size distribution,

indicating a maximum pore diameter of 2.7 nm. The incorporation of the magnetic phase with a concentration of 5% in weight, once again, doesn't seem to change the features of the silica matrix, being the surface area of the pure hexagonal silica 1005 m²/g, the pore volume 1.1 cm³/g and the pore diameter 2.5 nm (table 5a). No significant effect has been revealed also on the thickness of the silica walls (1.5 nm against 1.4 nm).

Similar features have been shown by the N₂ adsorption-desorption isotherms of the sample MMSN_C_1 treated at 550°C with cubic pore structure (figure 26). The values of the surface area (S_{BET} ~ 1300 m²/g), of the total pore volume (V_p ~ 0.9 cm³/g) and of the pore diameter (D_{pore} ~ 2.5 nm), are similar to the pure silica MSN_C_1 and higher than the composites with hexagonal pores structure. Differently to the most common impregnation methods, where to a porous matrix is added the precursor of the desired phase, which imply a reduction of the surface area and of the pore volume, the proposed strategy, both for hexagonal and cubic systems, seems to preserve the textural properties of the matrix.

Table 5a. Textural and structural parameters of MMSN_H_1 and MSN_H_1 samples.

Sample	S _{BET} (m ² g ⁻¹)	V _p (cm ³ g ⁻¹)	(w _{BjH}) [†] (nm)	D ₁₀₀ (nm)	a ₀ [*] (nm)	D _{pore} (nm)
MMSN_H_1	-	-	-	4.0	4.6	-
MMSN_H_1 T 550°C Air	1005	1.1	1.5	3.6	4.1	2.7
MSN_H_1	-	-	-	3.8	4.4	-
MSN_H_1 T 550°C Air	992	0.9	1.4	3.4	4.0	2.5

*The lattice parameter (a₀) was calculated by the equation; $a_0 = \frac{2d_{100}}{\sqrt{3}}$ through X-ray diffraction data. †The wall thickness (w_{BjH}), was calculated from the difference between the lattice parameter (a₀) and the pore size (D_{pore}).

Table 5b. Textual structural parameters of MNS_C_1, and MMNS_C_1 samples.

Sample	S_{BET} ($\text{m}^2 \text{g}^{-1}$)	V_p ($\text{cm}^3 \text{g}^{-1}$)	$(w_{\text{BJH}})^\dagger$ (nm)	d_{211} (nm)	a_0^* (nm)	D_{pore} (nm)
MSN_C_1	-	-	-	3.5	8.7	-
MSN_C_1 T 550°C Air	1441	0.9	1.3	3.2	7.7	2.3
MMSN_C_1	-	-	-	3.5	8.5	-
MMSN_C_1 T 550°C Air	1306	0.9	1.3	3.2	7.7	2.5

*The lattice parameter (a_0) was calculated by the equation: $a_0 = \sqrt{6} \times d_{211}$ through X-ray diffraction data. †The wall thickness (w_{BJH}), was calculated by the equation: $\left(\frac{a_0}{3.092}\right) - \left(\frac{D_{\text{pore}}}{2}\right)$

As for the pure silica samples, FTIR has been performed in order to verified the silica formation and the surfactant removal induced by the thermal treatment. The FTIR spectrum of the sample MMSN_H.1 (figure 27) and MMSN_C_1, (figure 28) before calcinations, exhibits a series of adsorptions attributable to the presence of CTAB and F127: the symmetric (3010 cm^{-1}), CH_3 stretching modes, symmetric and asymmetric ($2920\text{-}2850 \text{ cm}^{-1}$) stretching, the bending (1450 cm^{-1}), and the rocking ($1400\text{-}720 \text{ cm}^{-1}$) modes of CH_2 group. Once the sample is subjected to calcination, the spectra show only a series of bands typical of vibrational modes of pure silica: the symmetric stretching modes of Si-O-Si group (1240 cm^{-1} , 1060 cm^{-1} , 800 cm^{-1}), of Si-OH group (960 cm^{-1}), and the bending mode (460 cm^{-1}) of O-Si-O group. The absence of bands associated to CTAB and F127 suggests that the surfactants have been completely removed. The small band at 590 cm^{-1} in all samples are ascribed to the Me-O stretching of the magnetite phase.

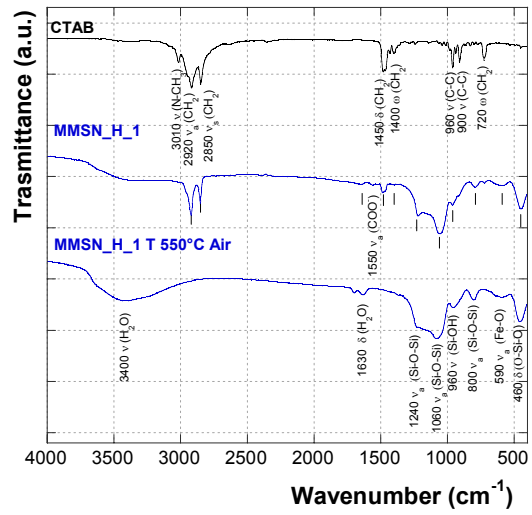


Figure 27. FTIR spectra of the CTAB and MMSN_H_1, before and after calcination.

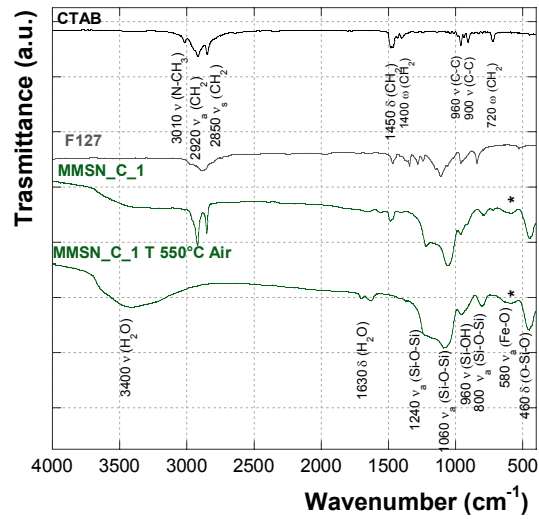


Figure 28. FTIR spectra of the CTAB, F127 and MMSN_C_1, before and after calcination.

All the magnetic mesoporous silica nanoparticles (MMSN) result to be stable over time in water for about 2 months, as shown in figure 29.

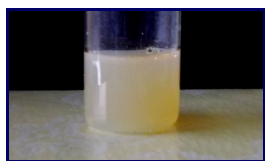


Figure 29. Stability in water of MMSN_H_1 sample.

To understand how the mesoporous silica and the concentration of the magnetic phase could affect magnetic properties of the magnetite nanoparticles, the MAG_6nm (magnetic core), MMSN_H_1 (magnetic phase 5% w/w), and MMSN_H_2 (magnetic phase 10% w/w) samples, have been submitted to preliminary magnetic measurements by SQUID. Temperature dependence of magnetization has been investigated by ZFC-FC protocols. Figure 30(a) show ZFC and FC magnetization curves of magnetic core MAG_6nm, and of the samples MMSN_H_1 and MMSN_H_2.

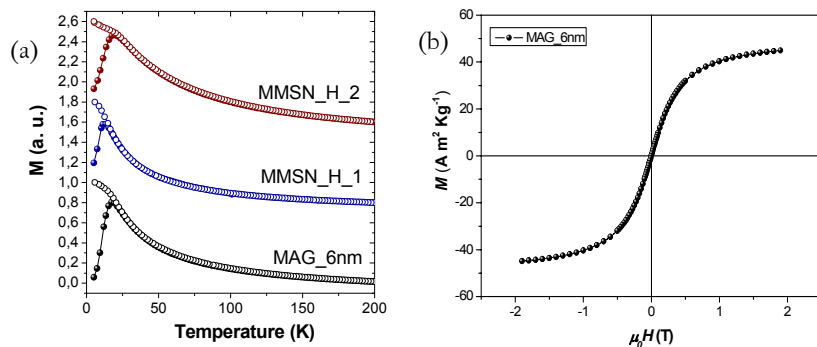


Figure 30. ZFC (full symbols) and FC(empty symbols) magnetizations for MAG_6nm (black), MMSN_H_1 (blue) and MMSN_H_2 (red) (a); Hysteresis loop at 300K of MAG_6nm normalized for the magnetic phase (black) (b).

The quantitative comparison between T_{\max} , T_{irr} , values (table 6) gives some indications regarding the differences between the samples. As expected, T_{irr} follow the same trend of T_{\max} (figure 30), indicating superparamagnetic behavior at room temperature for all samples. T_{irr} and T_{\max} (table 6) clearly decrease with the incorporation of the magnetic phase (MMSN_H_1 sample) in the mesoporous diamagnetic matrix: this behavior can be ascribed to a decrease of the interparticle interactions due to the quite homogeneous dispersion of the magnetite nanoparticles onto the silica. No change in terms of size or crystallinity of the magnetic phase can be in fact supposed, being the preformed MAG_6nm nanoparticles encapsulated at room temperature and without any further treatment. When the concentration of the magnetic phase is doubled, as observed by TEM analysis, the magnetic nanoparticles start to cluster and the average inter-particles distance decreases, and as a consequence the magnetic interaction become stronger. This effect is confirmed by the FC curve at low temperature. The difference between T_{\max} and T_{irr} , that provides a qualitative measure of the magnetic anisotropy distribution, and is strictly connected with the size distribution in the absence of interparticle interactions, are equal within the experimental error, further confirming that the magnetic phase doesn't undergo any modification when incorporated into the porous silica.

Table 6. Values of T_{\max} , T_{irr} for MAG_6nm, MMSN_H_1 and MMSN_H_2 samples.

Sample	$\langle D_{\text{TEM}} \rangle$ (nm)	σ (%)	T_{\max} (K)	T_{irr} (K)	T_{irr}, T_{\max} (K)	$*M_s$ (300 K) ($\text{A m}^2 \text{Kg}^{-1}$)
MAG_6nm	6	10	18	25	7	36 [†]
MMSN_H_1	75	16	13	20	7	0.6
MMSN_H_2	73	15	19	25	6	1.7

*The values of M_s have been normalized for the weight of the samples. †The value of M_s for the sample MAG_6nm become 48 at 300K when only the magnetic phase is considered, in agreement with the literature data

Field dependence of magnetization investigated a 300 K shows completely reversible behavior, confirming that all the samples are in superparamagnetic state. Saturation magnetization (M_s) is reported in table 6.

5.5 Conclusions

Mesoporous silica nanoparticles (MSN) possess unique structural features such as their large surface areas, tunable nanometer-scale pore sizes, and well-defined surface properties. Versatile mesoporous silica nanoparticles and magnetic silica-based nanocomposite were fabricated. Here, we highlight the synthetic approach that involves the encapsulation of hydrophobic magnetic nanoparticles within a mesoporous silica with hexagonal or cubic pore structure. In both strategies the nanoparticles were encapsulated in MSNs using CTAB as both phase transfer agents and pore-generating templates. The presence of the inorganic magnetic core seems to improve the features of the silica nanoparticles, leading to systems with smaller particle size and narrower particle size distribution if compared with the pure silica materials. Furthermore, the magnetic properties of the guest phase and the textural properties of the matrix were preserved. Using magnetic composites (MMSN) as a scaffold, other functional components such as fluorescent dyes or quantum dots can be integrated within these systems to generate multifunctional nanocomposite systems that maintain their individual functional characteristics. Clever combinations of different types of functional nanostructured materials will therefore be enable to the development of multifunctional nanomedical platforms for multimodal imaging or simultaneous diagnosis and therapy.

References

- [1] H. Guo¹, Haisheng Qian, S. Sun¹, D. Sun¹, H. Yin¹, X. Cai¹, Z. Liu¹, J. Wu¹, T. Jiang¹, X. Liu¹, *Hollow mesoporous silica nanoparticles for intracellular delivery of fluorescent dye*. Chemistry Central Journal **2011**.
- [2] K. Binnemans, *Lanthanide-Based Luminescent Hybrid Materials*. Chem. Rev. **2009**, 109, 4283-4374.
- [3] C. T. Kresge, M. E. Leonowicz, W. J. Roth, J. C. Vartuli, J. S. Beck, *Ordered mesoporous molecular sieves synthesized by a liquid-crystal template mechanism*. Nature **1992**, 359, 710-712.
- [4] J. S. Beck, J. C. Vartuli, W. J. Roth, M. E. Leonowicz, C. T. Kresge, K. D. Schmitt, C. T.-W. Chu, D. H. Olson, E. W. Sheppard, S. B. McCullen, J. B. Higgins, J. L. Schlenker, *A new family of mesoporous molecular sieves prepared with liquid crystal templates*. J Am. Chem. Soc. **1992**, 114, 10834-10843.
- [5] G. S. Attard, J. C. Glyde, C. G. Göltner, *Liquid-crystalline phases as templates for the synthesis of mesoporous silica*. Nature, **1995**, 378, 366-368.
- [6] A. Monnier, F. SchEth, Q. Huo, D. Kumar, D. Margolese, R. S. Maxwell, G. Stucky, M. Krishnamurty, P. Petroff, A. Firouzi, M. Janicke, B. Chmelka, *Cooperative Formation of Inorganic-Organic Interfaces in the Synthesis of Silicate Mesostructures*. Science **1993**, 261, 1299-1303.
- [7] G. S. Attard, J. C. Glyde, C. G. Göltner, *Liquid-crystalline phases as templates for the synthesis of mesoporous silica*. Nature **1995**, 378, 366-368.
- [8] F. Hoffmann, M. Cornelius, J. Morell, M. Fröba, *Silica-Based Mesoporous Organic-Inorganic Hybrid Materials*. Angew. Chem. Int. Ed. **2006**, 45, 3216-3251.
- [9] J. E. Lee, N. Lee, H. Kim, J. Kim, S. H. Choi, J. H. Kim, T. Kim, In C. Song, S. P. Park, W. K. Moon, T. Hyeon, *Uniform Mesoporous Dye-Doped Silica Nanoparticles Decorated with Multiple Magnetite Nanocrystals for Simultaneous Enhanced Magnetic Resonance Imaging, Fluorescence Imaging, and Drug Delivery*. J. Am. Chem. Soc. **2010**, 132, 552-55.

- [10] S.H. Wu, Y.S. Lin, Y. Hung, Y.H. Chou, Y.H. Hsu, C. Chang, C.Y. Mou, *Multifunctional Mesoporous Silica Nanoparticles for Intracellular Labeling and Animal Magnetic Resonance Imaging Studies*. Chem. Bio. Chem, **2008**, 9, 53-57.
- [11] Yu-Shen Lin, Christy L. Haynes, *Synthesis and Characterization of Biocompatible and Size-Tunable Multifunctional Porous Silica Nanoparticles*. Chem. Mater. **2009**, 21, 3979-3986.
- [12] T. W. Kim, P. W. Chung, Victor S.-Y. Lin, *Facile Synthesis of Monodisperse Spherical MCM-48 Mesoporous Silica Nanoparticles with Controlled Particle Size*. Chem. Mater. **2010**, 22, 5093-5104.
- [13] Yu-Shen Lin, C. L. Haynes, *Impacts of Mesoporous Silica Nanoparticles Size, Pore Ordering, and Pore integrity on Hemolytic Activity*. J. Am. Chem. Soc. **2010**, 132, 4834-4842.
- [14] K. K. Cotr, M. E. Belowich, M. Liong, M. W. Ambrogio, Y. A. Lau, H. A. Khatib, J. I. Zink, N. M. Khashab, J. Fraser Stoddart, *Mechanised nanoparticles for drug delivery*. Nanoscale, **2009**, 1, 16-39.
- [15] R. I. Nooney, D. Thirunavukkarasu, Y. M. Chen, R. Josephs, A. E. Ostafin, *Self-assembly of mesoporous nanoscale silica/gold composites*. Langmuir, **2003**, 19, 7628-7637.
- [16] U. Brohede, R. Atluri, A. E. Garcia-Bennett, M. Stromme, *Sustained release from mesoporous nanoparticles: Evaluation of structural properties associated with release rate*. Curr. Drug Delivery, **2008**, 5, 177-185.
- [17] K. Schumacher, P. I. Ravikovitch, A. Du Chesne, A. V. Neimark, K. K. Unger, *Characterization of MCM-48 Materials*. Langmuir, **2000**, 16, 4648-4654.
- [18] T. Suteewong, H. Sai, R. Cohen, S. Wang, M. Bradbury, B. Baird, S. M. Gruner, U. Wiesner, *Highly Aminated Mesoporous Silica Nanoparticles with Cubic Pore Structure*. J. Am. Chem. Soc. **2011**, 133(2), 172-175.
- [19] Y. Wan, D. Y. Zhao, *On the controllable soft-templating approach to mesoporous silicates*. Chem. Rev. **2007**, 107, 2821-2860.
- [20] M. Thommes, *Physical Adsorption Characterization of Nanoporous Materials*, Chemie Ingenieur Technik, **2010**, 82, No. 7, 1059-1073.

- [21] S. Ahmed, A. Ramli, *Effect of Surfactant Concentration on the Physico-chemical of Mesoporous Molecular Sieve*. Journal of Applied Sciences, **2011**, 11(7), 1178-1184.
- [22] M. Chakraborty, F. W. Hsiao, B. Naskar, C. H. Chang and A. K. Panda, *Surfactant-Assisted Synthesis and Characterization of Stable Silver Bromide Nanoparticles in Aqueous Media*, Langmuir, **2012**, 28, 7282-7290.
- [23] X. Huang, L. Zhou, C. Yu and D. Zhao, *Self-assembly of monodispersed silica nano-spheres with a closed-pore mesostructure*, J. Mater. Chem., **2012**, 22, 11523-11528.
- [24] C. Cannas, A. Musinu, A. Ardu, F. Orrù, D. Peddis, M. Casu, R. Sanna, F. Angius, G. Diaz, G. Piccaluga, *CoFe₂O₄ and CoFe₂O₄/SiO₂ Core/Shell Nanoparticles: Magnetic and Spectroscopic Study*. Chem. Mater., **2010**, 22, 3353-3361.
- [25] H. Y. Fan, E. W. Leve, C. Scullin, J. Gabaldon, D. Tallant, S. Bunge, T. Boyle, M. C. Wilson, C. J. Brinker, *Surfactant-assisted synthesis of water-soluble and biocompatible semiconductor quantum dot micelles*. Nano Lett., **2005**, 5, 645-648.
- [26] H. Yang, H. Zhou, C. Zhang, X. Li, H. Hu, H. Wu, S. Yang, *Water-soluble magnetic CoO nanocrystals functionalized with surfactants as T₂-weighed MRI contrast agents in vitro*. Dalton Trans., **2011**, 40, 3616-3621.
- [27] J. Kim, J.E. Lee, J. Lee, J.H. Yu, B.C. Kim, K. An, Y. Hwang, C.H. Shin, J.G. Park, J. Kim, T. Hyeon, *Magnetic fluorescent delivery vehicle using uniform mesoporous silica spheres embedded with monodisperse magnetic and semiconductor nanocrystals*. J. Am. Chem. Soc., **2006**, 128, 688-689.
- [28] X. Hu, P. Zrazhevskiy, X. Gao, *Encapsulation of Single Quantum Dots with Mesoporous Silica*. Annals of Biomedical Engineering, **2009**, 37, 1960-1966.

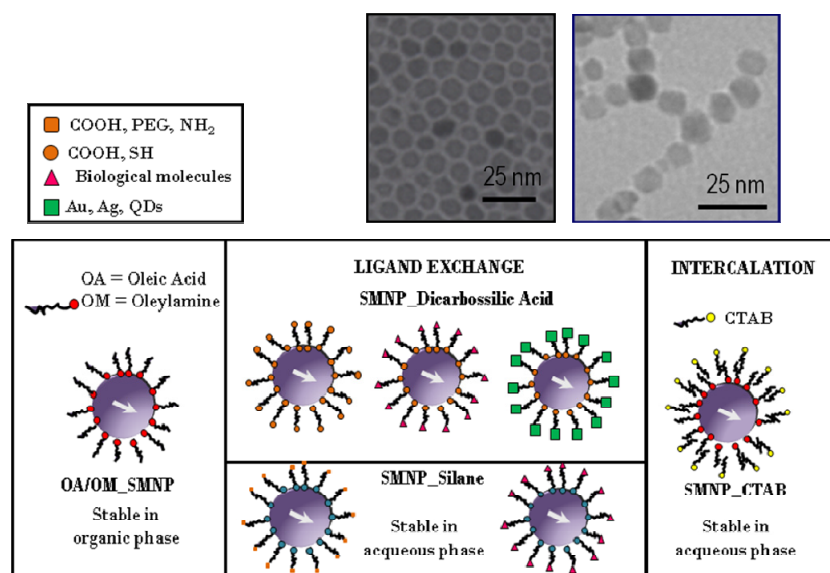
Conclusions and future insights

Uniform-sized colloidal nanocrystals have attracted much attention because of their unique magnetic and optical properties, as compared with those of their bulk counterparts. Especially, magnetic nanocrystals have been intensively pursued for biomedical applications, such as contrast enhancement agents in magnetic resonance imaging, magnetic carriers for drug delivery systems, biological labeling, and hyperthermia.

In the present thesis, because magnetic properties are size and chemical composition dependent, the first objective that has been attained was the achievement of magnetite and cobalt ferrite nanoparticles as unique phases with tunable size and narrow particle size distribution. High temperature thermal decomposition of metallorganic compounds in highly boiling solvents assisted by surfactant has been selected as synthetic strategy, as it has been widely shown that the non-aqueous routes are more efficient in producing stable colloidal nanoparticles with narrow particle size distribution, high crystallinity and tunable size and shape. Changing the solvent, the temperature, the time and the concentration of the surfactants it has been possible to change the size of the magnetic phases from about 4 to 12 nm.

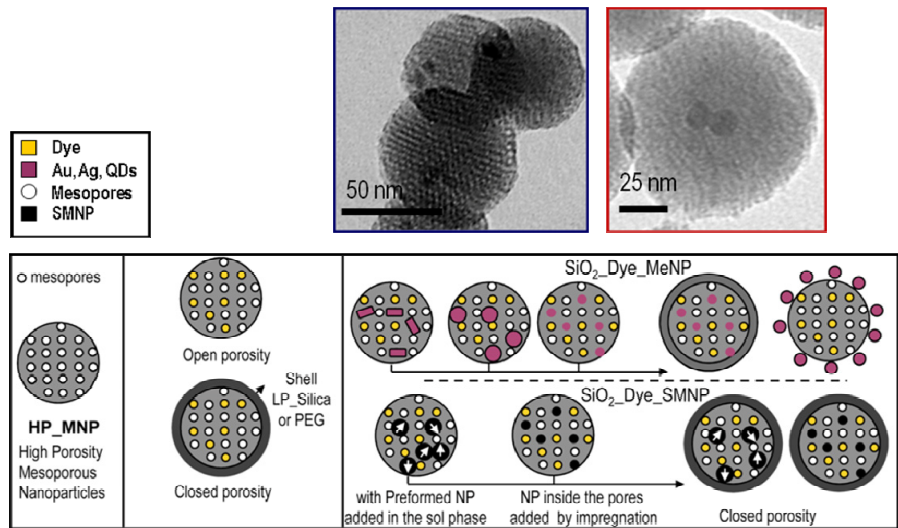
However, this approach produce hydrophobic nanoparticles, being the nanoparticle surface capped with oleic-acid and oleylamine, limiting their applications in biological and medical fields. Thus, the second important objective of this work was the transferring of these nanoparticles into water. The engineering of the surface has been carried out through two main strategies based on ligand exchange and intercalation processes. Small double functionalized molecules, as dimercapto-succinic acid and succinic acid, and silanes with COOH or PEG as functional groups, have been used as ligands to substitute the starting capping agents (oleic acid-oleylamine). The

characterization of the systems indicates that, in all the cases, the ligand exchange is almost complete, even if the presence of small amount of oleic acid cannot be excluded. Anyway all the ferrofluid are water dispersible and are stable for months. Intercalation phenomena can be induced by the using of molecules like cetyltrimetilmonium bromide (CTAB) and the corresponding water dispersions are very stable. All these aqueous ferrofluids can be used in MRI, in hyperthermia application and also for protein purification by magnetic separation.



The conversion of the hydrophobic nanoparticles into hydrophilic systems has been performed also by their encapsulation onto a silica mesoporous matrix. Due to their large pore size and high surface area, mesoporous materials and their composites with nanocrystals have attracted considerable attention. To use nanocrystals as functional delivery carriers and catalytic supports, nanocrystals coated with porous silica shells are desirable and to our knowledge there have been a few reports on their preparation. Silica is an ideal candidate, being biocompatible, having a low toxicity (size and surface area

dependent), high surface silanol groups and low density. In addition, mesoporous silica nanoparticles due to their high surface area and pore size can entrap magnetic nanoparticles and, at the same, time can be further functionalized with amino, mercapto, carboxy, cyano, phenyl, benzyl groups extending their range of possible applications. Thus, starting with the preparation of colloidal silica nanoparticles with ordered hexagonal or cubic structure and with ideal sizes for the applications in biomedicine, it has been possible to set up a synthetic strategy that has allowed to entrap the preformed hydrophobic nanoparticles within a mesostructured silica without changing the physical properties of the magnetic phase and the peculiar features of the matrix. The key molecule that has allowed the success of the synthetic strategy has resulted to be the ionic surfactant CTAB used both to intercalate oleic acid and as template for the formation of silica ordered porous structure. The “pseudo hybrid micelles” made up of an inorganic core and an organic shell of oleic acid-CTAB has been used instead of CTAB micelles to build the organic mesophase, that through a based catalyzed sol-gel process, has been coated with silica. Following this approach, magnetic mesoporous systems with hexagonal pore order has been achieved, and with the adding of the non-ionic surfactant F127 has been also possible to prepare magnetic composites with a cubic order. Size and particle size distributions are ideal for biomedical applications because of the low cytotoxicity that is size dependent.



The high potentiality of these systems derive from the possibility to make them multifunctional when to the magnetic nanoparticles are associated fluorescent or luminescent species as nanoparticles or molecules. Moreover, compared to non-porous silica nanoparticles, mesoporous silica materials can not only reduce red blood cell membrane damage but also provide a large surface area for drug loading. For these reasons I believe that these magnetic nanoparticles have great potential for bioimaging and drug delivery applications.

Several techniques have been used to obtain information on the system under investigation. In fact, only a multi-technique approach allow to elucidate their nanostructure and their properties.

Transmission Electron Microscopy (TEM)

Transmission Electron Microscopy (TEM) micrographs were obtained using a JEOL 200CX microscope operating at 200 kV. Colloidal dispersions have been dropped on conventional copper grids for the observations. Under the experimental conditions adopted, the wavelength of the incident beam is about 2.51×10^{-2} nm and the camera length is 82 cm. Particle size distributions have been obtained by bright field images, on different images the average diameter of about 200 particles in different parts of the grid. The standard deviation σ , was calculated from the following equation:

$$\sigma = \left\{ \sum \frac{[n_i (D_i - \langle D \rangle)^2]}{N} \right\}^{1/2}$$

High Resolution Transmission Electron Microscopy (HRTEM)

High Resolution (HR) TEM images were performed using a JEM 2010UHR (Jeol) microscope with a LaB₆ thermionic source operating at 200 kV and equipped with a Gatan Imaging Filter (GIF). Energy-filtered images were acquired using a 3 mm GIF entrance aperture and a slit width of 15 eV. All high-resolution images were acquired

digitally at microscope magnification of 25 kX, using 1 s or 2 s exposure and 1 x binning (1024 x 1024 pixel) of the charge coupled device (CCD) camera (a 794 slow scan). Because of the $\approx 19x$ magnification between the TEM viewing screen and the CCD camera, a preliminary calibration using a standard gold sample were performed to obtain corrected values of d-spacing in the samples.

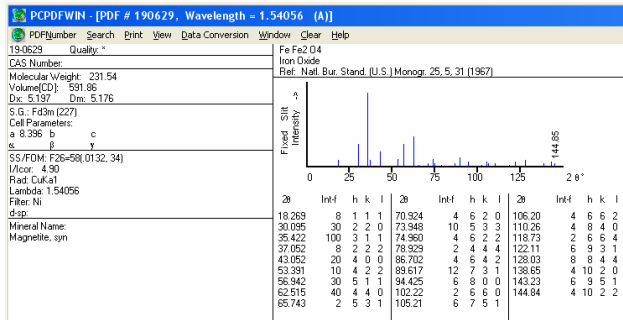
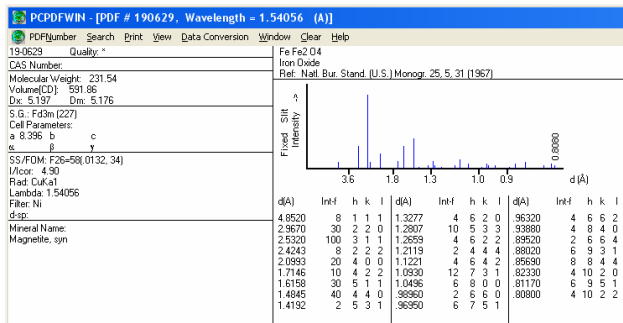
X-Ray Diffraction

Powder X-Ray Diffraction (XRD) spectra of the samples were collected using a Seifert diffractometer with a conventional θ - θ Bragg-Brentano focalising geometry, Cu-K α wavelength. An estimate of mean particle size ($\langle D_{XRD} \rangle$) was obtained from XRD patterns. The relation between average crystal size without disorder effects and full width at half maximum (fwhm) is expressed by Scherrer's equation:

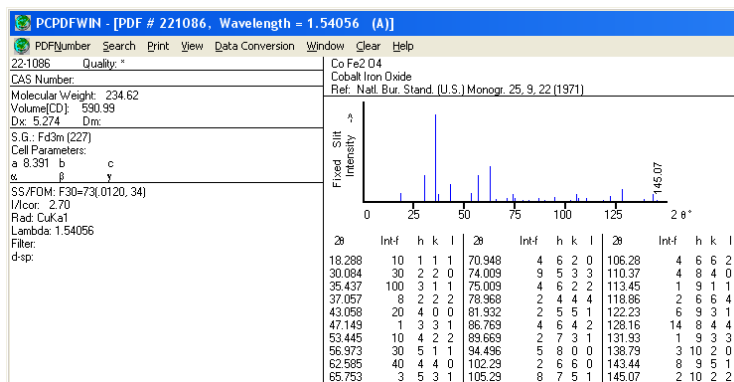
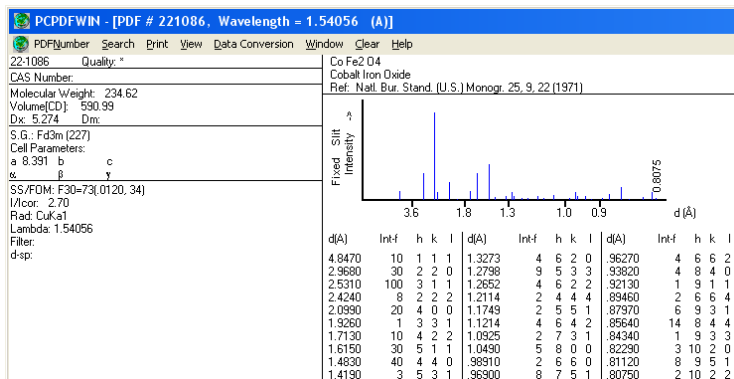
$$\langle D_{XRD} \rangle = \frac{K\lambda}{B \cos \theta}$$

where λ is the wavelength of X-Ray, θ is the angle of incident of X-ray beam, K is a constant related to the crystallite shape (0.9) and β is the pure breath of the powder reflection free of the broadening due to instrumental contributions. This calibration was performed by means of the spectrum of a standard Si sample and using the Warren correction $\beta_{sample} = (\beta_{exp}^2 - \beta_{std}^2)$.

PDF Card 19-0629 Fe₃O₄ -Magnetite



PDF Card 22-1086 -CoFe₂O₄



Infrared Spectroscopy

The absorption spectra were collected in the Mid region from 400 cm^{-1} to 2000 cm^{-1} using an Equinox 55 (Bruker) spectrophotometer. The samples were prepared in pellets obtained by dispersing the finely ground powder in KBr.

Nitrogen-physorption measurements

N_2 -physorption measurements at 77 K were carried out on a Sorptomatic 1990 System (Fisons Instruments). Before analysis, the samples were outgassed by heating at a rate of 1°C min^{-1} under vacuum at 200°C for 18 hours.

Thermogravimetry and Differential thermal Analysis

Thermogravimetry analysis (TGA) and simultaneous differential thermal analysis (SDTA) of the samples were carried out on a Mettler-Toledo TGA/SDTA 851. Thermal analysis data were collected in the range $25\text{-}1000^\circ\text{C}$ with an heating rate of $10^\circ\text{C min}^{-1}$ under oxygen flow (flow rate = 50 ml/min^{-1}).

Chemical Analysis (ICP-AES)

The determination of cobalt and iron concentrations in the samples was performed in triplicate by a Varian Liberty 200 Inductively Coupled Plasma Atomic Emission Spectrometer (ICP-AES). Before the analysis, 1 mL of sample was digested on a hot plate at 80°C for 6 h with 2 mL of aqua regia (HCl 37% grade and HNO_3 , 65% sub-boiled in 3:1 ratio) and 0.05 mL of H_2O_2 suprapure grade. After digestion, the samples were diluted to 100 mL with distilled water. Analysis was performed using multiple standard additions method.

Magnetic measurement

The magnetic measurements were carried out with a *Superconducting Quantum Interference Device* (S.Q.U.I.D.) The S.Q.U.I.D. magnetometer is, actually, the most sensitive magnetometer. It contains an superconducting magnet able to produce magnetic fields from zero to several positive and negative *Tesla*. In addition, it allows a precise control of the sample temperature from the liquid Helium temperature (4.2K) to 400K. The measurements of Magnetization versus temperature, performed with the ZFC and FC protocols, are one of the most classical approaches in order to observe superparamagnetic relaxation in nanoparticles. The ZFC protocol consists in cooling the sample from high temperature, where all the particles are in superparamagnetic state, to the lowest measuring temperature in zero magnetic field. Then a static magnetic field is applied and magnetization is measured during warming up (*MZFC*). The resulting curve is called *Zero Field Cooled* because the sample has been previously cooled in absence of a magnetic field. When the nanoparticles are cooled below the blocking temperature without magnetic field, all the net magnetic moments in each single domain particle point along the easy axis of the nanoparticles. The FC protocol consist in cooling the sample in a small DC field and measuring the magnetization during warming up without remove the field. When a magnetic field is applied during the cooling process (FC), all the net magnetic moments of the nanoparticles are aligned along the field direction. As the nanoparticles are cooled at low temperature, the magnetization direction of each particle is frozen in the field direction. By increasing the temperature, an increasing number of particles will be in superparamagnetic state and the magnetization monotonically will decrease giving rise to a typical “paramagnetic behaviour”. ZFC FC magnetization measurements were carried out by cooling the sample from 325K to 5K in zero magnetic field. Then a static magnetic field was applied. *MZFC* was measured during warming up from 4.2 to 325K, whereas *MFC* was recorded during the subsequent cooling. Stringently both *MZFC* and *MFC* should be measured in warming up.

Acknowledgements

First and foremost I would like to thank my research advisor, Dr. Carla Cannas, my mentorship provided me with the perfect balance of research independence and support. Her belief in me and at the end of my third year of graduate school provided incentive to achieve goals!

I especially would also like to acknowledge all of friends and all my lab-mates, that I have made prior to and during my years here who helped remind me that a full life requires a good balance between scientific discovery and friendship, travel and life experiences.

Andrea Ardu, Mauro Mureddu, Valentina Mamei, Roberta Sanna, Giorgia Manzo, Cristina Piras, Andrea Scorciapino, Manuela Pisu, Marzia Fantauzzi, Davide Peddis e Giuseppe Muscas. Thank you!

I'm very grateful to Prof. Anna Musinu and Prof. Giorgio Piccaluga for their guidance, support and mentoring.

I would like to thank Dr. Daniela Meloni for ICP analysis.

It was an honor to work with them, they were a significant contributor to my research.

Finally and certainly not least, I especially would like to thank my family for their support of all my life choices and their love, which is a constant source of strength for everything I do.